# Real Time Loudspeaker Control

Oliver Munroe

DOCTORAT BRETAGNE LOIRE SCIENCES POUR L'INGENIEUR

Le Mans Université

# THÈSE DE DOCTORAT DE

LE MANS UNIVERSITÉ

ÉCOLE DOCTORALE N° 602
*Sciences pour l'Ingénieur*
Spécialité : *« Acoustique »*

Par

## « Oliver MUNROE »

## « Real Time Loudspeaker Control »

**Thèse présentée et soutenue à « Le Mans », le « 17 November 2022 »**
**Unité de recherche : « LAUM »**
**Thèse N° : « 2022LEMA1022 »**

**Rapporteurs avant soutenance :**

| | |
|---|---|
| Wolfgang KLIPPEL | Professor, TUD DRESDEN, Allemagne |
| Finn AGERKVIST | Associate Professor, DTU LYNGBY, Danemark |

**Composition du Jury :**

| | | |
|---|---|---|
| Président : | Thomas HÉLIE | Directeur de Recherche CNRS, Laboratoire STM, UMR 9912 |
| Examinateurs : | Balbine MAILLOU | Maître de Conférence, Université de Lorraine |
| | Philippe HERZOG | Directeur de Recherche CNRS, ARTEAC-LAB |
| Dir. de thèse : | Laurent SIMON | Professeur, Le Mans University |
| Co-dir. de thèse : | Antonin NOVAK | Ingenieur de Recherche, Le Mans University |
| Co-dir. de thèse : | Daniel MASSICOTTE | Professeur, Université de Quebec à Trois Rivières, Canada |

# Real Time Loudspeaker Control

**Oliver Munroe**

## Abstract

The aim of this thesis is to provide simplified hardware and software solutions to the problem of real time loudspeaker linearisation. Most of the existing methods require the use of external sensors, use complex nonlinear models, or attempt to optimise all the nonlinear parameters of the feed forward model. From an industrial standpoint simplicity is attractive, so the main thematic of this work is to propose a linearisation framework that is as simple as possible while still being competitive with other methods.

In order to make the algorithm as simple as possible, most of the nonlinear parameters are provided *a priori* through the use of simulations and data sheets. Only the nonlinear function used to represent the loudspeaker suspension is optimised in real time to adapt the parameters to the sample drive unit. The algorithm is run on a low latency controller, and the control signal applied to the loudspeaker system via a transconductance power amplifier system. Both the controller and the power amplifier system were designed, built and validated by the author during this thesis.

The control system is simulated and the effects of Analog to Digital Converter (ADC) resolution, model error, and mechanical damping on the compensation are analysed. Measurement results show that the control system is capable of reducing both harmonic and intermodulation distortions in the cone acceleration by up to 25 dB between 10 Hz and 1000 Hz. The control system also enables the control of the linear frequency response of the loudspeaker system, removing the peaking present at the loudspeaker resonance frequency or providing a more broad band modification of the frequency response.

# Contrôle du haut parleur en temps réel

## Resumé

L'objectif de cette thèse est de fournir des solutions matérielles et logicielles simplifiées au problème de la linéarisation des haut-parleurs en temps réel. La plupart des méthodes existantes nécessitent l'utilisation de capteurs externes, utilisent des modèles non linéaires complexes, ou tentent d'optimiser tous les paramètres non linéaires du modèle prédictif. D'un point de vue industriel, la simplicité est attrayante, donc la thématique principale de ce travail est de proposer un cadre de linéarisation qui soit aussi simple que possible tout en étant compétitif avec les autres méthodes.

Afin de rendre l'algorithme aussi simple que possible, la plupart des paramètres non linéaires sont fournis a priori par l'utilisation de simulations et de fiches techniques. Seule la fonction non linéaire utilisée pour représenter la suspension du haut-parleur est optimisée en temps réel pour adapter les paramètres à l'échantillon. L'algorithme est exécuté sur un contrôleur à faible latence, et le signal de commande est appliqué au système de haut-parleurs via un système d'amplificateur de puissance à transconductance. Le contrôleur et le système d'amplificateur de puissance ont été conçus, construits et validés par l'auteur au cours de cette thèse.

Le système de contrôle est simulé et les effets de la résolution ADC, de l'erreur de modèle et de l'amortissement mécanique sur la compensation sont analysés. Les résultats des mesures montrent que le système de contrôle est capable de réduire les distorsions harmoniques et d'intermodulation dans l'accélération du cône jusqu'à 25 dB entre 10 Hz et 1000 Hz. Le système de contrôle permet également de contrôler la réponse en fréquence linéaire du système de haut-parleurs, en éliminant le pic présent à la fréquence de résonance du haut-parleur ou en fournissant une modification plus large de la réponse en fréquence.

# Acknowledgements

I would first like to thank Laurent Simon, Antonin Novak, and Daniel Massicotte for the opportunity to undertake this thesis project. The support and advice they provided proved to be an important asset in progressing and refining this work.

I extend my appreciation and thanks to Wolfgang Klippel and Finn Agerkvist who accepted to review the manuscript, Balbine Maillou and Philippe Herzog who agreed to act as examiners, and Thomas Hélie for presiding over the thesis defence.

I would also like to thank James Blondeau for providing all the necessary equipment while also keeping me supplied with enough drive units to replace the ones that I broke.

I am grateful to Hervé Mezzière, Jacky Maroudaye and Eric Egon for their time, ideas, and advice during the design and manufacturing of some of the hardware produced during this thesis.

I am extremely grateful to Stéphane Letourneur for the help, advice and discussions when designing, assembling and debugging the real time controller. Thanks to Pierre-Arnaud Lecompte for showing me how to use the SMD assembly equipment.

Finally, I am deeply grateful to my family, in particular my wife Adeline and daughter Ellie for their support, humour, and forcing me to stop my work to play pirates in the garden.

*Enjoy yourself, it is later than you think.*

*Time flies like an arrow, fruit flies like bananas.*

# Acronymes

ΣΔ Sigma Delta.

**µC** Micro Controller.

**AC** Alternative Current.

**ADC** Analog to Digital Converter.

**AISI** American Iron and Steel Institute.

**CAD** Computer Aided Design.

**DAC** Digital to Analog Converter.

**DAQ** Data Acquisition system.

**DC** Direct Current.

**DOF** Degree Of Freedom.

**DSP** Digital Signal Processor.

**DUT** Device Under Test.

**EMF** Electro-Motive Force.

**ENOB** Effective Number Of Bits.

**FEA** Finite Element Analysis.

**FFT** Fast Fourier Transform.

**FIR** Finite Impulse Response.

**FP** Floating Point.

**FPU** Floating Point Unit.

**HD** Harmonic Distortion.

**IDE** Integrated Development Environment.

**IMD** Intermodulation Distortion.

**LSI** Large Signal Identification.

**MFB** Motional Feed Back.

**MTND** Multi Tone Nonlinear Distortion.

**NLC** Nonlinear Control.

**ODE** Ordinary Differential Equation.

**Op Amp** Operational Amplifier.

**PC** Personal Computer.

**PCB** Printed Circuit Board.

**SAR** Successive Approximation Register.

**SINAD** Signal to Noise And Distortion ratio.

**SPI** Serial Peripheral Interface.

**UV** Ultra Violet.

# NOMENCLATURE

---

**Physics Constants**

| | | |
|---|---|---|
| $\mu_0$ | Magnetic Permeability of Free Space | $4\pi \times 10^{-7}$ |
| $\rho_{air}$ | Air density at ambient conditions | $1.18\,\mathrm{kg\,m^{-3}}$ |
| $c$ | Celerity of sound in air | $343\,\mathrm{m\,s^{-1}}$ |

**Physics Quantities**

| | | |
|---|---|---|
| $\epsilon$ | EMF | V |
| $\mu_r$ | Relative Permeability | – |
| $\phi$ | Magnetic Flux | Wb |
| $\Pi$ | Mutual Inductance | H |
| $\rho_w$ | Electrical Resistivity | $\Omega\,\mathrm{m^{-1}}$ |
| L | Inductance | H |
| R | Electrical Resistance | $\Omega$ |
| **B** | Magnetic Flux Density | T |
| **E** | Electrical Field | $\mathrm{V\,m^{-1}}$ |
| **F** | Force | N |
| **I** | Current | A |
| **J** | Current Density | $\mathrm{A\,m^{-2}}$ |
| $q$ | Electric Charge | C |
| $v$ | Velocity | $\mathrm{m\,s^{-1}}$ |

**Model Parameters.** **** Denotes a nonlinear dependence on coil position*** $x$

| | | |
|---|---|---|
| $\delta_w$ | Coil Wire Thermal Coefficient | – |
| $\mathrm{C}_{ms}$* | Spring Compliance. *Defined as the ratio between displacement and force.* | $\mathrm{m\,N^{-1}}$ |
| $\mathrm{G}_v$ | Feedback Gain | – |
| $\mathrm{K}_{ms}$* | Spring Stiffness. *Defined as the ratio between force and displacement.* | $\mathrm{N\,m^{-1}}$ |

| | | |
|---|---|---|
| $L_e*$ | Lossless Coil Inductance | H |
| $L_N*$ | Voice Coil Para-Inductance | H |
| $M_{ms}$ | Moving Mass | kg |
| $R_e$ | Coil DC Resistance | Ω |
| $R_N*$ | Eddy Current Losses | Ω |
| $R_{ms}$ | Viscous Damping | $\mathrm{N\,s\,m^{-1}}$ |
| T | Coil Temperature | K |
| $B\ell*$ | Force Factor | $\mathrm{N\,A^{-1}}$ |

**Model Quantities**

| | | |
|---|---|---|
| $a_T$ | Target Acceleration | $\mathrm{m\,s^{-2}}$ |
| F | Total Force | N |
| $F_T$ | Target Force | N |
| $F_{rel}$ | Reluctance Force | N |
| $i_T$ | Target Current | A |
| $u_{DUT}$ | DUT Terminal Voltage | V |
| $v_T$ | Target Velocity | $\mathrm{m\,s^{-1}}$ |
| $v_{DUT}$ | DUT Coil Velocity | $\mathrm{m\,s^{-1}}$ |
| $v_{err}$ | Velocity Error | $\mathrm{m\,s^{-1}}$ |
| $x_T$ | Target Displacement | m |

# TABLE DES MATIÈRES

# TABLE DES FIGURES

Chapitre 1

# Introduction and State of the Art

## 1.1 Loudspeaker Control

The moving coil loudspeaker has not changed much since its conception over 100 years ago. What has changed is the requirements of the loudspeaker and the system it is installed in. Systems need to be smaller, more linear and produce more low frequency energy. Producing low frequency sounds with a smaller volume can be done by simply increasing the amplifier power and applying a bass boost, such as in the Linkwitz transform or the ACE Bass system [89]. Unfortunately the increase in current and cone displacement invariably increases the amount of distortion produced by the speaker. Up til recently, the chosen way of reducing system distortion was to invest time and money into researching different materials, structure geometries and understanding the sources of distortion. Although this path has provided innovative solutions and vast amounts of insight into the distortion mechanisms of the electrodynamic loudspeaker, there has been a growing amount of interest in another way of reducing system distortion, active linearisation of nonlinear systems. The premise is rather simple, use feedback or feed forward techniques to reduce the distortion produced by the system. However, in reality, the actual application of these methods quickly becomes expensive, complicated to apply to a production run of thousands of units or difficult to integrate.
This thesis aims to provide three things :

- a framework for applying an active linearisation technique to any loudspeaker system,
- the required hardware to efficiently apply the correction routines,
- a foundation for future works.

## 1.2 Thesis Organisation

The first section that gives a brief introduction on the necessity of loudspeaker control is followed by a first principles explanation of the electrodynamic loudspeaker and a selection of the nonlinear phenomena. These nonlinear phenomena are then sorted into three groups of complexity. A comparison of the various compensation methods is then presented, and various bibliographical references are analysed, with a cherry picking of interesting ideas. The models section compares a selection of electromagnetic and mechanical models for use in the compensation algorithm with a discussion around the numerical methods required to run the compensation methods. Finally, the conclusion summarises the analysis and provides the axes of research for this thesis.
The second section lays out the various methods that are required to apply the compensation method. This is split into two parts, software and hardware. The software part focuses on the models required for the compensation algorithm and the fitting of the parameters, while the main axes of hardware research are :

- a mechanical jig to allow the measurement of the voice coil electrical impedance and force for various coil positions inside the motor and for frequencies between 0 Hz and 1 kHz,
- a controller to acquire the various signals, run the compensation algorithm and output compensation signal voltage.

The third and final section shows the results of the compensation method and discuss the advantages and disadvantages of the chosen approach before laying out possible future paths of research and concluding.

## 1.3 Basic Loudspeaker

There are many different ways of producing sound, although the most common is with the use of an electrodynamic loudspeaker. It is a type of voice coil actuator, and its fundamental structure has not changed since its invention by Chester W Rice in 1925 [83]. An example of the basic structure can be seen in Figure 1.1. The motor is comprised of a permanent magnet and some low carbon steel. The magnetic field from the magnet is guided by the steel and is focused in the magnetic gap in which sits the voice coil. A current flowing in the voice coil interacts with the magnetic field in the gap, and moves the voice coil in a specific direction due to the Lorentz force. The motion of the voice coil is transferred to cone which displaces the air resulting in sound. Two suspension elements, the spider and surround serve differing purposes. The spider provides the main restoring spring force, stopping the cone flying away from the structure, while the surround provides an air seal, damping to the cones outer edge, and radial stability to the cone.

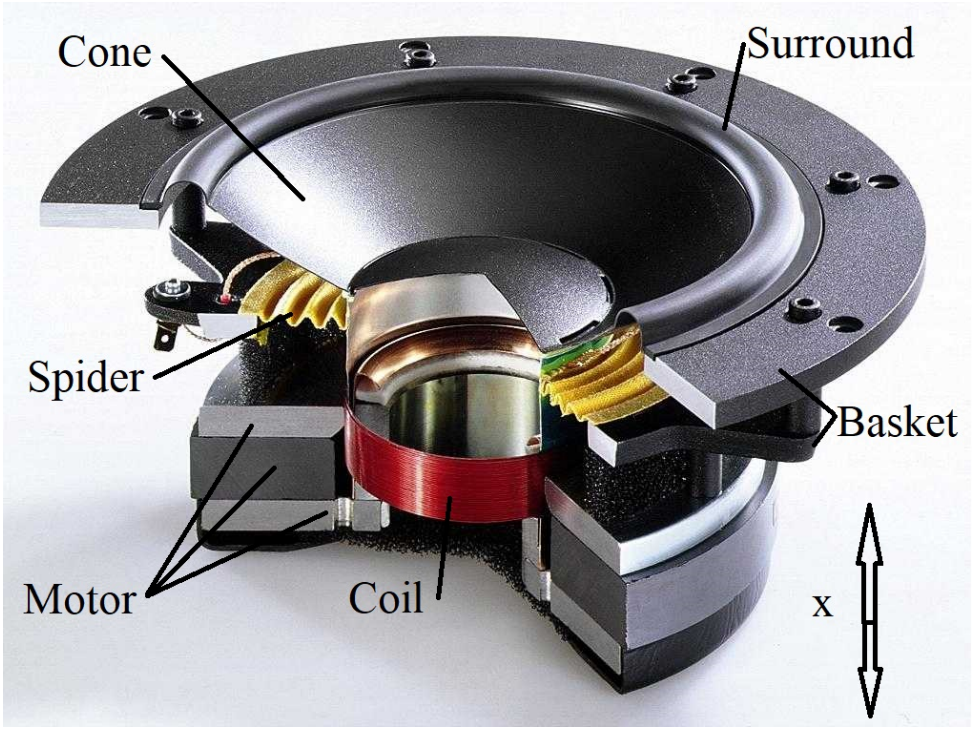


FIGURE 1.1 – Electrodynamic Loudspeaker.

## 1.4 First principles

This section serves as a demonstration of the fundamental principles that govern the behaviour of a loudspeaker motor. A first principles approach is taken to illustrate to source of several nonlinear phenomena.

### 1.4.1 Electromagnetics

In the case of the loudspeaker motor system, Maxwell's equations are used to derive the more well known parameters and expression of the electrodynamic loudspeaker drive unit. Most of these results are also found in classic electromagnetic literature [26, 33]

#### Lorentz Force

The mechanism responsible for the conversion of electrical energy into mechanical energy is the Lorentz force (sometimes called the Laplace force). The original Lorentz force expression (Equation 1.1) states that a particle of charge $q$, moving through a magnetic field $\overrightarrow{\mathbf{B}}$ and electrical field $\overrightarrow{\mathbf{E}}$ at a velocity $\overrightarrow{v}$ will experience a force $\overrightarrow{\mathbf{F}}$ such that

$$\overrightarrow{\mathbf{F}} = q\overrightarrow{\mathbf{E}} + q\overrightarrow{v} \times \overrightarrow{\mathbf{B}}. \tag{1.1}$$

An electrical current is simply a stream of charges. Thus if we imagine a current $\overrightarrow{\mathbf{I}}$ flowing through a length of wire $dl$ as a linear density $\rho_c$ of charges travelling at a velocity $\overrightarrow{v}$, the force exerted on this piece of wire is

$$\overrightarrow{\mathbf{dF}} = (\rho_c dl)\overrightarrow{\mathbf{E}} + (\rho_c dl)\overrightarrow{v} \times \overrightarrow{\mathbf{B}}. \tag{1.2}$$

If we assume that the electrical field is zero, and that the electrical current defines the vector, then

$$\overrightarrow{\mathbf{dF}} = \overrightarrow{\mathbf{I}}\, dl \times \overrightarrow{\mathbf{B}}. \tag{1.3}$$

Finally by integration we arrive at the expression for the force acting on a current carrying wire in a uniform magnetic field

$$\overrightarrow{\mathbf{F}} = \overrightarrow{\mathbf{I}}\, l \times \overrightarrow{\mathbf{B}}. \tag{1.4}$$

The vector cross product $\times$ may be rewritten as

$$\overrightarrow{A} \times \overrightarrow{B} = |A||B| \sin\Theta_{AB}\, \overrightarrow{n}, \tag{1.5}$$

where $\overrightarrow{A}$ and $\overrightarrow{B}$ are two vectors in the same plane separated by an angle $\Theta_{AB}$ and $\overrightarrow{n}$ is the unit vector perpendicular to both $\overrightarrow{A}$ and $\overrightarrow{B}$, the $||$ operator signifies their magnitudes. Thus Equation (1.5) can be rewritten as

$$\overrightarrow{\mathbf{F}} = |\mathbf{I}||\mathbf{B}| l \sin\Theta_{IB} \overrightarrow{n}. \tag{1.6}$$

The Lorentz force is thus perpendicular to both the current **I** and the magnetic field **B**, and maximal when **I** and **B** are perpendicular. This can be observed using the right hand rule as shown in Figure 1.2.

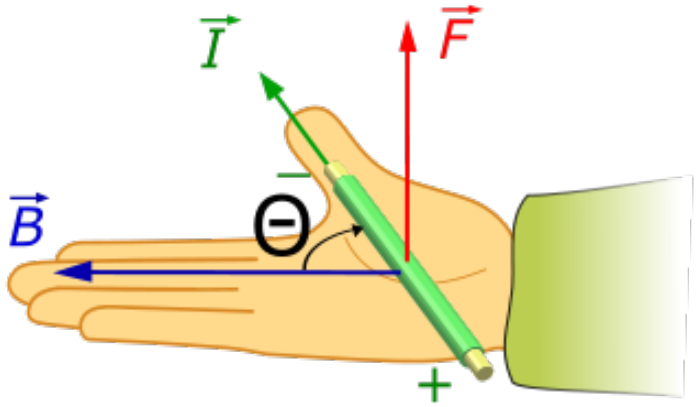


FIGURE 1.2 – Right Hand rule from [40].

From Equation (1.6), it is clear that in order to maximise the amount of force, we need to maximise the three quantities **B**, **I** and $l$ while also ensuring that **B** is perpendicular to **I**.
In the case of a voice coil in the loudspeaker motor, where the total length of wire $\ell$ in the field $\overrightarrow{\mathbf{B}}$ is $N$ turns of a coil of length $l$

$$|\overrightarrow{\mathbf{F}}| = |\overrightarrow{\mathbf{B}}|\ell|\overrightarrow{\mathbf{I}}|. \tag{1.7}$$

In the case of a loudspeaker drive unit, the amount of turns intersected by **B** depends on the position of the coil as shown in Figure 1.3, leading to force (nonlinearly) depending on coil position. The efficiency of the conversion of electrical current to mechanical force will therefore not be uniform when the coil moves. The conversion factor $|\overrightarrow{\mathbf{B}}|\ell$, often termed 'force factor' $B\ell$ in loudspeakers will depend on the coil position $x$, giving $B\ell(x)$. Figure 1.3 was generated using data from a FEA [65] simulation. An increase in $\ell$ results in an increase in the wires electrical resistance and inductance, which we shall look at next.

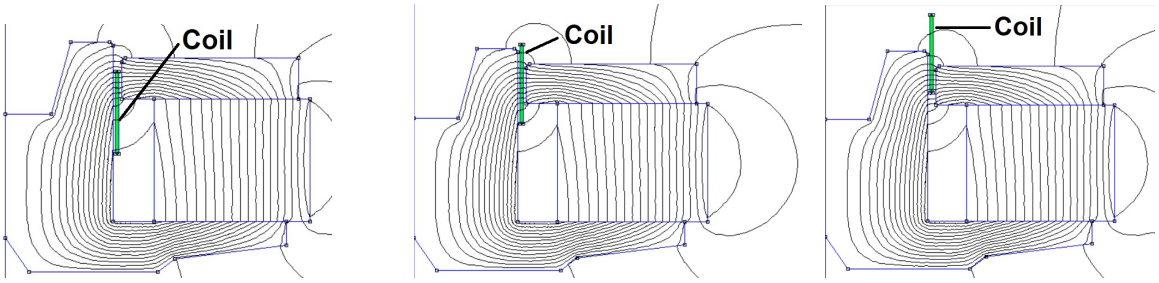


(a) Coil at −5 mm. (b) Coil at 0 mm. (c) Coil at +5 mm.

FIGURE 1.3 – Magnetic flux lines intersecting the coil at different positions. (a) : Magnetic flux lines intersecting the coil which is positioned 5 mm into the motor. (b) : Magnetic flux lines intersecting the coil which is at the rest position (0 mm). (c) : Magnetic flux lines intersecting the coil which is positioned 5 mm out of the motor. Images generated using FEA software [65].

### Electrical Resistance

The electrical resistance $R$ of a wire of length $\ell$, cross section area $S_w$ and electrical resistivity $\rho_w$ can be calculated with

$$R = \rho_w \frac{\ell}{S_w}. \tag{1.8}$$

This formula however does assume that the current density is uniform inside the wire. Due to its finite resistance, the wire is subjected to Joule heating, where the dissipated power $P_w$ can be calculated through

$$P_w = Ri^2. \tag{1.9}$$

Finally, any dissipated power results in a heating of the wire and surrounding material. When the temperature of a metal increases, so does its electrical resistance. This can be approximated through the first order equation [100],

$$R(T_w) = R_0(1 + \delta_w(T_w - T_0)), \tag{1.10}$$

where $R(T_w)$ is the resistance of the wire at a temperature $T_w$, $R_0$ is the resistance of the wire at a reference temperature $T_0$ and $\delta_w$ is the temperature coefficient of the wire material.

### Electro-Motive Force (EMF)

A voice coil is most commonly constructed as a multilayer coil with an even number of layers. The winding of the coil means the geometry is helical in nature, as shown in Figure 1.4. In [66] it was shown that for a single layer coil, the geometry is helical and thus the surface integral operations become incredibly complex. However, in the case of a coil with an even number of layers, there are an even number of helical surfaces whose normal directions are opposed due to the winding direction. In the case of a two-layer coil, the normals of the two surfaces will be opposed and approximately equal, thus they can be neglected and we can thus perform a much simpler integral over $N$ surfaces where each surface corresponds to a single turn. The voice coil can be thus defined as $N$ loops of wire.

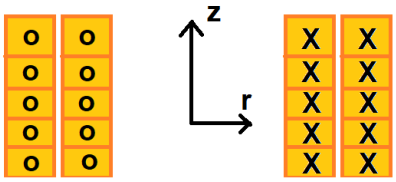


(a) Two layer voice coil winding. The circles and crosses show the direction of the current flow, circles indicates out of the page and crosses indicating into the page.

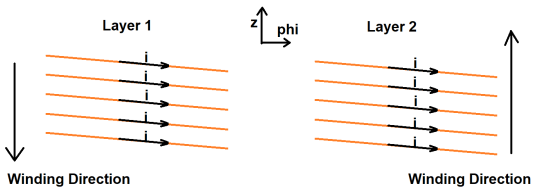


(b) Layer winding direction. Due to the winding direction, the surfaces defining layers 1 and 2 have opposed normals (z direction).

FIGURE 1.4 – (a) : Current flow inside a two layer voice coil. Circles show current flowing out of the page, while crosses show current flowing into the page. (b) : Current flow and winding direction for each layer of the two layer coil.

Some portion of the coil also sits inside a magnetic field $\overrightarrow{\mathbf{B_m}}$. We define the magnetic flux $\phi_m(t)$ of the voice coil as

$$\phi_m(t) = \int_{\Sigma(t)} \overrightarrow{\mathbf{B_{tot}}}(t) \cdot \overrightarrow{\mathbf{dA}}, \tag{1.11}$$

where $\Sigma(t)$ is the surface encircled by the coil, $\overrightarrow{\mathbf{dA}}$ is an element of this surface, $\overrightarrow{\mathbf{B_{tot}}}(t)$ is the total magnetic field

$$\overrightarrow{\mathbf{B_{tot}}}(t) = \overrightarrow{\mathbf{B_c}}(t) + \overrightarrow{\mathbf{B_m}}(t), \tag{1.12}$$

with $\overrightarrow{\mathbf{B_c}}(t)$ the field generated by the coil, and $\overrightarrow{\mathbf{B_m}}(t)$ the field generated by the magnet. Both of these quantities are supposed to vary over time for this analysis. From Faraday's law, we know that for a coil of $N$ loops, the EMF $\epsilon(t)$ generated inside the coil is

$$\epsilon(t) = -N\frac{d\phi_m(t)}{dt}. \tag{1.13}$$

Thus

$$\epsilon(t) = -N\frac{d}{dt}\int_{\Sigma(t)} \overrightarrow{\mathbf{B_{tot}}}(t) \cdot \overrightarrow{\mathbf{dA}}. \tag{1.14}$$

In the case of the voice coil, the magnetic field can change either because of a change in current $i$ or a change in coil position $x$. We therefore split the integral into two parts, one represents the integrand changing, the other represents the integration area changing as

$$\epsilon(t=t_0) = -N\left[\int_{\Sigma(t_0)} \frac{d\overrightarrow{\mathbf{B_{tot}}}(t)}{dt}\Big|_{t_0} \cdot \overrightarrow{\mathbf{dA}} + \frac{d}{dt}\int_{\Sigma(t)} \overrightarrow{\mathbf{B_{tot}}}(t_0) \cdot \overrightarrow{\mathbf{dA}}\right], \tag{1.15}$$

where $t_0$ is any fixed point in time. If we split this expression into its two components, $\epsilon_T$ which represents the contribution from a time varying magnetic field, and $\epsilon_M$ which represents the contribution from the motion of the coil

$$\begin{aligned} \epsilon_T(t_0) &= -N\int_{\Sigma(t_0)} \frac{d\overrightarrow{\mathbf{B_{tot}}}(t)}{dt}\Big|_{t_0} \cdot \overrightarrow{\mathbf{dA}} \\ \epsilon_M(t_0) &= -N\frac{d}{dt}\int_{\Sigma(t)} \overrightarrow{\mathbf{B_{tot}}}(t_0) \cdot \overrightarrow{\mathbf{dA}}, \end{aligned} \tag{1.16}$$

the first term can be rewritten using the integral form of the Maxwell-Faraday equation

$$\epsilon_T(t_0) = N\oint_{\partial\Sigma(t_0)} \overrightarrow{\mathbf{E}}(t_0) \cdot \overrightarrow{dl}, \tag{1.17}$$

where $\partial\Sigma(t_0)$ represents the closed path formed by the coil. For the second term, we assume that the coil moves axially due to a velocity $\overrightarrow{v_{coil}}$. Over a small amount of time $dt$ the velocity will change the area of integration $\overrightarrow{\mathbf{dA}}$ by the area $\overrightarrow{\mathbf{dA}_\delta}$

$$\overrightarrow{\mathbf{dA}_\delta} = \overrightarrow{v_{coil}}dt \times \overrightarrow{dl}, \tag{1.18}$$

where $\overrightarrow{dl}$ is a small length of one turn. Thus $\epsilon_M$ can be written

$$\epsilon_M(t_0) = -N\frac{d}{dt}\int_{\Sigma(t)} \overrightarrow{\mathbf{B_{tot}}}(t_0) \cdot (\overrightarrow{v_{coil}}(t_0)dt \times \overrightarrow{dl}), \tag{1.19}$$

which can then be transformed into

$$\epsilon_M(t_0) = N\oint_{\delta\Sigma(t_0)} (\overrightarrow{v_{coil}}(t_0) \times \overrightarrow{\mathbf{B_{tot}}}(t_0)) \cdot \overrightarrow{dl}. \tag{1.20}$$

By reassembling both expressions, we can find the total emf due to changes in the magnetic field

$$\epsilon(t_0) = N\left[\oint_{\partial\Sigma(t_0)} (\overrightarrow{\mathbf{E}}(t_0) + \overrightarrow{v_{coil}}(t_0) \times \overrightarrow{\mathbf{B_{tot}}}(t_0)) \cdot \overrightarrow{dl}\right]. \tag{1.21}$$

We can therefore see that the total emf or voltage generated by the coil in the motor is the sum of two emfs, $\epsilon_T$ which is due to a time varying magnetic field whose contribution is often modelled via an inductive component, and $\epsilon_M$ which is due to the velocity of the coil inside the magnetic field whose contribution is often modelled via the coupling

between the mechanical and electrical domains

$$\begin{aligned}\epsilon_T(t) &= N \oint_{\partial\Sigma(t)} \overrightarrow{\mathbf{E}}(t) \cdot \overrightarrow{dl}, \\ \epsilon_M(t) &= N \oint_{\partial\Sigma(t)} (\overrightarrow{v}_{coil}(t) \times \overrightarrow{\mathbf{B_{tot}}}(t)) \cdot \overrightarrow{dl}.\end{aligned} \tag{1.22}$$

The velocity of the coil $\overrightarrow{v}_{coil}$ is parallel with the direction of the magnetic field created by the coil, $\overrightarrow{\mathbf{B_c}}$, and perpendicular to both $\overrightarrow{dl}$ and the magnetic field created by the magnet $\overrightarrow{\mathbf{B_m}}$. Thus $\epsilon_M$ can be written

$$\epsilon_M = B_m \ell v_{coil}, \tag{1.23}$$

where $\ell$ is the total length of the $N$ wire loops that make up the coil $\ell = Nl$. When in motion, the length of coil $\ell$ wire situated in the magnetic field will vary. Therefore, both $\epsilon_T(t)$ and $\epsilon_M(t)$ will have a dependency on the coil position.
In guise of a simple example of how the emf $\epsilon_T$ due to a time varying magnetic field can be modelled through an inductive component, we will assume that there is no exterior magnetic field, such that only the time varying magnetic field from the coil current exists. The emf generated will be

$$\epsilon(t_0) = \epsilon_T(t_0) = -N \int_{\Sigma(t_0)} \frac{d\overrightarrow{\mathbf{B_c}}(t)}{dt}\bigg|_{t_0} \cdot \overrightarrow{\mathbf{dA}}. \tag{1.24}$$

In the case of a long thin coil in air of length $\ell$ constituted of $N$ loops of length $l$, then the magnetising field $\overrightarrow{\mathbf{B_c}}$ can be approximated through Ampère's circuit law

$$\oint \overrightarrow{\mathbf{B_c}} \cdot \overrightarrow{dl} = \mu_0 \mu_r \iint_S \overrightarrow{\mathbf{J}} \cdot \overrightarrow{dS}, \tag{1.25}$$

where $\mu_0$ is the permeability of free space ($4\pi.10^{-7}$ H/m), $\mu_r$ is the relative permeability of the medium, $\overrightarrow{\mathbf{J}}$ is the current density inside the coil and $S$ is the surface enclosed by the coil. This may be simplified to

$$\overrightarrow{\mathbf{B_c}}\ell = \mu_0 \mu_r N \overrightarrow{\mathbf{I}}, \tag{1.26}$$

or finally

$$\overrightarrow{\mathbf{B_c}} = \frac{\mu_0 \mu_r N}{\ell} \overrightarrow{\mathbf{I}}. \tag{1.27}$$

This leads to the expression for the emf generated by a long thin coil

$$\epsilon(t_0) = -\frac{\mu_0 \mu_r N^2}{\ell} \int_{\Sigma(t_0)} \frac{d\,\overrightarrow{\mathbf{I}}(t)}{dt}\bigg|_{t_0} \cdot \overrightarrow{\mathbf{dA}}, \tag{1.28}$$

which simplifies to

$$\epsilon(t) = -\frac{\mu_0 \mu_r N^2}{\ell} \frac{di}{dt} A, \tag{1.29}$$

where $A$ is the cross section area of the coil. This leads to the expression of the inductance of an air cored coil

$$\begin{cases} \epsilon(t) = -L\dfrac{di}{dt}, \\ L = \dfrac{A\mu_0\mu_r N^2}{\ell}. \end{cases} \tag{1.30}$$

In this ideal case, we see that the emf generated by the coil due to a time varying magnetic field is purely due to its geometry and the permeability of the medium surrounding the coil. Of course when the coil moves inside the motor system, the number of turns $N$, and thus the length of wire $\ell$ surrounding and surrounded by the steel will vary, leading to a dependency of the inductance on the coil position $x$.

In the case of a loudspeaker the coil emf will also be affected by the permeability of the surrounding steel in the motor structure. The motor structure is commonly made using a low carbon steel (American Iron and Steel Institute (AISI) 1006 - AISI 1010) which has a nonlinear relative permeability [8]. The magnetic permeability links $B$ and $H$ where $H$ is the magnetic field strength. If there is an exterior magnetic field, and if the coil is coupled to the steel of the motor, then Equation (1.24) cannot be simplified as in Equations (1.26) to (1.30). If we recall Equation (1.24) for clarity

$$\epsilon(t_0) = -N \int_{\Sigma(t_0)} \frac{d\overrightarrow{\mathbf{B_{tot}}}(t)}{dt}\bigg|_{t_0} \cdot \overrightarrow{\mathbf{dA}}.$$

Due to the dot product in Equation (1.24), only time variations of the magnetic field $\overrightarrow{\mathbf{B_{tot}}}$ in the axial direction of the coil (parallel to the normal of the surface of each turn) will result in a voltage, thus if we observe the directions of $\overrightarrow{\mathbf{B}}$ using a simulation (Figure 1.5) we can see that the magnetic field in the gap ($\overrightarrow{\mathbf{B_m}}$) will contribute very little to the transformer emf. However, the $\overrightarrow{\mathbf{B}}$ inside the red area will have a much larger effect due to the orientation of the vectors and the proximity to the coil. As this $\overrightarrow{\mathbf{B}}$ is inside the steel, it will be subjected to the nonlinear hysteretic relationship between $B$ and $H$, as illustrated in Figure 1.6 for a sample of AISI 1006 low carbon steel. This relationship is usually simplified to an anhysteretic curve as shown in Figure 1.6a, though the actual behaviour is more complex as shown in Figure 1.6b.

The consequence of this nonlinear relation is that the emf due to transformer coupling may also exhibit nonlinear phenomena due the hysteresis and saturation curve of the motor material. Appendix A uses Maxwell's equations to delve further into the effects of eddy currents and mutual inductance.

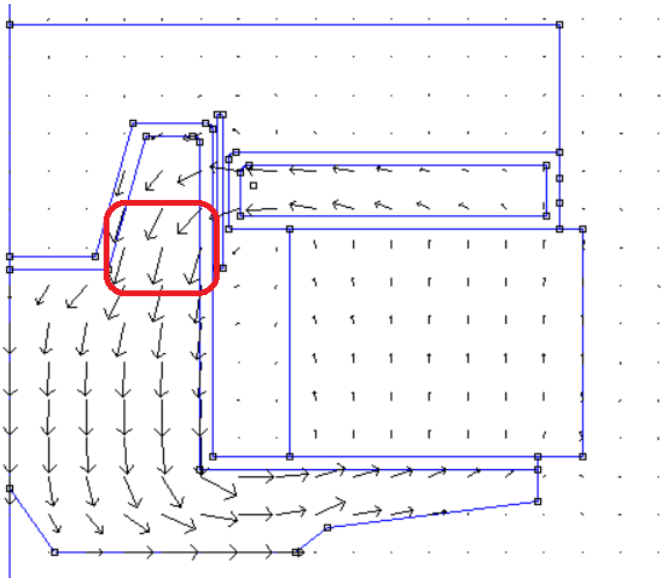

FIGURE 1.5 – Simulation of a loudspeaker motor using FEA. Vectors show the direction of $\overrightarrow{\mathbf{B}}$.

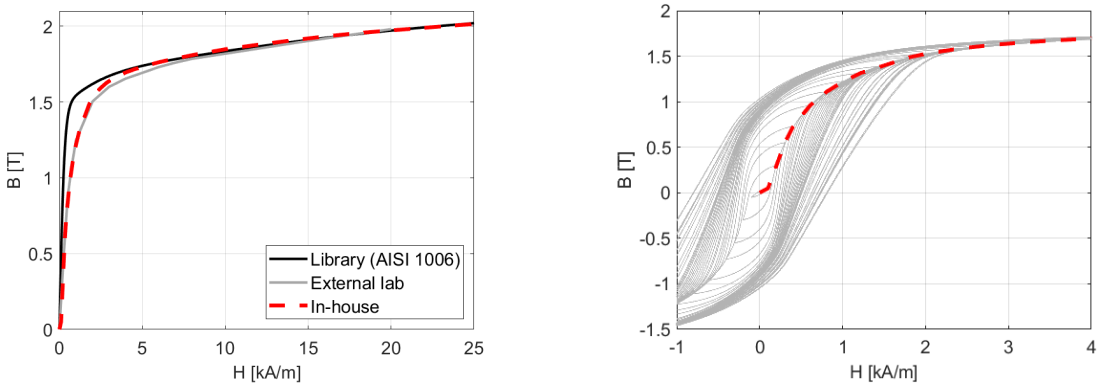


(a) B(H) curves taken from [8].

(b) Hysteresis curves taken from [8].

FIGURE 1.6 – (a) : Anhysteretic B(H) curves. Solid black shows the COMSOL library B(H) curve for AISI 1006 steel, solid grey shows the B(H) curve provided by an external lab for a sample of steel, and red dashed shows the result of an in house (Bowers & Wilkins) measurement. (b) : In house measurement of hysteretic B(H) curves, red dashed shows the resultant anhysteretic approximation. Measurement details in [8].

### 1.4.2 Mechanics

The voice coil is wound onto what is commonly known as the former. It is usually made out of polyimide (DuPont Kapton®), paper, aluminium, or a combination of these materials. The former serves as the main attachment point for most of the mechanical parts as shown in Figure 1.7a. Usually a cardboard ring or collar is used to correctly seat the cone onto the former while also providing a gluing surface. If the former is constructed from polyimide, then a layer of material sometimes called 'Nomex® spunlace' is added as it provides a superior gluing surface compared to polyimide. The force generated in

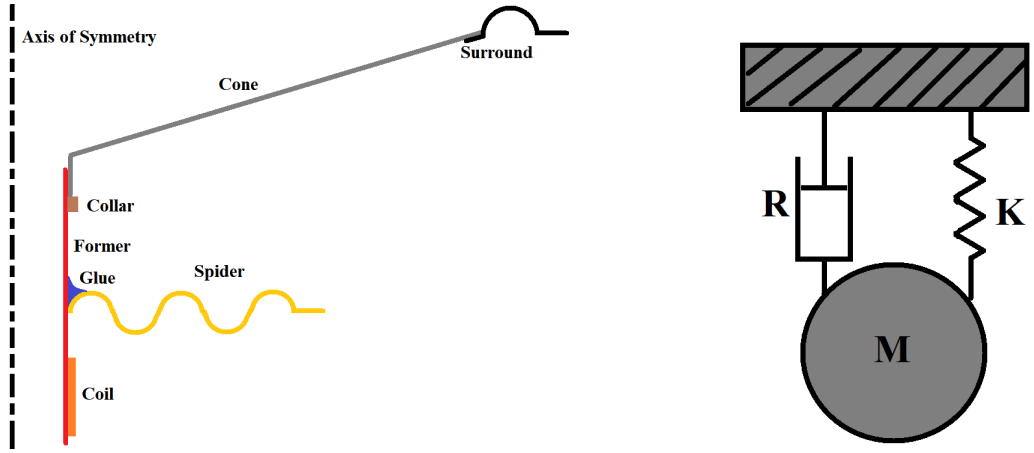


(a) Mechanical system construction example. (b) 1 DOF model.

FIGURE 1.7 – Mechanical System. (a) : Simplified axisymmetric view of the moving parts of a loudspeaker. (b) : Single degree of freedom oscillator, used to represent the loudspeaker moving parts at low frequency.

the voice coil is transferred through the former to the cone, which then moves the air molecules in its vicinity causing sound propagation. The two suspension elements, the spider and the surround, both provide a restoring force that stops the cone from moving too far. Most of the stiffness is provided by the spider, whereas the surround provides an air seal and some radial stability and damping to the cone.

All mechanical systems exhibit resonances and the main resonance in the mechanical system is caused by the moving mass of the assembly and the stiffness of the suspension elements. If we assume that the former and cone behave like perfectly rigid bodies at this resonance frequency, then the simplest representation of our moving assembly is that of a mass-spring-damper system with a single Degree Of Freedom (DOF), as in Figure 1.7b. The spring stiffness K is defined as the ratio between force and displacement, and the damping R is of the viscous sort.

Of course neither the former or the cone are perfectly rigid. The cone, spider and surround all exhibit a variety of different modes [13, 30, 88], and above a certain frequency, the former acts as a spring between the two masses of the coil and cone, thus creating another resonance. There is also the matter of rocking modes where the entire cone assembly may

'rock' axially. Rocking modes are always present, but may become problematic due to mass or stiffness imbalances [17], or even the suspension geometry (personal experience). The issue with rocking modes is that when the assembly 'rocks', the coil may rub against the motor, leading to unwanted noise and even coil failure due to electrical shorts.
As mentioned before, the spider is made from a doped fabric. A woven fabric is doped with a phenolic resin then pressed and heated in a mold. The woven fabric construction means that individual fibres can rub against each other resulting in frictional losses and hysteresis [21, 52, 57]. Furthermore, due to the weave the spider material is not isotropic. The surround material is usually a type of rubber composite, thus some form of polymer which may exhibit viscoelastic behaviour [90, 96] which is characterised by a frequency dependent energy storage (spring) and loss (damper). Another consequence of the viscoelasticity of the surround is creep [85]. Finally the rubber used in loudspeaker surrounds typically includes a percentage of 'fillers' used to modify the hardness of the rubber, in order to increase the stiffness of the surround. The consequences of this filler are the Payne [77] and Mullins [22, 70] effects, as illustrated in Figure 1.8.

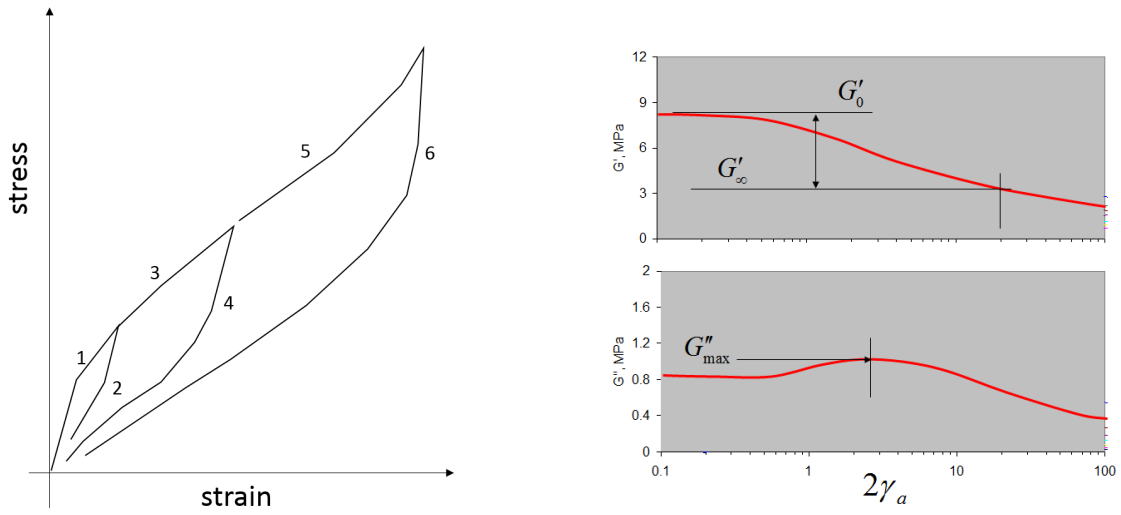


(a) Mullins Effect, image taken from from [5].

(b) Payne Effect, image taken from [62].

FIGURE 1.8 – Mullins & Payne effects. (a) : Mullins effect, where a hysteretic behaviour can be seen between the stress and strain. The material effectively has a memory as the stress depends on the peak strain level. (b) : Payne effect, where the top graph shows the storage modulus (spring) and the bottom graph shows the loss modulus. Above a strain threshold, the storage modulus drops, and the loss modulus exhibits a peak before decreasing.

The Mullins effect can be thought of as a sort of hysteresis, where the stress/strain relationship depends on the previous maximal strain value. The Payne effect resembles a threshold effect, where above a certain strain threshold of approximately 0.1%, the storage modulus (spring) of the material rapidly decreases to a lower limit. In the area where the

storage modulus decreases, the loss modulus increases to a peak value before decreasing again. The end result of these effects is a storage and loss modulus of the material that depend on frequency, previous maximal strain values and instantaneous strain levels.
As with any solid body, the stiffness is the consequence of both the geometry and the material mechanical properties. If we then lump all of the aforementioned phenomena into a single nonlinear spring $K$ and nonlinear viscous damper $R$ as shown in Figure 1.7b, the equations required to correctly represent the behaviour become incredibly complex.
For the same reason, when using finite element analysis software (FEA) to design the suspension elements, the material is considered linear and isotropic, and the stiffness deduced from quasi static simulations. Thus any hysteretic or viscoelastic type behaviour is ignored completely.

### 1.4.3 Acoustics

When approximating the cone as a perfectly rigid body, the far field sound pressure radiated by the cone in an infinite baffle may be approximated by

$$p(r) = \frac{j\omega\rho_{air}S_{cone}}{2\pi}v_{cone}\frac{e^{-jk|r-r_c|}}{|r-r_c|}, \tag{1.31}$$

with $p(r)$ the pressure at point $r$ created by a surface vibrating homogeneously with a velocity $v_{cone}$, $\rho_{air}$ the air density at atmospheric conditions, $S_{cone}$ the surface area of the cone, and $r_c$ the position of the center of the cone. In the frequency domain, a time derivative may be done by multiplying the variable by $j\omega$, thus we may write

$$p(r) = \frac{\rho_{air}S_{cone}}{2\pi}a_{cone}\frac{e^{-jk|r-r_c|}}{|r-r_c|}, \tag{1.32}$$

where $a_{cone}$ is the cone acceleration. Thus in the case of a perfectly rigid cone vibrating in an infinite baffle, the far field pressure is proportional to the cone acceleration. Infinite baffles however are not practical, and as such the drive unit is usually placed inside an enclosure or box. The enclosure serves several purposes. First, it stops the acoustic wave propagating away from the rear of the cone from interacting with the acoustic wave propagating away from the front of the cone. This 'dipole' effect leads to a loss in low frequency output as the two wave cancel each other out due to the phase opposition. Secondly, it acts as an acoustic load for the rear of the drive unit. Thirdly, and perhaps the most important from a sales perspective, it serves to hide all the wires, drive units and components from view while looking incredibly pretty. After all, the loudspeaker will be in a lounge and therefore can be thought of as an expensive piece of furniture that sometimes makes some noise.
In the case where the largest dimension of the enclosure is smaller than the acoustic

wave length ($kL << 1$, where $k$ is the wave number and $L$ is the largest dimension), we may simplify the enclosure types into lumped parameters. The sealed enclosure may be approximated by a spring, while the vented enclosure may be approximated by the parallel association of a spring, mass and damper as shown in Figure 1.9. For Figure 1.9b, $P$ is the air pressure inside the box and $q_{box}$, $q_{vent}$ and $q_{loss}$ are the volume velocities inside the box, vent and interacting with any losses.

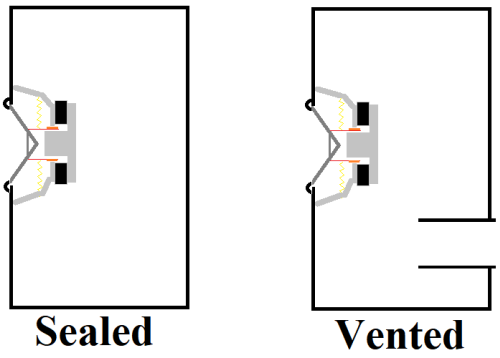


(a) Sealed and Vented enclosures.

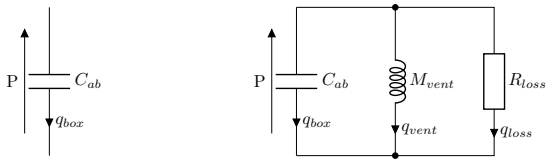


(b) Acoustic Lumped elements.

FIGURE 1.9 – Common enclosure and lumped element models.

In the case of the sealed box, the equivalent air spring $C_{ab}$ may be calculated using

$$C_{ab} = \frac{V_{ab}}{\rho_{air} c^2}, \tag{1.33}$$

where $V_{ab}$ is the enclosure volume, $\rho_{air}$ is the air density and $c$ is the speed of sound in air. In the case of small enclosure volumes and relatively large cone diameters and displacements, the box volume is modulated by the cone displacement leading to a nonlinear air spring [76].

In the case of the vented box, the air spring is calculated using Equation (1.33) while the air mass $M_{vent}$ can be approximated by

$$M_{vent} = \frac{\rho_{air} L_{vent}}{S_{vent}}, \tag{1.34}$$

where $L_{vent}$ is the length of the vent, and $S_{vent}$ is the surface area of the vent. This formula is the simplest expression which may be improved by adding length correction terms.

The damper component $R_{loss}$ is used to approximate the losses inside the enclosure, and is mostly neglected due its low value.

Of course these simplifications are only valid for frequency ranges where $kL << 1$. Above

this threshold, the acoustic volumes are subject to modal behaviour, and the lumped element models need to be turned into distributed element models to correctly predict the behaviour.

Another nonlinear aspect of the vented enclosure is the turbulence due to the air velocity inside the vent. At high output levels, the air velocity inside and around the vent creates turbulence leading to distortion and noise [16, 38, 69, 80].

There are also acoustic effects inside the drive unit itself that may modify its behaviour. Figure 1.10 shows the air paths when the cone moves in the down direction. If there is no venting in the former or the motor, an extra acoustic spring and damper is created. The acoustic spring is mainly due to the air trapped between the cone and the pole, while the air flowing through the gap between the pole & former and the coil & top plate creates a viscous loss. This loss is coupled back into the mechanical domain through the surface area of the cone and is one of the main contributors to the 1 DOF damper.

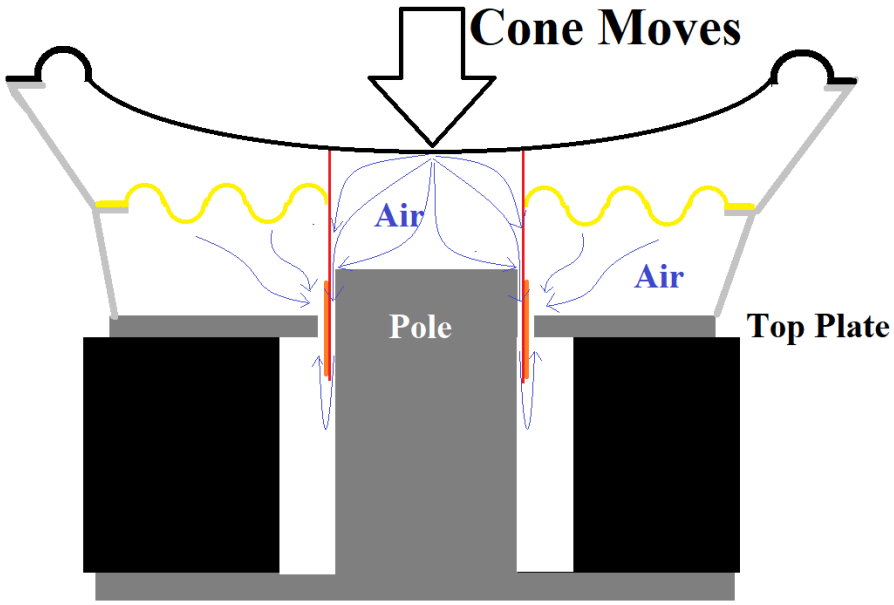


FIGURE 1.10 – Air flow with cone motion.

### 1.4.4 Nonlinearity groups

This first principles section is useful as it sets a foundation for the phenomena in and around the electrodynamic drive unit in an enclosure. It is quite obvious that there are a lot of different sources of nonlinearities present, though they do not all affect the drive unit by the same amount. In this paragraph, they are separated into three groups, 'memory-less', 'dynamic' and 'miscellaneous'. Each group has a rating out of 10 (0 : easy, 10 : impossible) for the complexity of modelling the phenomena and also providing the model parameters.

#### Category I : Memory-less. 3/10

The nonlinear phenomena that can be described as not having a memory are those that depend only on the instantaneous coil position $x$. They are by far the most simple to model and also contribute the most to the measurable distortions. They are the dependence of $B\ell$, the inductance $L$ and the mechanical stiffness $K_{ms}$ or compliance $C_{ms}$ on the coils position $x$.
Figures 1.3a, 1.3b and 1.3c show the magnetic flux lines intersecting with the coil for different positions. It is clear that at ±5 mm, there are less flux lines intersecting with the coil thus resulting in a lower $B\ell$. It can also be seen that the amount of steel contained within the coil increases as the coil descends into the motor. This has the consequence of increasing the inductance of the coil. The actual parameter variations of the motor structure shown in Figures 1.3a to 1.3c are proposed in Figures 1.11a and 1.11b.

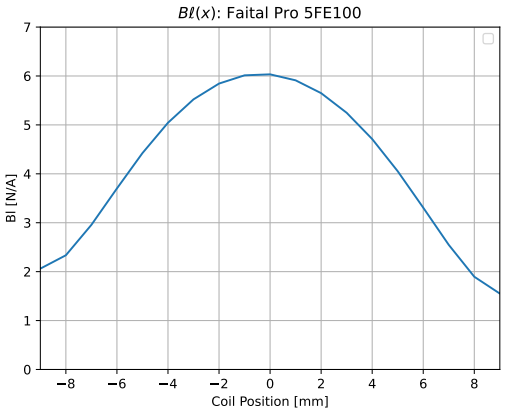


(a) $B\ell(x)$.

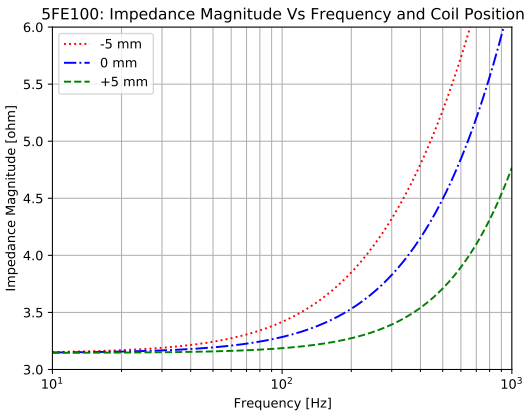


(b) Voice coil impedance magnitude.

FIGURE 1.11 – Spatial variation of electromagnetic parameters for the coil/motor combination in Figure 1.3. (a) : Spatial variation of $B\ell(x)$ for the motor structure shown in Figure 1.3. (b) : Voice coil electrical impedance magnitude for when the coil is positioned 5 mm inside the motor (red dot), at 0 mm (blue dash dot) and 5 mm (green dashed) outside the motor structure of Figure 1.3, 0 mm is the rest position.

In the case of the suspension, the mechanical stiffness increases as the coil moves away from its rest position inside the magnetic gap. Figure 1.12a shows how the suspensions are stretched when the coil moves away from its rest position, and Figure 1.12b shows a measured $K_{ms}$ curve. Therefore, in this category are :

— spatial variation of $B\ell(x)$,
— spatial variation of spring stiffness $K_{ms}(x)$,
— spatial variation of coil inductance $L(x)$.

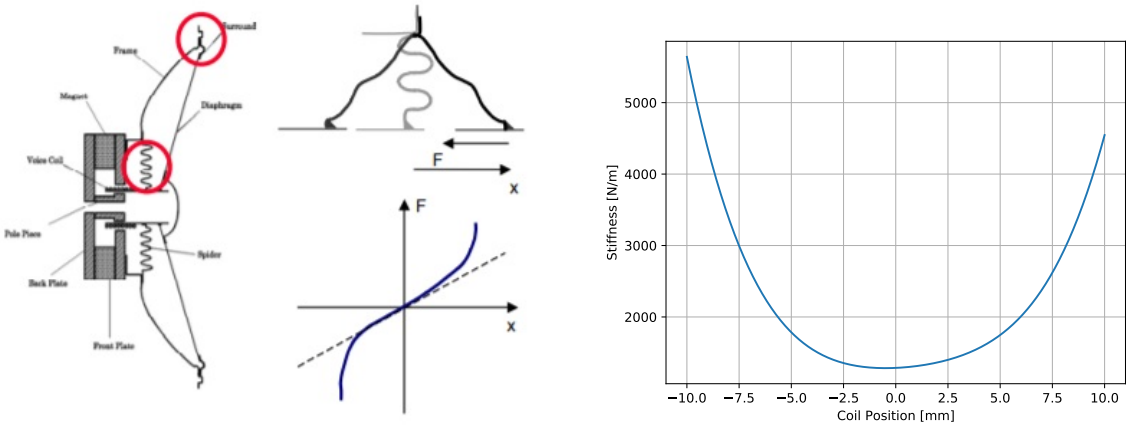


(a) Suspension nonlinearity, taken from [47].

(b) Measured $K_{ms}$.

FIGURE 1.12 – Suspension nonlinearity and measurement. (a) : Example of how the geometry changes when the suspension is stretched and the resulting force/displacement curve. (b) : Example of a measured $K_{ms}$ curve for a drive unit.

### Category II : Dynamic Nonlinearities. 7/10

Whereas the nonlinearities in the previous section are relatively easy to measure, simulate and model, the nonlinearities presented in this section are not. In this category are placed notable phenomena such as hysteresis, frequency dependency and component ageing. Hysteresis is present in both the electromagnetic part of the loudspeaker [8], as well as in the mechanical part [52, 60]. The hysteresis nonlinearity is unfortunately also coupled to a frequency dependency due to eddy currents [19, 98], or the viscoelastic properties of the surround [45, 74].
The component ageing mostly affects the suspension elements, particularly the spider. The spider is usually a doped fabric, where the fabric is doped with phenolic resin and then pressed and heated into the final form. With use, the resin bonds break leading to a decrease in the mechanical stiffness, while also changing the hysteresis loop.
Due to the nature of these nonlinearities, it is challenging to measure them, but it is harder still to model them with any degree of accuracy and with simple maths. Therefore in this category are :

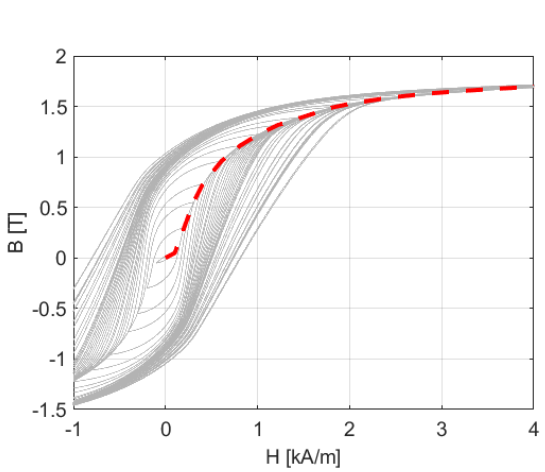


(a) Electromagnetic hysteresis, taken from [8].

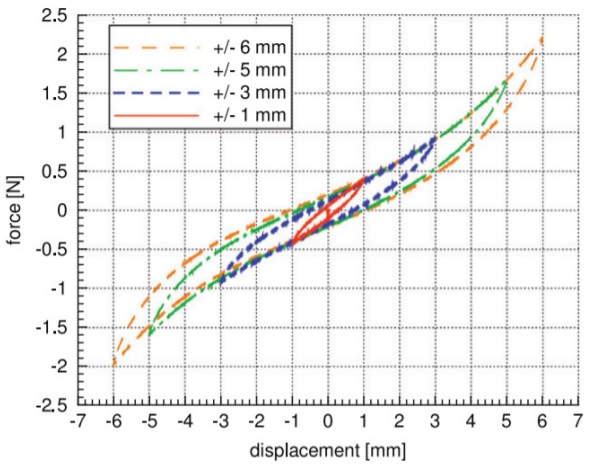


(b) Mechanical hysteresis, taken from [61].

FIGURE 1.13 – Hysteretic Nonlinearities. (a) : Electromagnetic hysteresis measured in a sample of AISI 1006 low carbon steel, where the grey curves show the hysteresis loops, and the red dotted line illustrates the anhysteretic B(H) curve. (b) : Mechanical hysteresis measured in a drive unit suspension (surround and spider) at four different peak displacement levels. Red solid indicates ± 1 mm, blue dashed indicates ± 3 mm, green dash dot indicates ± 5 mm, and red long dashed indicates ± 6 mm.

— mechanical viscoelastic effects,
— mechanical hysteresis,
— mechanical component ageing,
— electromagnetic hysteresis,
— coupling between electromagnetic hysteresis and eddy currents.

### Category III : Miscellaneous. 10/10

There are also a variety of other factors that may severely hamper the linearity of the drive unit, but which are impossible to model with the current methods. For example, the process used to create the spiders may induce residual stresses in the geometry. Personal experience has shown this leads to the spider being shaped like a Pringles crisp rather than a disk, leading to issues during assembly of the drive unit. Another issue, again related to the suspension is the sensitivity of some rubbers to Ultra Violet (UV) light. Some rubbers can harden under the influence of UV leading to a loss in bass or even the destruction of the drive unit.
Other phenomena also belonging to this category are small children, drunk friends, and pets. Therefore, phenomena belonging to this category are :

— rocking modes,
— modal behaviour of cone, suspension and spider,
— fabrication defects,

— UV light
— human interaction.

## 1.5 Control Methods

In the aim of improving the performance of a loudspeaker system, several techniques have been tried over the past decades. The first techniques relied on analog feedback in an attempt to increase the amount of bass and reduce distortion. A variety of different techniques have been proposed included current feedback [7, 81], velocity feedback [53] and acceleration feedback [12, 37]. There were also techniques which used both current and velocity feedback [32, 68]. Of course, the main difficulty with most of these approaches is the need for a suitable sensor to provide the feedback signal. Various ways of sensing coil displacement [11, 31], velocity [68], or acceleration exist today. Adding a sensor to the loudspeaker is not always trivial [35, 68], and may render the assembly of a smaller drive unit rather complex and result in a lower efficiency due to the added mass.
Another more recent technique involves feed forward. The idea being to predistort the stimulus in such a way that the distortion generated by the loudspeaker is reduced. There are many ways to do this [10, 14, 29, 46, 49, 58, 79, 86, 94]. The main challenge when dealing with feed forward routines is the accuracy of the model chosen to approximate the drive unit behaviour.

### 1.5.1 Feedback

An observation of the physical principles of the electrodynamic loudspeaker shows that the force applied to the mechanical system is dependent on the voice coil current, $i$, not the voice coil voltage, $u$. Thus the premise of using feedback to control the current flowing through the voice coil rather than the voltage applied to the terminals was a logical step. Most amplifiers on the market attempt to act as voltage sources. They can be characterised by a high input impedance, and a very low output impedance. The output voltage is an amplified version of the input voltage. Controlling the current requires that the output impedance be at least an order of magnitude higher than the load impedance, and as most signals are voltage based, the input impedance must also be high. This type of amplifier is called a transconductance amplifier, and its gain is characterised as Ampères per Volt, or Siemens. A true current amplifier would be characterised by an extremely low input impedance and an extremely high output impedance. Figures 1.14a and 1.14b show the basic circuit configurations for creating a voltage or transductance amplifier.

#### Analysis

References [7, 81] both perform an analysis on the effects of using current drive on the distortion generated by an electrodynamic loudspeaker. The work described in [81] is

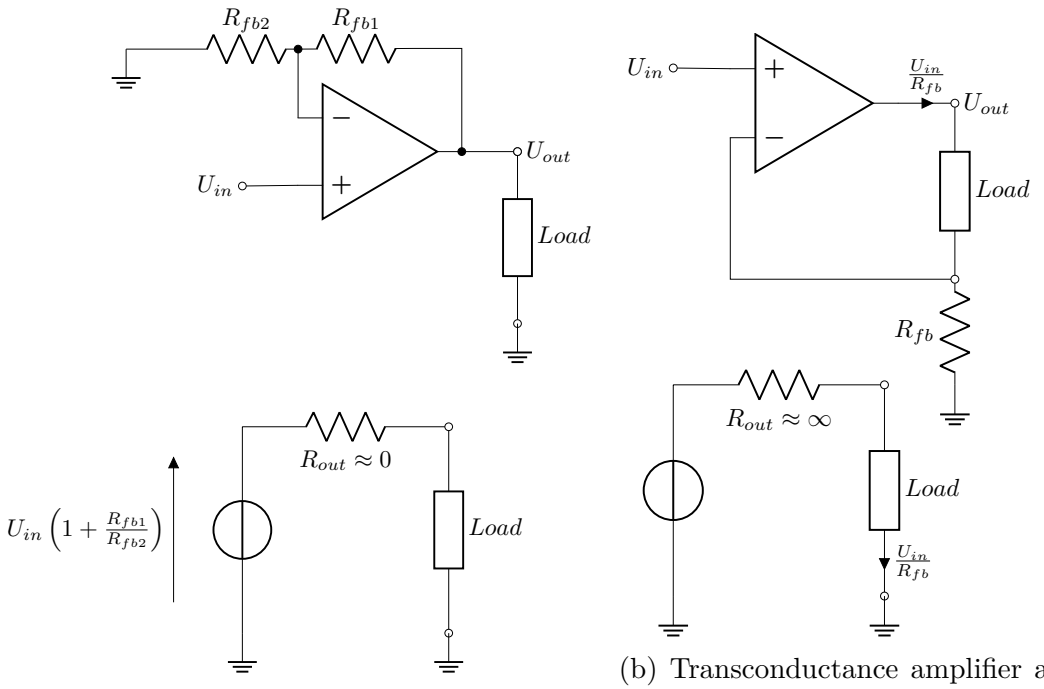


(a) Voltage amplifier and Thevenin equivalent

(b) Transconductance amplifier and Thevenin equivalent

FIGURE 1.14 – Equivalent circuits for voltage and transconductance amplifiers. (a) : Ideal voltage amplifier and its Thevenin equivalent. (b) : Ideal transconductance amplifier and its Thevenin equivalent.

limited to very low powers and only uses sine waves and two tone measurements to assess the effect of the amplifier output impedance, whereas [7] performs multitone tests and looks at how the component tolerances affect the output of an electrodynamic loudspeaker when the amplifier has a low output impedance, a negative output impedance, and a positive output impedance. An interesting idea presented in [7] was the use of a frequency dependent output impedance to provide damping around the resonance frequency, and current drive above the resonance. The result was more linearity in the mid range and a higher resilience to the component tolerances when compared against amplifiers with frequency independent output impedances.

Another type of feedback is velocity feedback. There are a variety of different ways of obtaining a signal that represents the velocity of the voice coil using secondary coils [68], integrating the signal from an accelerometer [32] or utilising the voice coil current and velocity [53]. From a production perspective, adding a secondary coil or an accelerometer to a product increases the complexity and thus the cost and assembly time. The additional mass can also reduce the system sensitivity leading to increased power dissipation. It is also shown in [68] that the coupling between the voice coil and the sense coil must be compensated for the correction to be correctly applied. Figure 1.15 shows the circuit used to apply the velocity error correction. Box A is the circuit responsible for compensating the mutual coupling between the sense and voice coil, and box B shows the circuit used to condition the output of the sense coil.

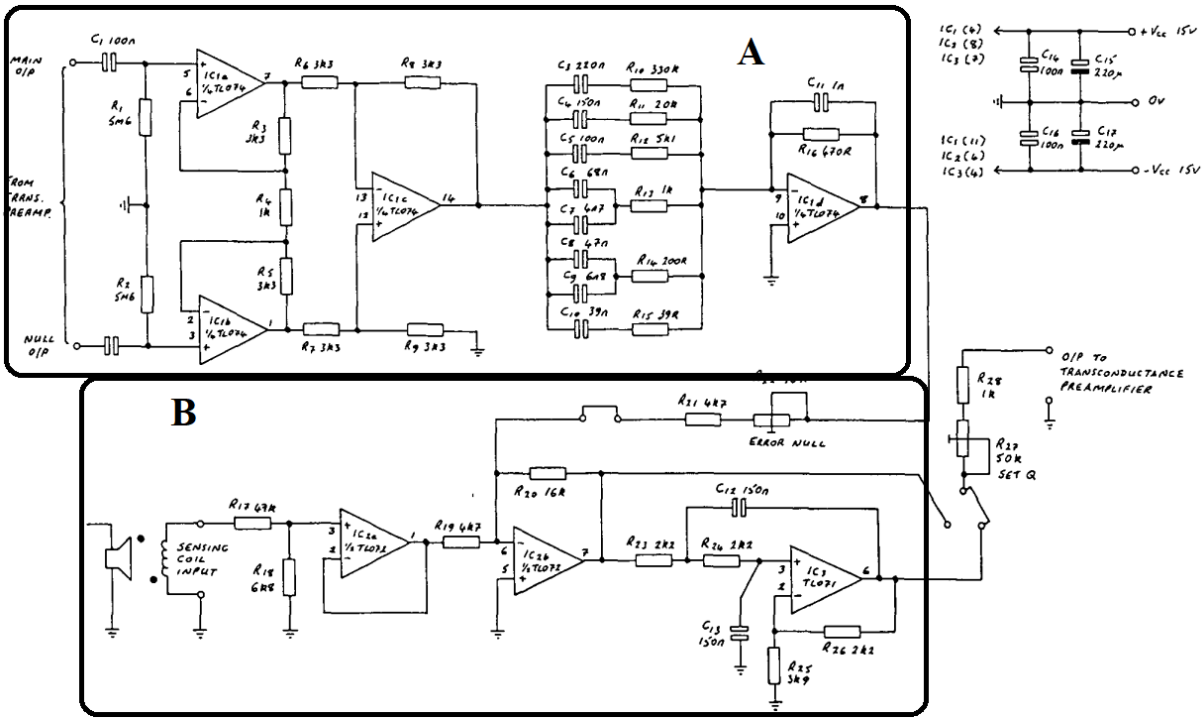


FIGURE 1.15 – Secondary voice coil signal conditioning circuit extracted from [68].

One of the main points of interest in this article is the discussion around the circuit topologies used to design a transconductance amplifier. The power amplifier circuit proposed was used as an inspiration for the power amplifier circuit designed during this thesis and detailed in Appendix D.

In [32] the signal from an accelerometer is integrated to generate the velocity signal, however the integration of real world signals is always problematic with regards to the amplification of low frequency signals. The circuit proposed is shown in Figure 1.16. Resistors $R_3$ and $R_4$ provide the current feedback, and the op amp with $C_1$, $R_5$, $R_6$ and $R_7$ provide the velocity signal through integration of the accelerometer signal. In order to reduce any issues related to the integration of low frequency signals, the parallel association of $C_1$ and $R_6$ effectively reduces the low frequency gain of the integrator which would be infinite if $R_6$ were omitted. References [12, 35, 37] all discuss the use of direct acceleration feedback in the aim of linearising the output of a loudspeaker system. Although [37] is rather brief, it does discuss the compromises encountered when trying to render a loudspeaker system as compact as possible while keeping the bandwidth high and distortion low. A more in depth analysis of an accelerometer based feedback system can be found in [12]. There are two main points of interest in this article. The first is that even though the Digital Signal Processor (DSP) version of the controller was far easier to tune, the inherent system latency of 100 $\mu$s induced a phase shift at higher frequencies that would impair the efficiency of the control loop. The second point is the effectiveness of the final closed loop system. In Figure 1.17, it is clear that although the control loop

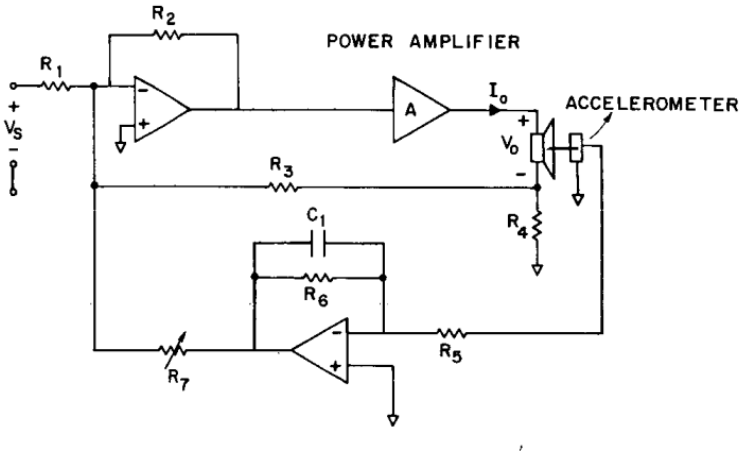


FIGURE 1.16 – Circuit for the integration of the signal from an accelerometer and mixing with current feedback, extracted from [32].

reduces distortion below 100 Hz, it increases it between 100 Hz and 800 Hz.

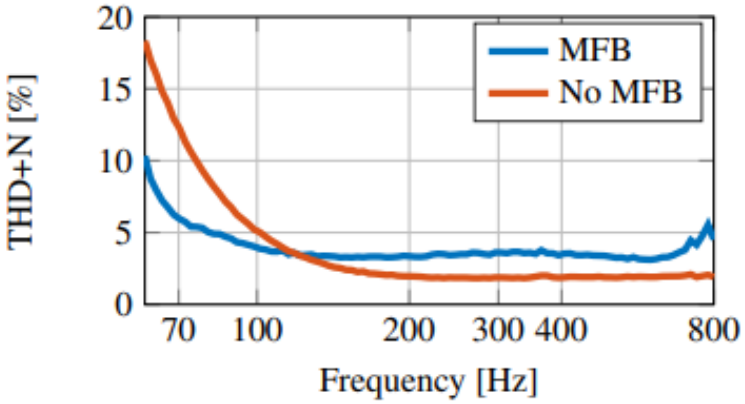


FIGURE 1.17 – Effect of applying MFB to linearise a loudspeaker. THD+N is reduced below and around the resonance frequency but increased above. Figure extracted from [12].

Finally Hall goes very in depth into the practical aspects of implementing an accelerometer based feedback system [35]. The discussion talks about the general aspects of feedback loop stability, but more interestingly goes into detail about the compromises in mounting the accelerometer to the cone. Details that stand out are ; (a) at low frequencies the accelerometer is susceptible to pick up the signal resulting from the strain imposed on the cone from the air pressure inside the enclosure resulting in a bump or a notch in the frequency response, and (b) the combination of high temperatures and magnetic fields means that a loudspeaker is not necessarily the ideal system in which to mount an accelerometer.

**Feedback Summary**

There are a variety of different feedback techniques that may be applied to a loudspeaker, each with its own set of compromises and advantages. Current feedback is by far the simplest arrangement as it only requires a slight modification of the power amplifier. There is no need to worry about the extra cost and complexity of mounting a sensor inside the loudspeaker, or how the sensor will interact with the loudspeakers behaviour. It automatically removes the influence of voice coil heating and most inductive nonlinearities, such as hysteresis and spatial variations. The main disadvantage of current feedback is the lack of damping at the resonance frequency and thus a high sensitivity to variances in the suspension system. One solution is to make the amplifier output impedance frequency dependent, this does however induce extra components into the system. It may be possible to couple current feedback with the topic of the next section, feed forward.

### 1.5.2 Feed forward

The premise of feed forward or predistortion methods is simple. If you know how the system behaves, you can predistort the input signal so that the nonlinearities are effectively cancelled out. This does however entail the necessity of being able to accurately predict the behaviour of the system over time. References [10, 14, 29, 51, 79, 86, 94] all propose different ways of implementing a feed forward linearisation scheme.
In guise of an example of a feedforward system, we imagine a single degree of freedom mechanical oscillator of mass $M_{ms}$, damping $R_{ms}$ and spring stiffness $K_{ms}$. The force $F(t)$ applied to this system is proportional to a current $i(t)$ through the coupling factor $B\ell$. Both the coupling factor $B\ell$ and the spring stiffness $K_{ms}$ are nonlinear functions of coil position $x$, and may be represented by $2^{nd}$ order polynomial functions

$$\begin{cases} B\ell(x) = B\ell_0 + B\ell_1 x + B\ell_2 x^2, \\ K_{ms}(x) = K_{ms_0} + K_{ms_1} x + K_{ms_2} x^2. \end{cases} \tag{1.35}$$

We assume that the model is 100% accurate for this example, and that the oscillator is excited by a current source. The acceleration of the oscillator is to be linearised and made to match a target acceleration $\ddot{x}_T(t)$. If we write the differential equations of a single degree of freedom mass-spring oscillator

$$F(t) = M_{ms}\ddot{x}(t) + R_{ms}\dot{x}(t) + K_{ms}x(t), \tag{1.36}$$

we see that the force $F(t)$ is proportional to the acceleration $\ddot{x}(t)$, velocity $\dot{x}(t)$ and displacement $x(t)$ of the mass. Thus the force $F_T(t)$ to be applied to our nonlinear oscillator

to impose the target acceleration $\ddot{x}_T(t)$ is

$$F_T(t) = M_{ms}\ddot{x}_T(t) + R_{ms}\dot{x}_T(t) + K_{ms}(x_T)x_T(t). \tag{1.37}$$

We then work back to the required current $i_T(t)$ using

$$F_T(t) = B\ell(x_T(t))i_T(t), \tag{1.38}$$

giving

$$i_T(t) = \frac{F_T(t)}{B\ell(x_T(t))}. \tag{1.39}$$

We can see that when $K_{ms}(x)$ increases so does the force, and when $B\ell(x)$ drops the current increases. The nonlinearities are thus cancelled out by the model. This example shows the main idea behind the inverse dynamics or model inversion principles of feed forward compensation.

### Analysis

In [10] an inverse dynamics or predistortion scheme is coupled with accelerometer based feedback, as shown in Figure 1.18, in the aim of linearising systems with small drive units. While the approach is interesting, the issues with placing an accelerometer inside the drive unit are still present along with the addition of latency incurred by the DSP implementation.

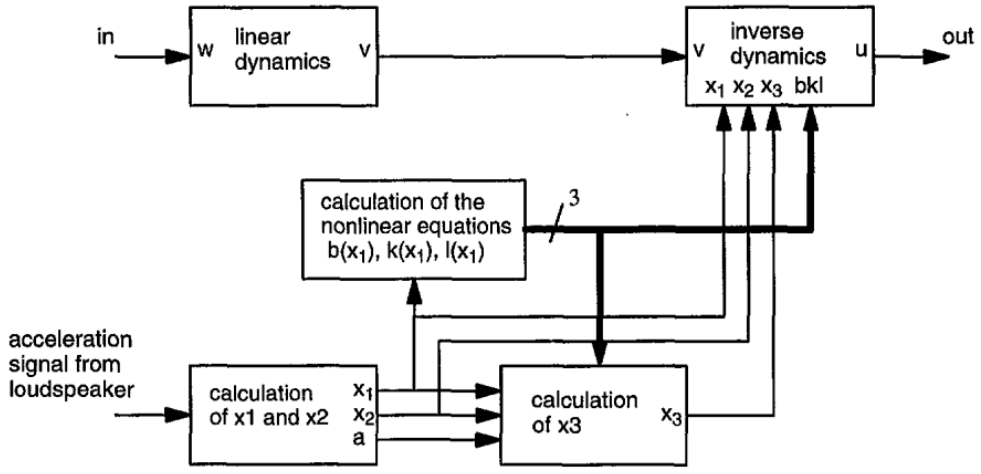


FIGURE 1.18 – Taken from [10].

A comparison of two different feed forward methods is performed in [86], concluding that the inverse dynamics method performs better than the direct nonlinear controller. The linear parameters are fitted to impedance measurements, while the nonlinear parameters

are fitted using sound pressure distortion measurements. Even though the results are interesting and promising, there are two issues present. The first issue comes from the use of only the $2^{nd}$ and $3^{rd}$ harmonics to quantify the performance of the linearisation scheme. There is no discussion of inter modulation distortions or the use of more complex signals. The second issue stems from the way the parameters are fitted. To obtain the results in this article, one would be required to perform impedance and sound pressure measurements over time in order to keep the model updated, and even if this could be automated, the measurement of sound pressure in an arbitrary room would impose additional challenges. Reference [79] uses simulations to observe the impact of component variations due to heating, concluding that an adaptive controller is needed if the compensation is to be efficient. Although the cited distortion reduction from 20 % to 1 % seems like an excellent result, it is only in the case of the model used in the simulations. The model is incredibly simple and does not include hysteresis, eddy currents, or component ageing. Flatness and

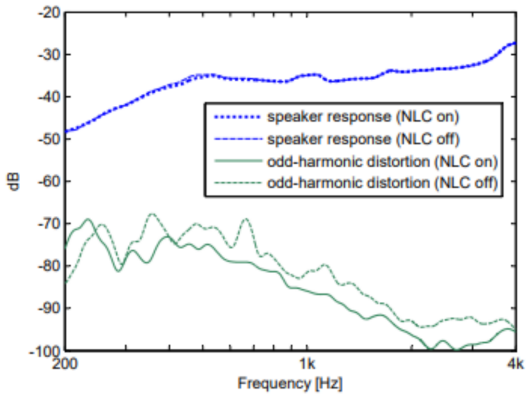


(a) Comparison of odd-harmonic distortion for a microdriver with NLC on and off, multitone measurement.

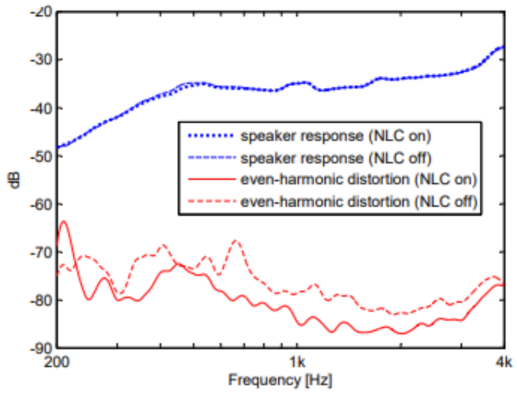


(b) Comparison of even-harmonic distortion for a microdriver with NLC on and off, multitone measurement.

FIGURE 1.19 – Effect of NLC on the odd (a) and even (b) harmonic distortion when applied to a microdriver, from [14].

trajectory planning is a technique proposed in [25] via the port Hamiltonian approach, however only simulations and a single frequency is used to assess the methods. Later, the same concept is used via a nonlinear state space model in [14] to perform the inverse dynamics. The wanted sound pressure is used to calculate the required coil displacement, velocity and acceleration. These quantities are then fed into a nonlinear equation and the required voltage is then calculated. The nonlinearities taken into account are the inductance, force factor and compliance. These are all represented as polynomial functions, and the actual values are updated in real time using the coil current. The performance of the correction algorithm is then evaluated using sine waves, multitone signals and musical signals using the Non coherent distortion metric [91]. For all stimuli, the average reduction in distortion seems to be between 6 and 10 dB, an example being shown in Figure 1.19.

The discussion around the requirements for the amplifier is particularly interesting. The correction algorithm increases the signal crest factor by around 6 dB leading to higher voltage peaks, and also requires the ability to output frequencies below 1 Hz. Simply increasing the voltage rails of the amplifier can lead to increased losses in the output stage, thus some sort of adaptive system would be required [102]. Another important remark is that the time derivatives required by the algorithm are susceptible to noise issues and thus required some sort of filtering. Adaptive Finite Impulse Response (FIR) filtering is used in [29] to provide the nonlinear compensation. Several methods are compared in terms of error, and the frequency weighted inverse filter method was used to assess the compensation when applied to a simulation model, giving a claimed overall reduction of 14 dB. With this work, we again see the trend of using adaptive algorithms in the compensation scheme. In [51] a mirror filter method for the compensation of nonlinearities

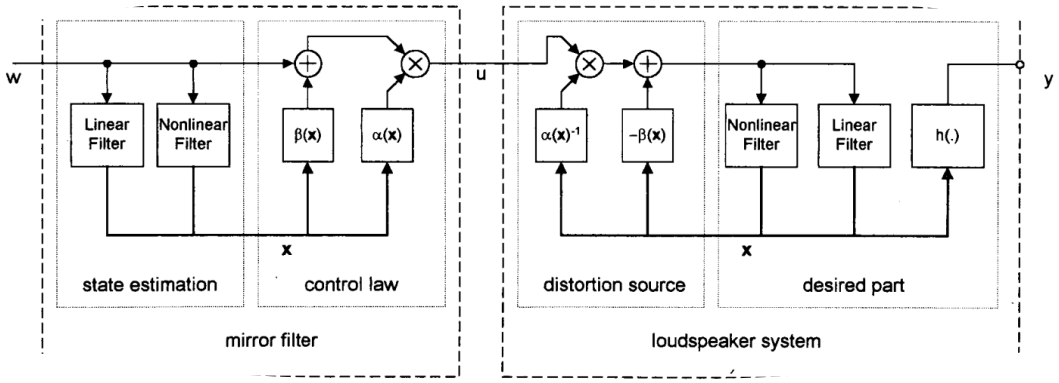


FIGURE 1.20 – Mirror filter for woofer systems [46].

is proposed, as shown in Figure 1.20 and an in depth analysis is performed. Both objective and subjective tests are performed to quantify the effectiveness of the algorithm. The objective results show that if the sound pressure is used to update the model parameters then approximately 12-20 dB of correction can be obtained. Using information from the drive unit terminals (voltage / current) proved to be less effective due to the difficulty of separating out the nonlinear effects. The subjective results vary, and depend heavily on the musical stimulus and its frequency content. A different approach is proposed in [58], with the use of neural networks instead of physical models. The neural network was trained using an approximation of the instantaneous cone displacement by integrating the instantaneous cone velocity, deduced using the drive unit terminal voltage and current. The work focuses mainly on simulations and thus there is no discussion about hardware implementations or the effectiveness on an actual drive unit. Finally, an extension to the mirror filter formulation is proposed in [94] by adding in a fractional derivative term to take into account the visco-elasticity of the suspension. The additional term provides a more effective compensation below 200 Hz as shown in Figure 1.21. However, the use of fractional derivative models requires more processing power and memory which may not

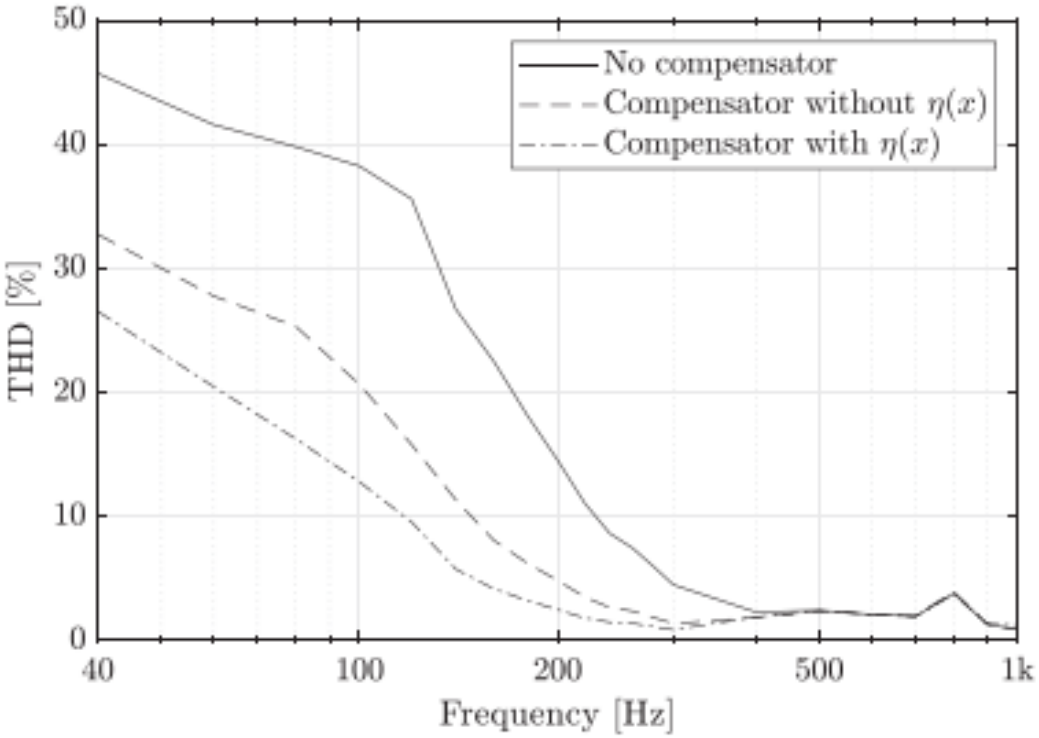


FIGURE 1.21 – Effect of taking the visco-elasticity effects into account for the compensation [94]. Solid line : No compensation. Dashed line : Compensation without visco-elastic effects. Dash Dot : Compensation with visco-elastic effects.

be worth the investment for such a slight improvement in compensation. Furthermore, there is no discussion about the hardware used to calculate the fractional derivative in real time, which is a shame.

**Feed forward Summary**

All of the feed forward methods are in fact hybrid methods, in that the feed forward algorithm is coupled together with a feedback loop. Most of the time the feedback loop is used to update or fit the feed forward model parameters to the drive unit sample. In order to reduce the system complexity and avoid any issues with feedback sensors, the feedback variables of choice are the drive unit current and voltage. Both of these quantities may be easily measured with simple and low cost circuits, which is a major advantage for industrial applications.
The compensation efficiency seems to be on average around 10 dB. However it is difficult to provide a statistically relevant figure as some of the publications just use sine wave tests, some use multitone, while others are just simulation results.
The overall preferred method of modelling the loudspeaker was with a state space type model, using a system of differential equations with linear and nonlinear parameters. The

nonlinear parameters are almost always in the form of a polynomial functions of varying degree.
The model itself is the most important aspect of the feed forward method of compensation, thus the next section will concentrate on providing an overview of the available models.

## 1.6 Nonlinear Models

A loudspeaker drive unit, although rather simple and consisting of only a few components, exhibits a variety of different nonlinear phenomena which must be modelled if they are to be compensated. The electrodynamic loudspeaker is at heart a transducer, it therefore transforms one form of energy into another. The input energy is electrical and the output is acoustical by way of a mechanical system.
This chapter discusses and illustrates the various methods and models available for approximating the behaviour of an electrodynamic loudspeaker. Because the model needs to be run in real time, simplicity is the most important aspect, thus only single degree of freedom models will be discussed. The models are be divided into their respective physical domains, electromagnetic or mechanic, with the acoustical load of the enclosure lumped into the mechanical domain.
First the different models are briefly analysed, followed by a short section on the maths required to run the models.

### 1.6.1 Physics based models

The are many ways of representing the linear and nonlinear behaviour of a drive unit. It is common to separate the models into 3 types, white box, grey box and black box. Black box models tend to have a set of parameters that have no link to the actual physics of the system. Some examples would be a neural network [58] or block orientated model such as Hammerstein, Wiener or their generalised forms [34]. White box models tend to have a set of parameters that are actual physical quantities. An example would be the differential equations of a mass on a spring, based on Newtonian physics. Grey box models are all those that fall in between.
For this thesis, the white box or physics based approach is preferred because the models are easier to understand as the link between the model and the real system is more obvious, and most of the parameters can actually be measured.

**Electromagnetic Domain**

If we recall the electromagnetic part in the first principles section, then we can list the prerequisites for the model :

— electrical resistance $R_e$, due to coil wire length [Ω],
— inductance $L$, due to electromagnetic coupling [H],
— back EMF due to coil motion [V],
— force generation due to Lorentz force [N].

A common way of representing the models is through electrical circuit analogies, an example of which is shown in Figure 1.22. These circuits can also be converted to/from a

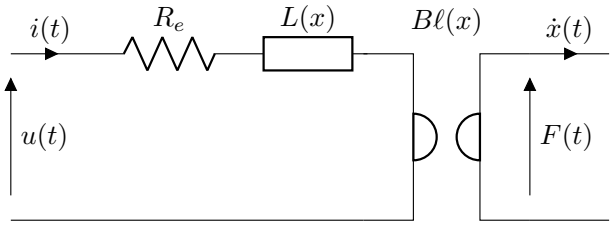


FIGURE 1.22 – Basic Electromagnetic model.

set of differential equations

$$\begin{cases} u(t) = R_e i(t) + \dfrac{dL(x)i(t)}{dt} + B\ell(x)\dot{x}(t), \\ F(t) = B\ell(x)i(t). \end{cases} \tag{1.40}$$

The wire resistance is simply a resistor that may or may not be temperature dependent where the dependency is modelled as [50]

$$R_e(T_v) = R_e(T_{amb})(1 + \delta_{wire}(T_v - T_{amb})), \tag{1.41}$$

where $R_e(T_v)$ is the resistance at the temperature $T_v$, $R_e(T_{amb})$ is the resistance at the temperature $T_{amb}$ and $\delta_{wire}$ is the temperature coefficient of the voice coil wire.
The coupling between the magnetic and mechanical domain is through the $B\ell v$ and $B\ell i$ terms. It is common to represent the $B\ell$ term as a polynomial function in order to take into account the variation with coil position $x$

$$B\ell(x) = B\ell_0 + B\ell_1 x + B\ell_2 x^2 + B\ell_3 x^3 + B\ell_4 x^4 + ... + B\ell_N x^N. \tag{1.42}$$

The inductance $L$ is the part of the model with the most research. As exposed in the first principles section and Appendix A, there are a lot of different linear and nonlinear phenomena at work.
In order to represent the frequency dependency of the inductance due to eddy currents,

there are two ways of proceeding ; Foster type networks [27] or Fractional derivatives [4, 55, 92, 98]. The Foster type models are from the theory of network synthesis where the frequency dependent component is modelled by a series of frequency independent components. The fractional derivative type models are from the more recent interest into fractional calculus, where the voltage $u_l(t)$ across a fractional inductance $L^\alpha$ of order $\alpha$ may be written

$$u_l(t) = L^\alpha \frac{d^\alpha i}{dt^\alpha}. \tag{1.43}$$

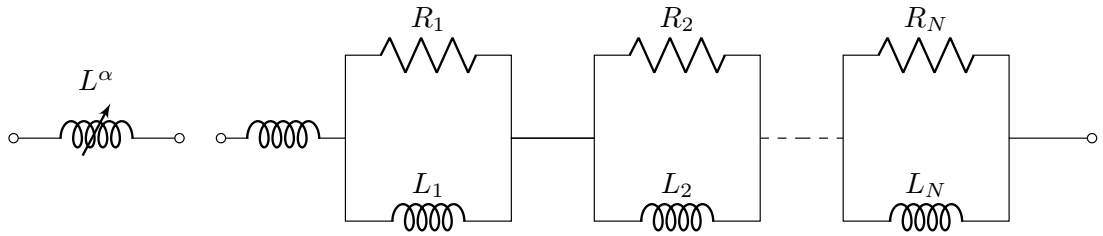


FIGURE 1.23 – Fractional inductor and equivalent Foster type I network.

A reduced version of Foster network shown in Figure 1.23 is more commonly known in the audio industry as the $RL_2$ or $R_2L_2$ model [23, 47]. It has been made popular through the Klippel Large Signal Identification (LSI) module and associated hardware. Shown in

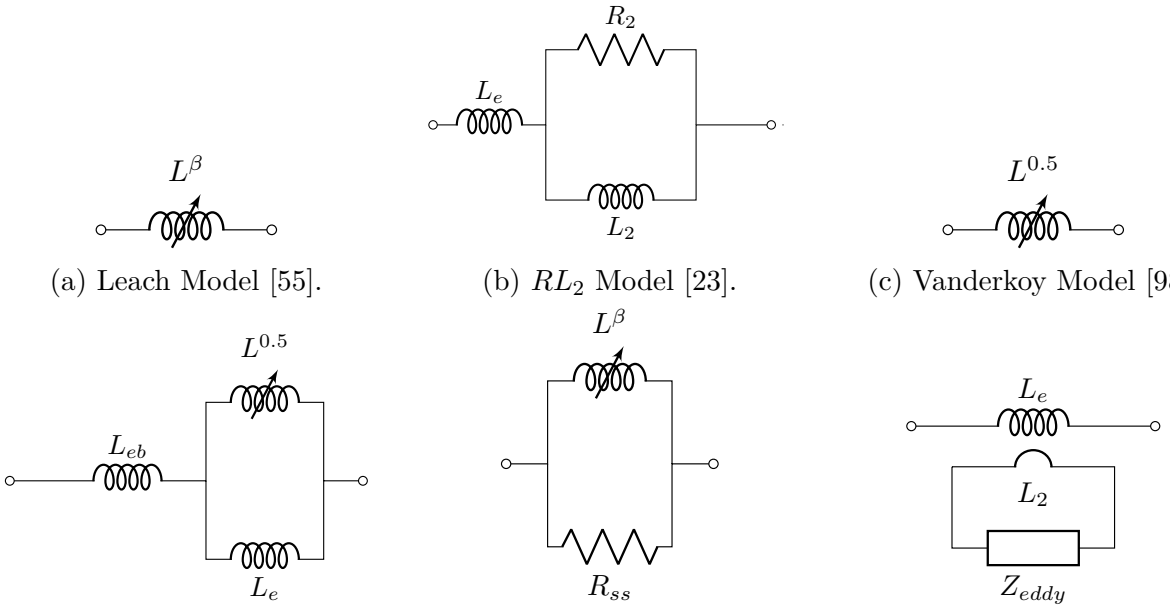


(a) Leach Model [55]. (b) $RL_2$ Model [23]. (c) Vanderkoy Model [98].

(d) Thorborg Model [92]. (e) King Model [45]. (f) Anazawa Model [4].

FIGURE 1.24 – Common Inductance Models.

Figure 1.24 are six common inductance models, of which only one uses purely frequency independent components. Of the models, only the $RL_2$ and King model have been used to model both the nonlinearities due to frequency and position dependence [23, 43, 45]. In

terms of real time compensation, use of the $RL_2$ or Foster type models is preferable with today's technology, as the memory requirements of fractional calculus represent a heavy computational and memory burden [94]. A less well known but rather interesting approach is to model the electromagnetic domain separately via the "capacitor gyrator" approach [24, 36]. This approach can be interesting from the physics point of view, but ultimately electrical domain equivalencies of the electromagnetic models may be constructed that resemble some of the more common electrical equivalent circuits and shown in Figure 1.24.

Another aspect of the nonlinear inductance is the reluctance force. It is a purely nonlinear addition to the Lorentz force that is created by the spatial variation of the inductance [49, 72, 84]. In the guise of a simple example, let us assume we have a frequency independent inductance $L$, which only depends on the position in space $x$. In this case, a force is developed that can be approximated with

$$F_{rel} = \frac{1}{2}\frac{dL}{dx}i^2, \tag{1.44}$$

where $F_{rel}$ is the reluctance force and $i$ is the current flowing through the inductance. In the case of the $RL_2$ model it is not particularly difficult to analytically calculate the reluctance force using the energy balance method [72], however this method becomes quite complex when dealing with fractional order components [28].

An additional phenomena introduced in the first principles section is electromagnetic hysteresis. In [8] it was shown that in order to correctly model the current distortion due to the inductance, the hysteresis needed to be taken into account. A polynomial type model for the minor hysteresis loop was proposed in [64], where the magnetic flux $\phi$ is made dependent on both coil position $x$ and coil current $i$

$$\phi(x,i) = aL(x)i^3 + bL(x)i^2 + cL(x)i + dL(x), \tag{1.45}$$

where the coefficients $a, b, c, d$ are to be determined through measurements of the flux and current. It should be noted that in order to reproduce the hysteresis loop, the $b$ and $d$ coefficients have a sign that depends on the sign of the derivative of the current. For example if $i$ is increasing $b$ may be positive and $d$ negative, while $i$ is decreasing $b$ may be negative and $d$ positive. Even though this model is relatively simple compared to other models of electromagnetic hysteresis [41, 59, 82], it is the measurement of the parameters that may cause issues, especially if they are to be optimised in real time. A brief discussion on the methods used to measure the hysteresis loops of a steel sample is provided in [8]. Overall, the inclusion of hysteretic nonlinearities in a model designed to be run in real time represents quite a challenge from both the equations point of view and also the parameter fitting point of view.

**Mechanical Domain**

If we recall the mechanical part in the first principles section, then we can list the prerequisites for the model :

- Mechanical resistance $R_{ms}$, due to viscous losses $[N.s.m^{-1}]$
- Mechanical stiffness $K_{ms} = \frac{1}{C_{ms}}$, due to the suspension elements $[N.m^{-1}]$
- Mechanical mass $M_{ms}$, due to the moving assembly $[kg]$

An analogous circuit of the 1 DOF oscillator is shown in Figure 1.25. This circuit can also

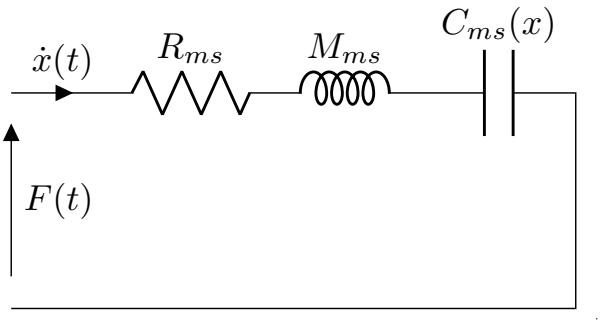


FIGURE 1.25 – Basic Mechanical model.

be converted to/from a differential equation

$$F(t) = M_{ms}\ddot{x}(t) + R_{ms}\dot{x}(t) + K_{ms}(x)x(t). \tag{1.46}$$

Usually, the only nonlinear parameter in the mechanical domain is the suspension stiffness $K_{ms}$ (compliance $C_{ms}$). It is typically assumed to be lossless (anhysteretic) and with a parabolic dependency on the coil position, leading to a representation using a polynomial function

$$K_{ms}(x) = K_0 + K_1 x + K_2 x^2 + K_3 x^3 + ... + K_N x^N. \tag{1.47}$$

It is quite common, when a sealed enclosure is used, to lump the acoustical air spring $C_{ab}$, into the mechanical compliance.

Even though a substantial amount of work has been performed on the analysis on the nonlinearities of the loudspeaker suspension [2, 3, 42, 48, 60, 74, 78, 93, 95], most of the work is concentrated on the linear frequency dependency due to viscoelastic effects which is usually modelled using fractional derivatives. The main issue here is the memory requirements of fractional derivatives. The loudspeaker suspension has the most effect on the system at low frequencies, below the resonance frequency. This is typically below 100 Hz for the average bass speaker. This means that the FIR filter must have enough samples in memory to correctly model the behaviour for frequencies below 100 Hz, and lower than 1 Hz if creep is to be taken into account. At a sampling frequency of 96 kHz, 1 s of data is

96000 samples, all of which must be summed together in the FIR filter. Furthermore, the real time optimisation of a fractional derivative model adds an extra layer of complexity. As in the case of the electromagnetic domain, while the use of fractional derivatives seems attractive, simpler models are preferred for use in real time processors. It is not only a question of computation power, but also of real time identification or optimisation of the model parameters. The tolerances of the loudspeaker suspension elements are given at ±30% on the value of $C_{ms}$. There is no tolerance on the total stiffness curve, which will also change over time, musical signal and use. Thus the model needs to be simple enough to be updated over time using methods that may be run in real time at sampling frequencies common to music (44.1 kHz, 48 kHz, 96 kHz).

### 1.6.2 Summary

Despite the large number of models available for the drive unit phenomena, not many are actually suitable for real time loudspeaker control due to the necessity of running the model(s) in real time at the required sampling period. The models need to be simple, accurate, and with easy to fit parameters.

In the case of the electromagnetic domain, the $RL_N$ model is the chosen way forward. The coil position dependence can be modelled through the use of independent polynomial functions [23], the reluctance force calculated analytically, and the model breaks down into a system of N differential equations. The voice coil resistance is modelled by a simple resistor that may or may not be temperature dependent, and the coil position dependence of $B\ell$ is modelled through a polynomial function.

In the case of the mechanical domain, a single degree of freedom model is used, with a linear mass and damper. The nonlinear spring is modelled though a simple polynomial function.

This chosen formulation can then be represented as a system of differential equations, of which the solutions may be approximated efficiently by any numerical integration scheme.

## 1.7 Numerical methods

As the models chosen for this thesis are physics based and can be represented as a system of differential equations, there are a variety of efficient ways of approximating the solutions to these equations. The solutions are usually approximated through the numerical integration of the differential equations, where the integration is performed by one of two techniques, 'Linear multi step methods' or 'Runge-Kutta methods' [20]. For this thesis, the linear multi step methods are chosen as the Runge-Kutta methods require knowledge of the function between two sample points, which adds a layer of complexity when dealing with signals such as music.
Linear multi step methods can then again be split into two groups; implicit methods and explicit methods. Contrary to implicit methods, explicit methods only require the past values to compute the next approximation. Therefore explicit methods are used for this thesis. The explicit linear multi step methods are also known as 'Adams-Bashforth' methods.

### 1.7.1 Adams Bashforth Methods

The Adams-Bashforth family of numerical integration methods (solvers) are used to approximate the solution to first order initial value problems. An example of a first order initial value problem would be the first order differential equation describing the current flowing through the electrical circuit shown in Figure 1.26 as

$$u(t) = Ri(t) + L\frac{di}{dt}, \tag{1.48}$$

from which

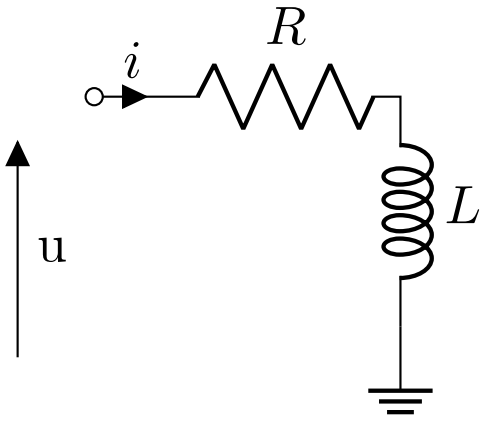


FIGURE 1.26 – RL circuit.

$$\frac{di}{dt} = \frac{u(t) - Ri(t)}{L}. \tag{1.49}$$

This equation is of the form

$$\frac{di}{dt} = y(t, i(t)), \tag{1.50}$$

with initial condition $i(t = 0) = i_0$. From the Euler definition of a continuous time derivative

$$\frac{di}{dt} \approx \frac{i(t + dt) - i(t)}{dt}, \tag{1.51}$$

which can be rearranged

$$i(t + dt) \approx i(t) + dty(t, i(t)), \tag{1.52}$$

and discretised

$$\begin{aligned} i[n + 1] &\approx i[n] + T_s y(n, i_n) \\ y(n, i_n) &= \frac{u[n] - Ri[n]}{L}, \end{aligned} \tag{1.53}$$

where $T_s$ is the sampling period. The expression

$$i[n + 1] \approx i[n] + T_s y(n, i_n) \tag{1.54}$$

is the first order Adams Bashforth solver, or the Euler forwards method. Using the Butcher tables [15] it is possible to extrapolate the higher order solvers. For example $2^{nd}$ and $3^{rd}$ order solvers applied to this example can be written

$$\begin{cases} i[n + 1] &= i[n] + \dfrac{T_s}{2}(3y(n, i_n) - y(n - 1, i_{n-1})) \\ i[n + 1] &= i[n] + \dfrac{T_s}{12}(23y(n, i_n) - 16y(n - 1, i_{n-1}) + 5y(n - 2, i_{n-2})) \end{cases} \tag{1.55}$$

Higher order methods will provide a more accurate approximation of the solution than lower order methods. However the compromise will be on the numerical stability of the solver/equation combination. Appendix C provides a short overview of solver/equation stability.

### 1.7.2 Gradient Descent

The gradient descent method [56] is an optimisation method for differentiable functions. It is a first order method used to find local or global minima of a function by taking steps away from the gradient. When applied to parameter fitting, we often talk of the cost function $C_f$ defined here as

$$C_f = (ref - fit)^2, \tag{1.56}$$

where $ref$ is the reference function, $fit$ is the modelled function being fitted to the reference. The cost function in this case is the squared error. By taking the partial derivative of the cost function relative to the parameter to be optimised $\gamma$ we end up with the gradient and thus the next value of the parameter can be approximated by

$$\gamma_{n+1} = \gamma_n - \eta \frac{\partial C_{f_n}}{\partial \gamma}, \tag{1.57}$$

where $\eta$ is the learning rate. Two factors affecting the convergence of the optimisation method are ; the learning rate and the initial guess $\gamma_0$. Increasing the learning rate may increase the convergence but may also mean the method misses some minima or even diverges, on the other hand too small a step size will mean the solution takes too long to converge. If the initial guess is close to the solution the convergence will be quicker.

## 1.8 Conclusion

As described in Section 1.4 dealing with the first principles, the electrodynamic drive unit is subject to various different nonlinear phenomena, the result of which is a distortion of the sound pressure output. Various ways of compensating the different distortions have been studied and proposed, each with their advantages and disadvantages. The idea behind this thesis is to propose a relatively simple way of compensating some of the distortions, therefore most of the feedback methods where the sensor is an addition to the loudspeaker must be left aside. The idea of using an amplifier with a high output impedance such as a transconductance amplifier is attractive for several reasons :

- simple to make,
- directly control the current and consequently the force,
- no longer need to model nonlinear phenomena such as magnetic hysteresis, eddy currents and thermal effects.

It also greatly simplifies the modelling equations as we only need to calculate the compensation current. The issue with the high output impedance is the lack of damping to the mechanical system, resulting in a higher sensitivity to the mechanical model errors and parameter variations. One part of the solution to this is to use an online gradient descent method to update certain parameters in real time thus reducing the modelling error. Another part of the solution is to add some damping into the system by acoustical means [9].

In terms of model, the chosen way forward is to use relatively simple models such as the Foster network for the electromagnetic inductance, polynomial functions for the coil position dependence, and a simple single degree of freedom mass-spring-damper where the spring stiffness depends on the coil position, and the polynomial function optimised using a gradient descent method. The cost function of the gradient descent will be derived from the measurement of the drive unit voltage and current at its terminals.

The model will be represented as a system of nonlinear differential equations and the solutions approximated using a one or two step linear multistep methods such as the Euler forward or Adams Bashforth second order solver.

The areas that require solutions are as follows :

- noise amplification from numerical derivatives,
- a transconductance amplifier for applying the compensation signal to the loudspeaker system,
- a method for the inversion of quadratic functions for the reluctance force,
- low latency hardware for acquiring and processing signals for the compensation routine,
- adding loss into the system to reduce influence of model errors and component tolerances.

Chapitre 2

# Materials and Methods

## 2.1 Loudspeaker System

In order to provide a complete assessment of the efficiency of the work presented in this thesis, a loudspeaker system is required to both provide parameters and serve as a transducer to linearise. The loudspeaker system was chosen to be a sealed enclosure type as it acts as a relatively linear spring which helps to reduce the influence of the nonlinear mechanical spring of the drive unit. It is also the easiest to construct and does not add extra noise or distortion from vent turbulence. In order to reduce the overall footprint of the system, a 5 inch bass-midrange type drive unit is selected, the Faital Pro 5FE100, and placed inside a sealed enclosure constructed from 18 mm thick Medium Density Fibreboard. The finished loudspeaker is shown in Figure 2.1. The mounting cap and accelerometer can be seen.

## 2.2 System Evaluation

In order to fully evaluate the efficiency of the compensation methods presented in this work, a suitable measurement set up and reference is required. The references are defined as the output of the loudspeaker when stimulated by either a voltage or current source without any compensation. The output of the loudspeaker is defined as the cone acceleration as measured by a miniature accelerometer attached to the former. This section details the various stimuli and measured quantities used for the characterisation of the compensation method.

FIGURE 2.1 – Loudspeaker System.

### 2.2.1 Stimuli

As shown in Section 1.5, the most favoured stimulus for the characterisation of the presented control methods is the sine wave. In the authors opinion they are not at all well suited to the evaluation of a system designed to reproduce such a complex signal as music for the following reasons :

— A low crest factor leads to more voice coil heating than music,
— unable to analyse intermodulation distortion with a single frequency,
— the histograms of sine waves and music are very different.

A sine wave spends more time near high amplitude values whereas music spends more time around zero (Figure 2.2). The distortion generated by a sine wave will thus be mostly due to the peak values whereas the distortion generated by music will be mostly due to low level amplitudes. As such, the stimuli chosen for the analysis of the presented work is a multitone signal.

The multitone signal used in this work is composed of 10 non harmonic logarithmically spaced frequencies each with a uniformly distributed random phase (between zero and $2\pi$), and is windowed in order to avoid beginning and end transients. Figure 2.3 illustrates a multitone signal created with the following characteristics :

— bandwidth : 10 Hz to 1000 Hz,
— 10 logarithmically spaced frequencies,
— duration : 10 s.

When applying a multitone signal to a nonlinear system, the distortion products tend to appear between the fundamentals as a sort of 'grass' as shown in Figure 2.3d. The distortion illustrated is the result of passing the multitone signal through the nonlinear system

$$y = x + 0.01x^2, \tag{2.1}$$

where $x$ is the input and $y$ is the output. The MTND products may then be averaged with a sliding window as in [99] using

$$d_{MTND}(f_i) = \sqrt{\sum_{k=i-K/2}^{K/2} \left( D_k \left[ \cos \frac{\pi |f_i - f_k|}{\Delta f} + 1 \right] \frac{1}{2} \right)^2}, \tag{2.2}$$

where $f_i$ is the centre frequency of the window, $\Delta f$ is the width of the frequency window, $D_k$ is the value of the distortion product at the $k$ frequency bin and $K$ is number of frequency bins in the window. The advantage of this operation is that it transforms the rather unreadable 'grass' into a continuous curve that may be more easily used when comparing two systems. Figure 2.4 shows the result of using different frequency window lengths on the MTND curve.

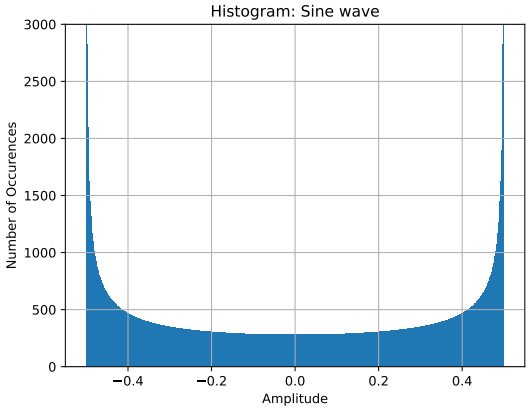


(a) Sine wave. 10 s.

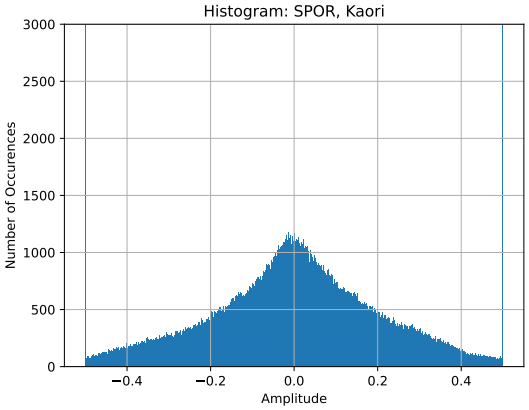


(b) SPOR, Kaori. 10 s (2 minute 55 seconds to 3 minutes 5 seconds).

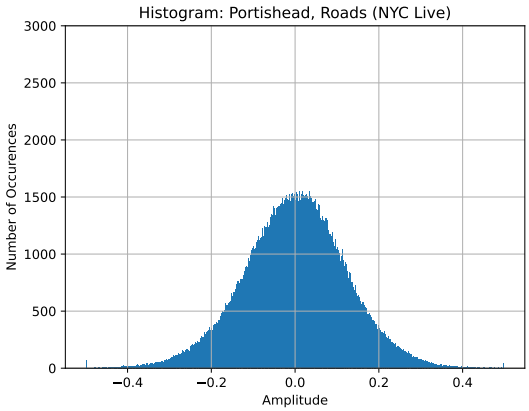


(c) Portishead, Roads (NYC Live). 10 s (2 minute 55 seconds to 3 minutes 5 seconds).

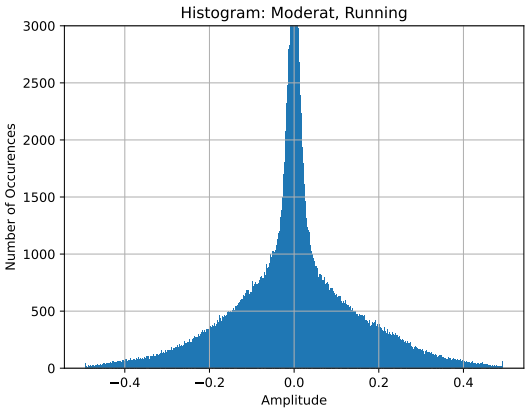


(d) Moderat, Running. 10 s (2 minute 55 seconds to 3 minutes 5 seconds).

FIGURE 2.2 – Signal Histograms. (a) : Sine wave histogram, note the number of occurrences is higher for the peak amplitude levels. (b),(c),(d) : Histograms of different types of music ; note the number of occurrences is higher for amplitude values around zero. Music data extracted directly from .wav files and processed in Python.

### 2.2.2 Measurements

The main quantity used to analyse the compensation is the cone acceleration. Using the sound pressure level brings a variety of additional difficulties such as the need for an anechoic chamber and the nonlinear contributions from the surround and the enclosure.
The acceleration is measured using a small accelerometer (PCB 352C68 or M353B18) screw mounted to a plastic cap that is glued onto the voice coil former as in Figure 2.5a. Secondary quantities of interest are the voice coil voltage, current and displacement. The voice coil current and voltage are measured differentially using Kelvin sense connections and instrumentation Operational Amplifiers (Op Amps), while the displacement is measured using a Keyence LK-H150 laser.

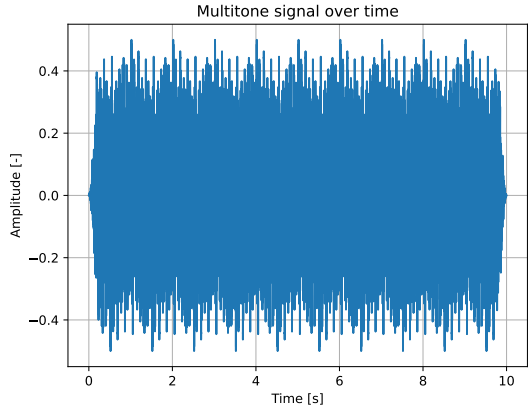


(a) Multitone over time. 10 s.

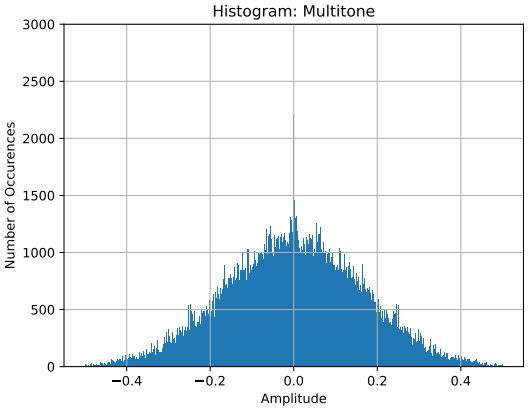


(b) Multitone histogram. 10 s.

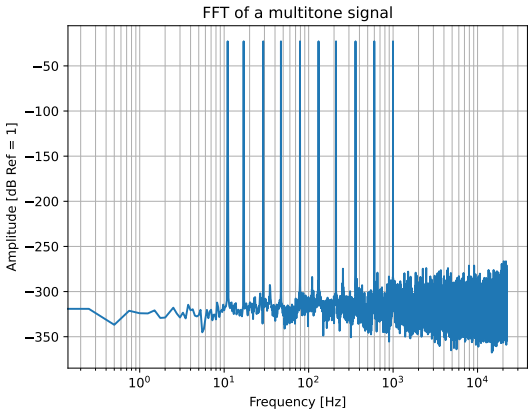


(c) Multitone frequency content.

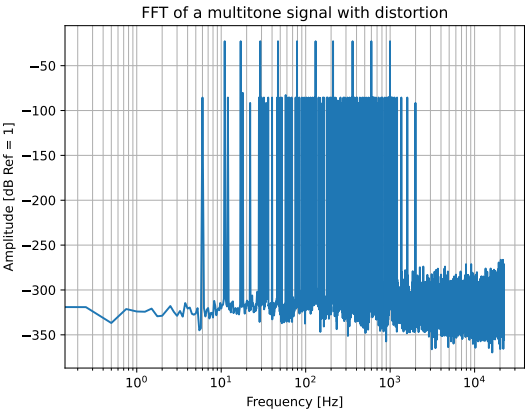


(d) Multitone frequency content, nonlinear system (Eq 2.1).

FIGURE 2.3 – Multitone signal. (a) Multitone over time. (b) : Histogram of the mutlitone signal in (a). (c) : Multitone frequency content of the output of a linear system. (d) : Multitone frequency content of the output of a nonlinear system (Equation 2.1).

## 2.3 System Details

As the goal of this thesis is to provide both a software and hardware foundation for the real time control of a loudspeaker system, work was done on developing software algorithms and several pieces of hardware (boxed in red in Figure 2.6) that combine to produce the real time control system. The system is thus comprised of a controller with two ADCs and one DAC, a transconductance amplifier, a Device Under Test (DUT) comprised of the Faital Pro drive unit in a sealed enclosure. An accelerometer and laser are used to measure the acceleration and displacement of the cone, while a pair of differential Op Amps provide signals proportional to the DUT voltage and current. The controller takes two inputs, the stimulus and the DUT terminal voltage, which are used to generate the correction signal through the hybrid feedback/ feed forward algorithm. The correction signal is then output via the DAC and applied to the DUT via a transconductance amplifier. The DUT cone

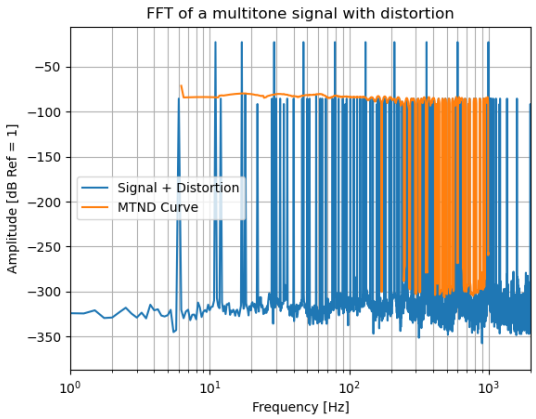


(a) MTND Curve with $\Delta f = 50$ frequency bins.

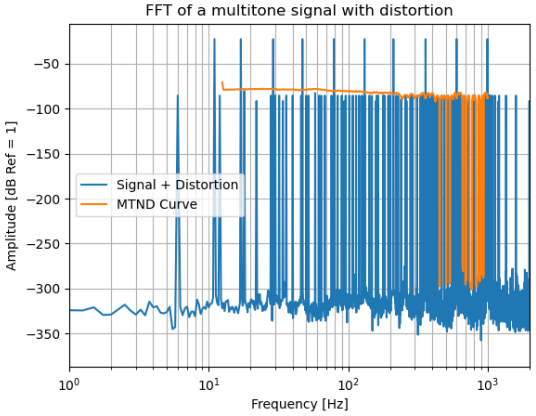


(b) MTND Curve with $\Delta f = 100$ frequency bins.

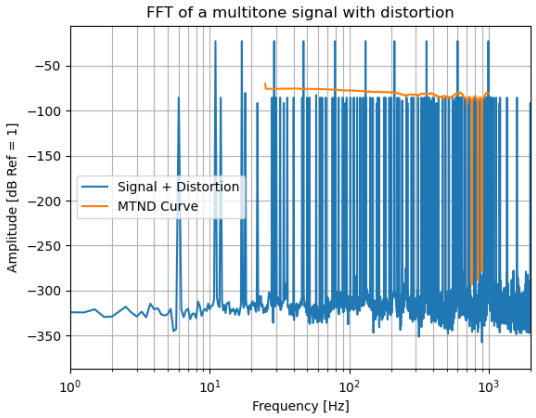


(c) MTND Curve with $\Delta f = 200$ frequency bins.

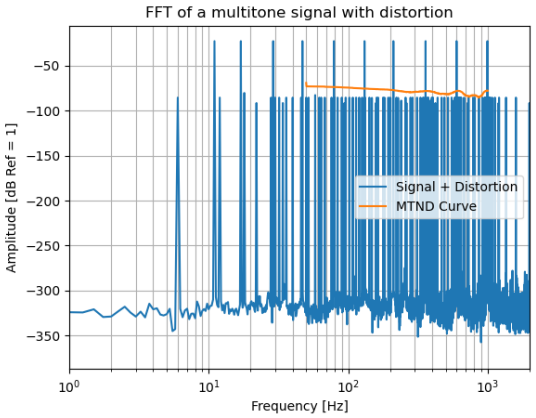


(d) MTND Curve with $\Delta f = 400$ frequency bins.

FIGURE 2.4 – MTND curves. (a) : MTND curve using a window width of 50 points. (b) : MTND curve using a window width of 100 points. (c) : MTND curve using a window width of 200 points. (d) : MTND curve using a window width of 400 points. For (a-d), the orange curve represents the MTND curve as calculated using Equation 2.2.

acceleration and displacement, current and terminal voltage are all acquired using the DT9837C Data Acquisition system (DAQ) and the results post processed in Python on the host Personal Computer (PC).

The next sections detail the software algorithms and provide the electrical characteristics of the real time controller. Appendix D details the power amplifier module, while Appendix E discusses some of the design factors for the Voltage/Current sensing equipment that was designed.

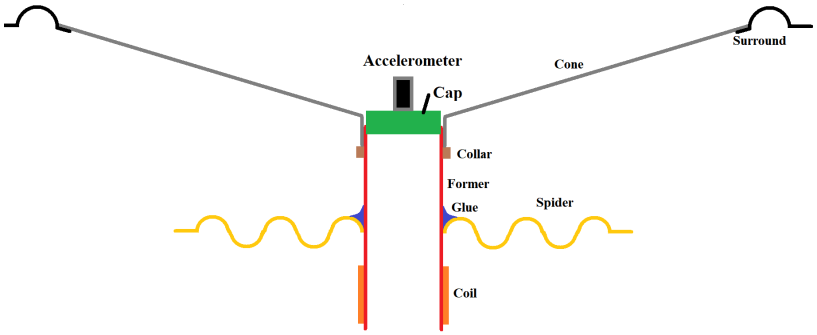


(a) Accelerometer mounting concept.

(b) Faital Pro 5FE100 with accelerometer.

FIGURE 2.5 – Accelerometer Mounting. (a) : Simplified drawing showing the accelerometer mounting concept with the mechanical parts. (b) : Photo of the actual drive unit with accelerometer mounted.

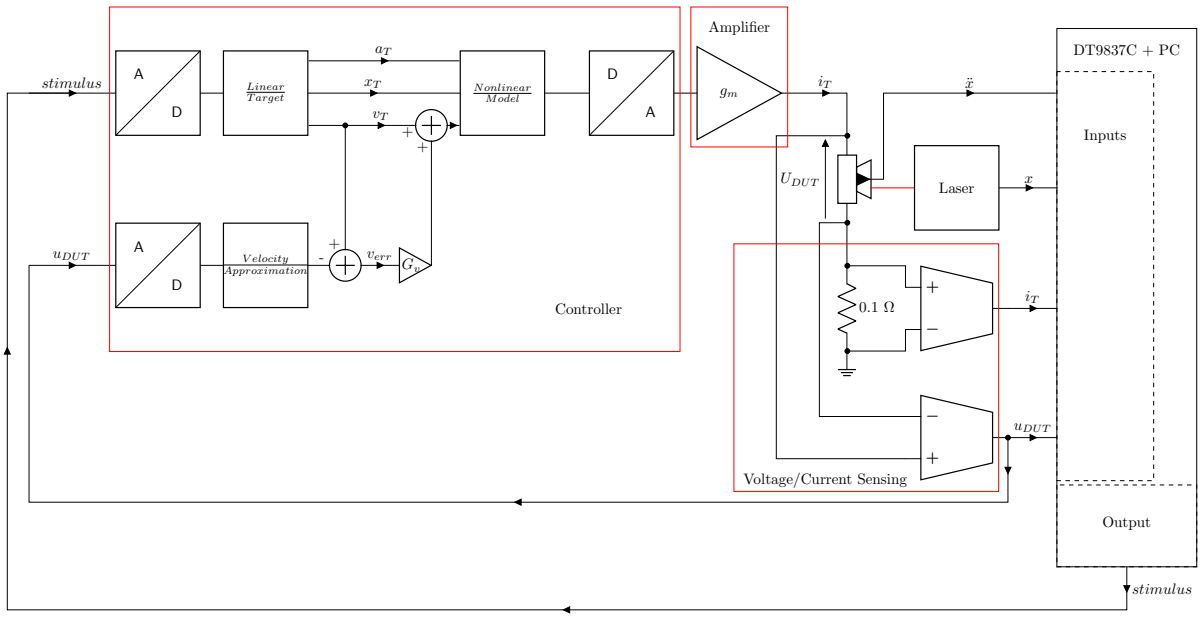


FIGURE 2.6 – System setup.

## 2.4 Feed forward model

If feed forward is to be used, then a nonlinear model is required. As specified in the conclusion of the state of the art, the model is kept relatively simple. To this end, a $R_N L_N$ model [23] is used for the electromagnetic inductance, a simple single degree of freedom mass-spring-damper where the spring stiffness depends on the coil position, and polynomial functions for the coil position dependence. The model is represented as a system of nonlinear differential equations and the solutions approximated using the Adams-Bashforth second order solver.

This section also details the following problems and the proposed solutions :

— a method for the inversion of quadratic functions for the reluctance force,

— a method to deal with stiffness tolerances and variations over time,

— an explanation of the derivation of the model parameters,

— a method to remove the noise amplification from numerical derivatives.

### 2.4.1 Model

The basic structure of the nonlinear model is shown in Figure 2.7. Each nonlinear parameter is represented by a unique polynomial function, and only the $K_{ms}(x)$ polynomial function is optimised in real time using a gradient descent method. The way the feed

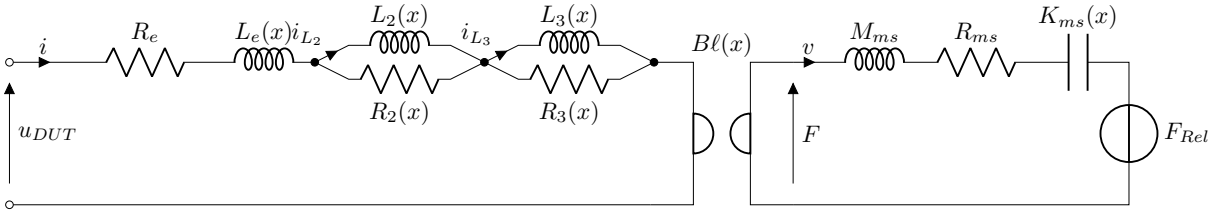


FIGURE 2.7 – Nonlinear Models Structure.

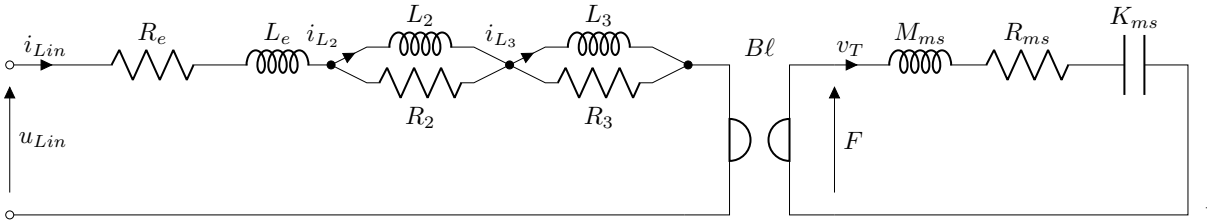


FIGURE 2.8 – Linear Target Model.

forward algorithm functions is as follows. The stimulus is applied to the linear target model (Figure 2.8) as the voltage $u_{Lin}(t)$. The linear model is represented as a system of linear Ordinary Differential Equations (ODEs), which provide approximations for the target coil displacement $x_T(t)$, velocity $v_T(t)$ and acceleration $a_T(t)$. These three variables

are then used to calculate the force $F_T(t)$ to apply to our nonlinear system using

$$F_T(t) = M_{ms}a_T(t) + R_{ms}v_T(t) + K_{ms}(x_T)x_T(t). \tag{2.3}$$

We now need to transform this target force into a target current $i_T$. If there was no reluctance force, the expression for the target current would simply be

$$i_T = \frac{F_T}{B\ell(x_T)}. \tag{2.4}$$

### 2.4.2 Problems and Solutions

#### Reluctance Force

Unfortunately the reluctance force complicates matters. The reluctance force is a purely nonlinear addition to the Lorentz force and a quadratic function of the current. A feed forward compensation method was proposed in [54] where the linearising current $i_T(t)$ was found by approximating the roots of the equation, quadratic in $i_T(t)$, shown below

$$\frac{1}{2}\frac{dL_e}{dx}i_T(t)^2 + B\ell i_T(t) = F_T(t), \tag{2.5}$$

this however becomes less accurate when using Foster type networks to model the electrical impedance. The author proposed a method for the approximation of the target current $i_T$ that does not require root finding or model inversion, which was tested and then published in [72]. The methodology will be briefly summarised here.

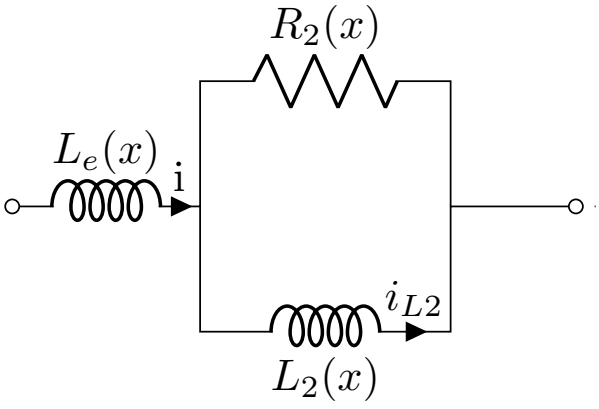


FIGURE 2.9 – $R_2L_2$ electrical impedance model.

If we refer to the $R_2L_2$ model as illustrated in Figure 2.9, then the reluctance force may be calculated as either [84]

$$\frac{1}{2}\frac{dL_e}{dx}i(t)^2 + \frac{1}{2}\frac{dL_2}{dx}i(t)i_{L2}(t) + B\ell i(t) = F(t), \tag{2.6}$$

or [72]

$$\frac{1}{2}\frac{dL_e i(t)^2}{dx} + \frac{1}{2}\frac{dL_2 i(t) i_{L2}(t)}{dx} + B\ell i(t) = F(t), \tag{2.7}$$

or [47]

$$\frac{1}{2}\frac{dL_e}{dx} i(t)^2 + \frac{1}{2}\frac{dL_2}{dx} i_{L2}^2(t) + B\ell i(t) = F(t). \tag{2.8}$$

All three of these equations work, however it was found that when a shorting ring was present inside the loudspeaker motor system [72], the formulation (2.7) was the most accurate.

In all three cases the current $i_{L2}$ depends on the current $i$ through the nonlinear differential equation

$$\frac{dL_2(x) i_{L2}(t)}{dt} = R_2(x)(i(t) - i_{L2}(t)). \tag{2.9}$$

Rewriting Equations (2.6) and (2.9) in the discrete domain under the assumption that the coil is blocked and therefore $\frac{dL_e}{dx}$, $\frac{dL_2}{dx}$ and $B\ell$ are constants,

$$\begin{cases} \frac{1}{2}\frac{\partial L_e}{\partial x} = A, \\ \frac{1}{2}\frac{\partial L_2}{\partial x} = B, \\ B\ell = C, \end{cases} \tag{2.10}$$

leads to

$$Ai^2[n] + Bi[n] i_{L2}[n] + Ci[n] = F[n], \tag{2.11}$$

and

$$\begin{cases} di_{L2}[n] = K[n](i[n] - i_{L2}[n]), \\ K[n] = \frac{R_2(x[n])}{L_2(x[n])}. \end{cases} \tag{2.12}$$

We can see that Equation (2.11) is an implicit equation as $i[n]$ is needed to calculate $i_{L2}[n]$ via the ODE given in Equation (2.12), but $i_{L2}[n]$ is needed to calculate $i[n]$. This is one of the reasons why the root finding methods do not work. The solution presented in [72] is to use the solution of $i$ and $i_{L2}$ at the previous time step to turn the implicit Equation (2.11) into the explicit equation,

$$Ai^2[n-1] + Bi[n-1] i_{L2}[n-1] + Ci[n] = F[n], \tag{2.13}$$

which leads to an approximation of the current $i[n]$,

$$i[n] = \frac{F[n] - Ai^2[n-1] - Bi[n-1]i_{L2}[n-1]}{C}. \tag{2.14}$$

As the reluctance force is a linear combination of $i$ and $i_{L2}$, we may write

$$i[n] = \frac{F[n] - F_{rel}[n-1]}{B\ell}, \tag{2.15}$$

which is also represented in Figure 2.10, where the black box represents the reluctance force formulation with all the required mathematical operations.

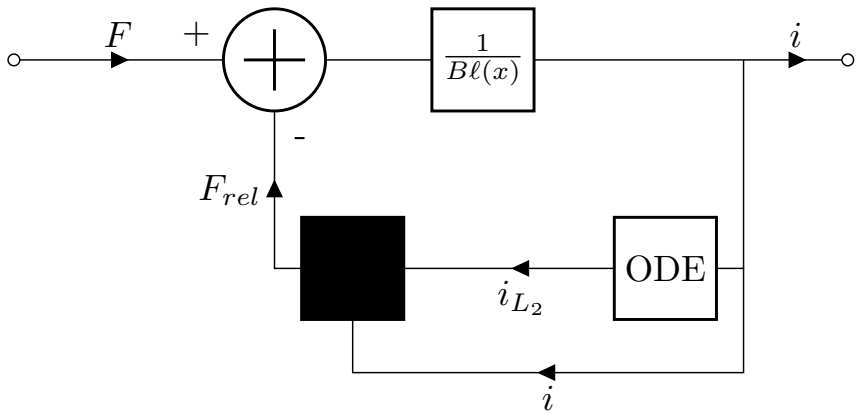


FIGURE 2.10 – Algorithm illustration.

Thus the target current $i_T$ at a time step $[n]$ can be calculated using,

$$i_T[n] = \frac{F_T[n] - F_{rel}[n-1]}{B\ell(x_T[n])}. \tag{2.16}$$

Of course, it should be noted here that in the case of real time compensation on a loudspeaker, all of the gradients of the inductance's vary with the coil position and thus with time. This means that in the case of the $RL_2$ model, the constants $A$ and $B$ in equation (2.10) are recalculated at each time step.

### Model Parameters

The model requires a set of linear and nonlinear parameters for the feed forward compensation to work, where the accuracy of these parameters directly effects the compensation efficiency. There are a variety of different ways of obtaining the model parameters, however in the aim of keeping the compensation algorithm as simple as possible, most of the model parameters are fixed with only the suspension stiffness $K_{ms}$ being updated in real time.

The electromagnetic parameters are obtained using a hybrid method. The blocked coil jig

(detailed in Section 2.5) is used to improve a series of Finite Element simulation results by providing clean measurements of the electrical impedance and force factor $B\ell$ for coil positions between -8 mm (in the motor) and 8 mm (outside the motor) with a 2 mm step. These measurements are performed by stimulating the coil with an exponential chirp signal using a voltage source, and measuring the voltage, current and force. The simulation is then used to provide electrical impedance and force factor data for a larger number of coil positions, (between -8 mm and 8 mm in steps of 0.5 mm) and 10 frequency points, as a sort of physics based interpolation. Three major advantages of using a simulation to provide the data compared with performing the measurements are :

— it is possible to use a finer spatial resolution in the simulation,
— there is no noise, ground loops or temperature effects,
— there is no need to perform the measurements, simulations can be run overnight (if required).

A comparison between the measured quantities and those from simulation can be seen in Figure 2.11. The simulated $B\ell$ provides a very good match to the measurements for all positions apart from at + 8 mm. The source of this discrepancy could not be explained, however this error is not deemed an issue as the voice coil should never be this far out of the gap. For the apparent inductance $L_{app}$, the simulation and measurements are very well matched over the 20 Hz to 1000 Hz bandwidth for each coil position. There seems to be an increase in the error for frequencies below 15 Hz as the coil moves further into the motor. This suggest there is a source of error that depends on the model used for the steel, as for these frequencies the eddy currents and magnetic field created by the coil will propagate through the entire motor structure as shown in Appendix A. Overall, it is clear that the simulated data provides a very good match to the measured data, while also allowing a finer spatial resolution.

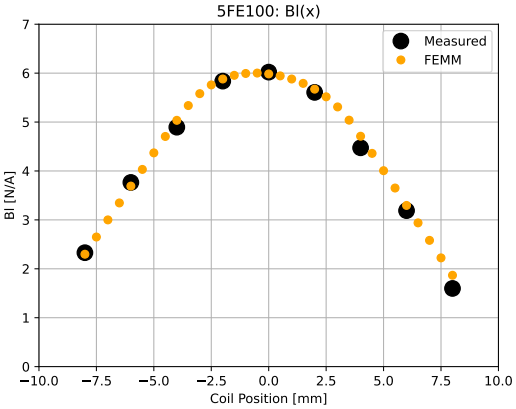


(a) $B\ell(x)$. Measured vs FEMM.

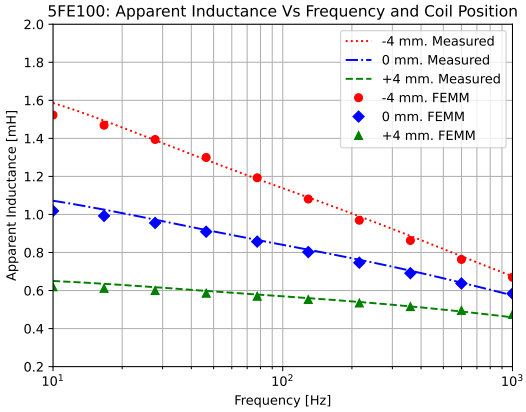


(b) $L_{app}$ (Equation 2.17). Measured vs FEMM.

FIGURE 2.11 – Measurements versus FEMM Simulation. (a) : $B\ell(x)$. Large black dots, Measured $B\ell$. Small orange dots, simulated $B\ell$ (b) : Apparent inductance versus coil position and signal frequency. The red colour indicates results for when the coil is 4 mm inside the motor with the dotted line indicating the measurement and the points indicating the simulation. The blue colour indicates results for when the coil is at the rest position (0 mm) with the dot dash showing the measurement and the diamonds showing the simulation. The green colour indicates results for when the coil is 4 mm outside of the motor with the dashes representing the measurement and the triangles representing the simulation.

A simple least square algorithm is used to fit the $R_3L_3$ model to the impedance data. The cost function for the least squares algorithm is derived from the apparent inductance $L_{app}$, defined as

$$L_{app} = \frac{\Im(Z)}{\omega}, \tag{2.17}$$

with $\omega$ the angular frequency and $Z$ the electrical impedance. The apparent inductance is chosen to generate the cost function as the nonlinear model uses the inductance as a parameter, not the impedance which is a frequency domain quantity. In order to increase the frequency resolution of the data, the 10 frequency points are interpolated using a cubic function, and the data is then extended to 1000 frequency points. Once the $R_3L_3$ model is fitted to the data at each coil position, separate polynomial functions are used to approximate the spatial variations of each parameter. For the Faital Pro 5FE100, the chosen polynomial order is 3, as justified in [72]. $B\ell$ is represented by a $6^{\text{th}}$ order polynomial function. The resulting fit can be seen in Figure 2.12. The polynomial fit of $B\ell$ provides a very good fit to the FEMM data, without diverging too much inside the -10 mm to 10 mm input range. The impedance data shown in Figure 2.12b shows an excellent agreement between the fitted and FEMM data between 10 Hz and 1 kHz. The spatial gradient of the apparent inductance shown in Figure 2.12c shows some error for coil positions around -2 mm and above 6 mm. This error is surely due to the order of the polynomial function used to fit the inductance model parameters. Increasing the order from 3 to 4, 5 or 6 should

provide a better fit of the spatial gradient at the expense of requiring more calculations. Finally, Figure 2.12d shows how the parameters vary with coil position. All of the parameters are highest for coil positions inside the motor structure and then decrease as the coil moves out of the motor. This sort of behaviour is expected as the coils inductance increases when the coil is surrounded by the steel of the motor structure, and decreases when it is surround by air.

Finally, it should be noted that when the order of the polynomial functions increases, so does the numerical range of the coefficients. For example, for the fit of the $B\ell(x)$ parameter with $x$ in meters, the numerical range between the first coefficient $B\ell_0 = 6.03359$ and the last coefficient $B\ell_5 = 4.64246e^{12}$ is approximately $1e^{12}$, which may induce rounding errors into the calculation. The proposed way to avoid this issue is to fit the $B\ell(x)$ parameter to a polynomial function that takes a input $x$ scaled to another unit, such as decimeters. In this case, the first and last coefficients of $B\ell(x)$ are $B\ell_0 = 6.03359$ and $B\ell_5 = 4.64246e^{6}$. The range has been reduced by a factor of $1e^{6}$ and all that is required in the algorithm is to convert the displacement used to evaluate the polynomial function from meters to decimeters, simply by multiplying by a factor of 10. It is possible to choose a different unit, but care must be taken to balance all the polynomial functions to avoid creating large ranges where there were none before.

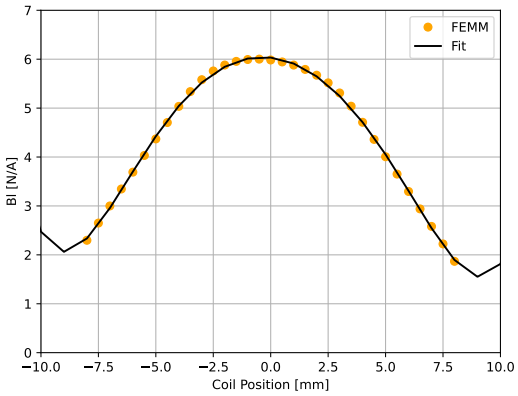


(a) $B\ell(x)$. Fit Vs Data.

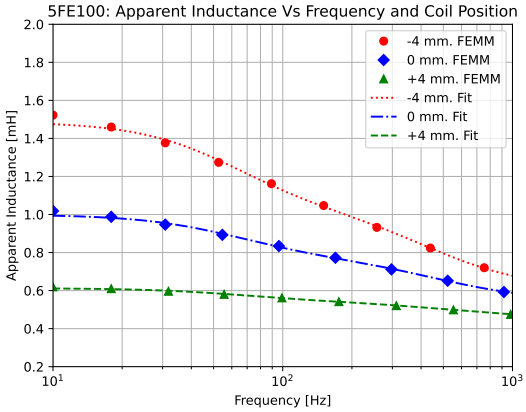


(b) Apparent inductance parameter fit.

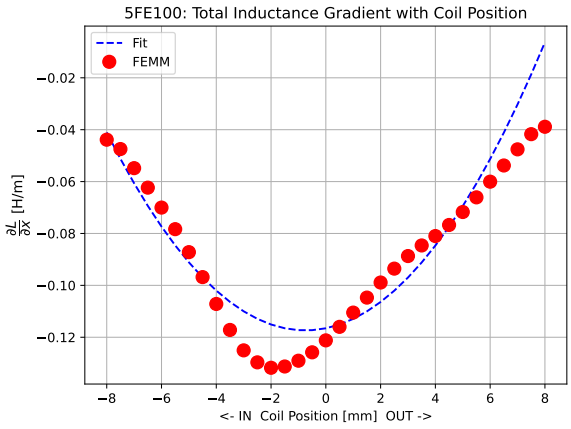


(c) Apparent inductance spatial gradient.

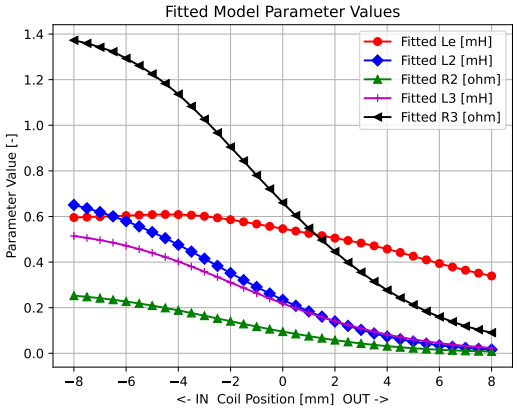


(d) $R_3L_3$ parameter values.

FIGURE 2.12 – Fitted parameters versus data. (a) : $B\ell(x)$. The orange points represent the reference data provided by the simulation while the black line indicates the fit. (b) : Apparent inductance fit versus FEMM data. Red indicates results when the coil is 4 mm inside the motor, with the points representing the reference data and the dotted line showing the fit. Blue indicates results for the coil at the rest position (0 mm), with the diamonds showing the reference data and the dash dot showing the fit. Green indicates the results when the coil is 4 mm outside the motor, with the triangles representing the reference data and the dashes the fit. (c) : Spatial gradient of apparent inductance, fit versus FEMM data. The blue dashed line shows the modelled spatial gradient of inductance while the red points show the measured spatial gradient of inductance. (d) : $R_3L_3$ model parameters. The black arrows designate the $R_3$ parameter, the red points the $L_e$ parameter, the blue diamonds the $L_2$ parameter, the purple plus signs show the $L_3$ parameter and the green triangles represent the $R_2$ parameter.

The mechanical system parameters are obtained by simply reading the values of $M_{ms}$, $K_{ms}$ and $R_{ms}$ from the data sheet, and calculating the equivalent air spring of the enclosure volume. The data sheet for the Faital Pro 5FE100 (4 Ω version) specifies the following parameter values :

— $M_{ms} = 9.8$ g,
— $R_{ms} = 0.5$ Kg.s$^{-1}$,
— $C_{ms} = 0.61$ mm.N$^{-1}$.

Which gives a mechanical stiffness of 1636 N/m. For the nonlinearity of the mechanical stiffness, it is assumed that when the coil position is at $x_{max}$, the suspension stiffness has increased by 50%, and that the stiffness curve is parabolic. The polynomial function that represents the stiffness variation with coil position $K_{ms}(x)$ is therefore represented using

$$K_{ms}(x) = 1636 + 32.72e^6x^2. \tag{2.18}$$

Using the dimensions of the enclosure, the equivalent mechanical stiffness of the air spring is calculated with

$$K_{ab} = \frac{\rho c^2 S_d^2}{V_{box}}, \tag{2.19}$$

with $K_{ab}$ the equivalent mechanical stiffness, $\rho$ and $c$ the air density and celerity of sound under ambient conditions, and $V_{box}$ the volume of the enclosure. The enclosure stiffness is estimated at 1166 N/m. The total mechanical stiffness is illustrated in Figure 2.13. Taking

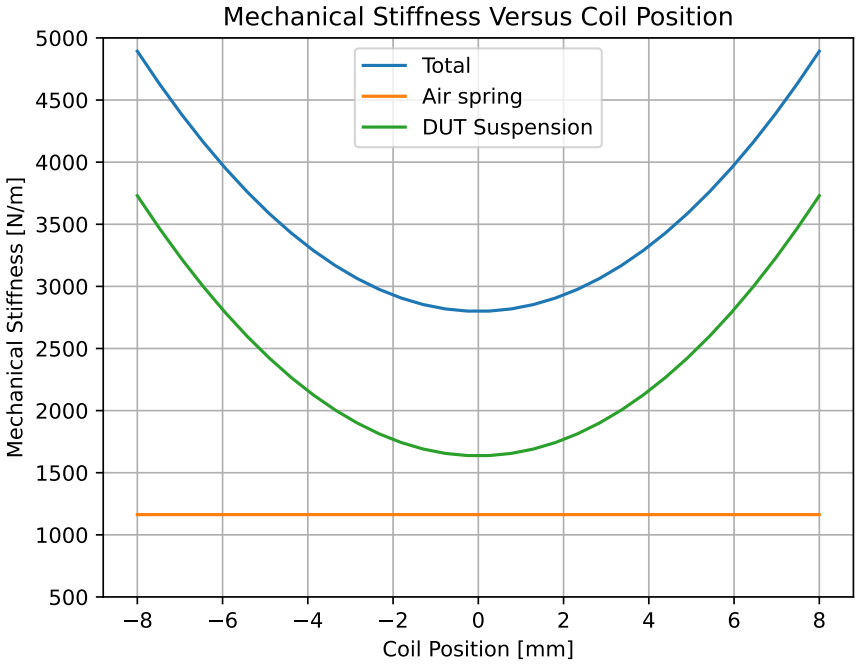


FIGURE 2.13 – Nonlinear stiffness model.

into account the added mass of the accelerometer, cap and wire the final mechanical

parameters are :

— $M_{ms} = 19$ g,

— $R_{ms} = 0.5$ Kg.s$^{-1}$,

— $K_{ms}(x) = 2802 + 32.72e^6x^2$ N.m$^{-1}$,

where the values for the $K_{ms}$ polynomial function are the initial guess for the optimisation scheme detailed next.

### Stiffness tolerances and time variations

If we refer back to Equation (2.3), we can see that the target force depends on the mechanical mass $M_{ms}$, loss $R_{ms}$ and stiffness $K_{ms}$. The mechanical stiffness is the parameter that varies the most both sample to sample and over time. The high output impedance of the amplifier means that the system is more sensitive to component tolerances and variations [7], leading to the requirement that the model parameters be fitted to the actual loudspeaker sample as in [79]. This can be done using a gradient descent method, which requires information about the behaviour of the actual drive unit, specifically the coil displacement $x$, velocity $v$ or acceleration $a$, to generate the error used by the cost function $C_f$.

The gradient descent method consists of taking the current guess of a parameter $\gamma$ and subtracting the gradient of the cost function relative to the parameter as in

$$\gamma_{n+1} = \gamma_n - \eta \frac{\partial C_{f_n}}{\partial \gamma}, \tag{2.20}$$

where $\eta$ is the learning rate.

By measuring the loudspeaker terminal voltage $u_{DUT}$, it is possible to approximate the loudspeaker coil velocity $v_{DUT}$ (in the case of the $R_2L_2$ model) using

$$v_{DUT}[n] \approx \frac{u_{DUT}[n] - R_e i[n] - L_e(x)\dot{i}[n] + R_2(x)(i[n] - i_{L2}[n])}{B\ell(x)}, \tag{2.21}$$

where $\dot{i}[n]$ aims at approximating the time derivative of the coil current $i[n]$. Either the target current value $i_T[n]$ from the algorithm or the measured current $i_m[n]$ may be used. The absolute error between the target velocity $v_T$ and the coil velocity can then be defined as

$$v_{err} = v_T - v_{DUT}, \tag{2.22}$$

which can then be used for the cost function of the gradient descent method. This error may also be used as a feedback variable, which brings us to the technique used in this work. The velocity error $v_{err}$ is used to provide a small amount of error correction while also generating the error required for the gradient descent. The expression for the target

force is changed from Equation (2.3) to

$$F_T[n] = M_{ms}a_T[n] + R_{ms}(v_T[n] + G_v v_{err}[n]) + K_{ms}(x_T[n])x_T[n], \tag{2.23}$$

where $G_v$ is the gain factor applied to the velocity error feedback. If $K_{ms}(x)$ is assumed to be parabolic with an offset, then it may be represented by a second order polynomial function

$$K_{ms}(x) = K_0 + K_2 x^2, \tag{2.24}$$

where both $K_0$ and $K_2$ are parameters to be optimised given an initial guess.
A common cost function for gradient descent methods is the square summed error, however as the algorithm will be running in real time and not on a finite set of data, the instantaneous squared error is used as in stochastic gradient descent [73]. By rearranging Equation (2.23) we find

$$v_{err}[n] = \frac{F_T[n] - M_{ms}a_T[n] - R_{ms}v_T[n] - K_{ms}(x_T[n])x_T[n]}{R_{ms}G_v}, \tag{2.25}$$

thus the cost function is

$$C_f = \frac{1}{(R_{ms}G_v)^2}\left(F_T[n] - M_{ms}a_T[n] - R_{ms}v_T[n] - K_{ms}(x_T[n])x_T[n]\right)^2. \tag{2.26}$$

Both the gradient of the cost function relative to $K_0$ and $K_2$ can then be analytically calculated resulting in

$$\frac{\partial C_f}{\partial K_0} = \frac{-2x_T D}{(R_{ms}G_v)^2}, \tag{2.27}$$

and

$$\frac{\partial C_f}{\partial K_2} = \frac{-2x_T^3 D}{(R_{ms}G_v)^2}, \tag{2.28}$$

with

$$D = F_t - M_{ms}a_T - R_{ms}v_T - K_{ms}(x_T)x_T. \tag{2.29}$$

Therefore, the parameter values can be updated in real time using

$$K_0[n+1] = K_0[n] - \eta\frac{-2x_T D}{(R_{ms}G_v)^2}, \tag{2.30}$$

and

$$K_2[n+1] = K_2[n] - \eta\frac{-2x_T^3 D}{(R_{ms}G_v)^2}. \tag{2.31}$$

### Noise from numerical differentiation

The problem of noisy numerical differentiation most commonly appears when the correction stimulus is applied to the loudspeaker system using a voltage amplifier. Once the target current $i_T$ is calculated, the corresponding target voltage $u_T$ must be approximated using a differential equation, for example in the case of the $R_2L_2$ model

$$u_T[n] = R_e i_T[n] + L_e(x_T)\dot{i}_T[n] + R_2(x_T)(i[n] - i_{L2}[n]) + B\ell(x_T)v_T[n], \tag{2.32}$$

where $\dot{i}_T[n]$ is the numerical derivative of the target current $i_T$ at the sample number $n$. The most obvious solution to this problem is the use of an amplifier with a high output impedance, which means the output of Equation (2.16) can be directly applied to the loudspeaker. This solution also removes all modelling errors due to eddy currents, electromagnetic hysteresis and reduces the errors due to thermal effects.
Unfortunately the use of an amplifier with a high output impedance does not remove the problem, it simply moves it to another area where it is slightly less of an issue. The use of velocity error correction as announced in the previous section requires the numerical derivative of the current to approximate the coil velocity as in Equation (2.21). Any noise from the numerical derivative is thus fed back into the system through the feedback gain $G_v$. The proposed solution to this issue is to simply use the time derivative of the current from the linear model. Observing the system of ODEs that describes the target model behaviour, we see that the $\frac{di_{Lin}}{dt}$ term is the result of

$$\frac{di_{Lin}}{dt} = \frac{stimulus - R_e i_{Lin} - R_2(i_{Lin} - i_{L2}) - R_3(i_{Lin} - i_{L3}) - B\ell v_T}{L_e}. \tag{2.33}$$

The numerical methods used to approximate the solutions to differential equations are integrators, thus the current $i_{Lin}$ is the result of an operation that reduces high frequency noise. $i_{L2}$, $i_{L3}$ and $v_T$ are all filtered versions of $i_{Lin}$, therefore the only source of potential noise in this equation is the stimulus due to the passage through cables, signal conditioning and analog to digital conversions. The downside is that as we use the derivative of the current from the linear model, there is a small error due to the lack of distortion and its time derivative ; however it is possible to use low pass filters to reduce the error.

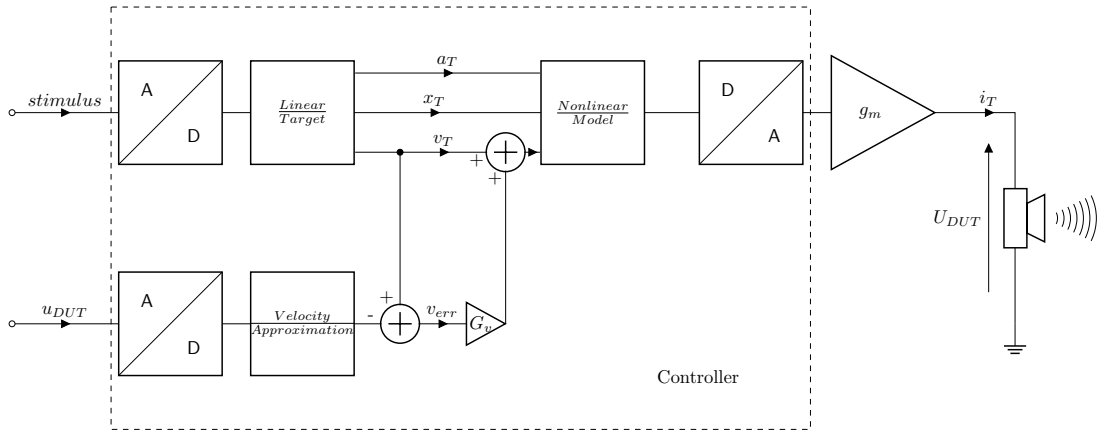


FIGURE 2.14 – Algorithm Structure, overview.

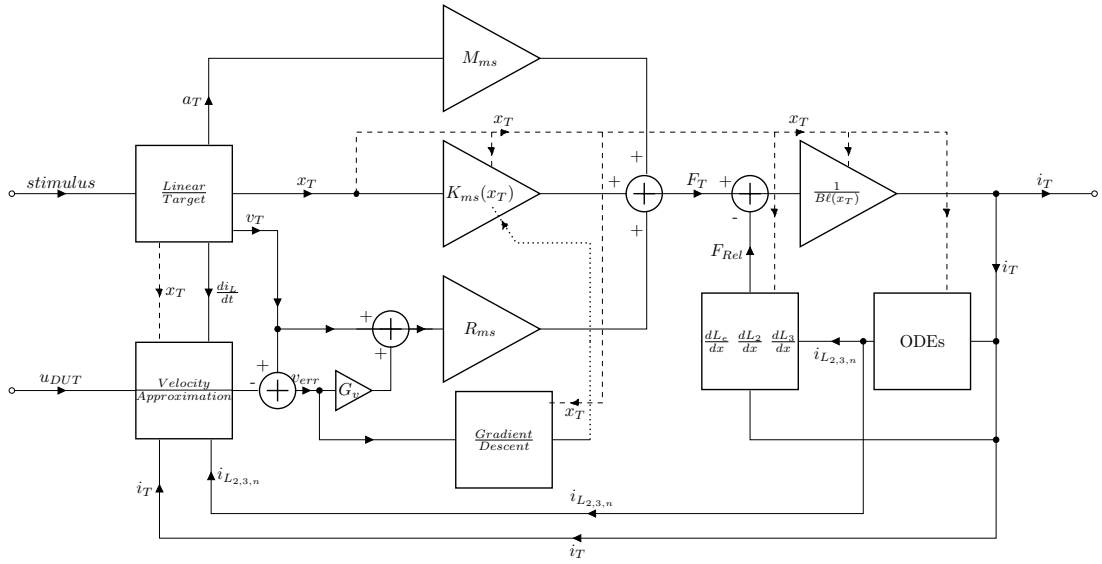


FIGURE 2.15 – Algorithm Structure, details. Dashed lines indicate the variable is used for the nonlinear functions. Dotted lines indicate the quantity is used to update the model.

### 2.4.3 Conclusion

In summary, the algorithm is a hybrid feed forward type model that uses feedback to improve the nonlinear model accuracy while also implementing a simple form of error correction as illustrated in Figures 2.14 and 2.15. The algorithm does not require root finding or model inversions to compensate for the quadratic nature of the reluctance force. In order to reduce model errors, a velocity error correction term is coupled with a simple gradient descent algorithm. Finally, a compromise is proposed to reduce the amount of noise introduced into the system by numerical derivatives.

## 2.5 Blocked Impedance Jig

The model presented in the previous section requires parameters to function and the closer the parameters are to reality, the more efficient the compensation. To this end, a specialised jig was designed and constructed whose concept is shown in Figure 2.16a. This jig was designed to allow the simultaneous measurement of the coil current, voltage and the force while the coil was blocked axially at a certain position inside the motor. The materials used were also studied to reduce the amount of electromagnetic coupling with the coil while also keeping the first modal frequency above 1 kHz. The end result (Figure 2.16b) is that clean measurements may be performed up to 1 kHz for a variety of different coil positions.

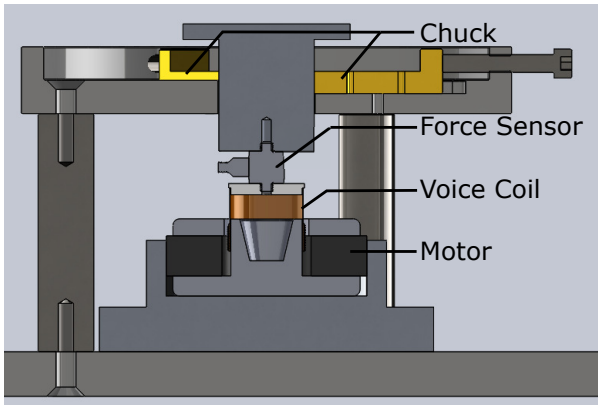


(a) Jig Concept.

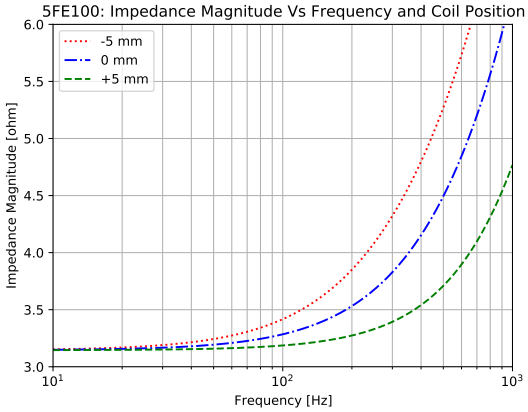


(b) Electrical impedance measurement performed using the jig.

FIGURE 2.16 – Jig Concept & Measurement. (a) : CAD concept of the Jig. (b) : Example of blocked coil measurements performed using the jig. Red dotted line indicates results for the voice coil 5 mm inside the motor, blue dash-dotted line indicates results for the coil at the rest position (0 mm), and green dashed line shows results for the voice coil 5 mm outside the motor.

### 2.5.1 Principle

The main principle of the jig is to be able to move the voice coil axially inside the motor, then block the coil at a certain position. The voice coil could then be stimulated, and by measuring the voltage and current the electrical impedance deduced. A very useful addition was the mounting of a force sensor. This allowed the simultaneous measurement of electrical impedance and the relationship between electrical current and force.
In order to fine tune the radial position of the coil inside the magnetic gap, three chucks are used to block the coil at the predefined position, and three screws used to block the motor. Adjusting each screw leads to a fine tuning of the radial position of both the motor

and coil.
For our work presented in [72], it was conducive to be able to perform the electrical and mechanical measurements up to 1 kHz without any mechanical modes interfering with the results, to that end both the jig materials and geometry were considered.

### 2.5.2 Materials

The choice of materials for the jig was an interesting challenge. The requirements were as follows :

- first mode above 1 kHz,
- low electromagnetic coupling to the coil,
- low magnetic coupling to the motor,
- could be produced at the University.

No mechanical simulations were performed to guide the geometry and materials choice, instead materials were selected based on their Young's modulus, electrical conductivity, and relative permeability. The goal was to use materials that had a high Young's modulus, low electrical conductivity, low relative permeability and could be acquired and machined at the University. The end result is that the structure is mainly composed of a mixture of AISI 316 Stainless steel (Austenitic) and Aluminium as shown in Figure 2.17. Although there are various ceramics on the market that would have resulted in a much lower electrical conductivity compared to the steel, they are expensive, very difficult to machine and the resulting parts are extremely fragile. This comes from previous experience with using ceramics for similar jigs. Some simple Finite Element Analysis (FEA) simulations were performed to verify the electromagnetic and magnetic coupling. A simplified geometry was created in the FEMM software [65] and the magnetic flux lines and induced currents were observed inside the structure. Figure 2.18 shows the static magnetic field lines as well as the induced currents at three different frequencies. The steel part of the structure has no influence on the magneto static solution and there are no induced currents. On the other hand, the two aluminium parts show induced currents, especially as the frequency of the coil current increases. Changing the material of the motor cup from aluminium to AISI 316 stainless steel would reduce the amount of induced currents and may be a worthwhile improvement for the next version.

### 2.5.3 Geometry

Compared to the materials choice, little work was performed on the geometry of the jig. The main factors affecting the geometry were the size of the drive unit motor, and the maximum measurement range for the coil position. The motor size directly affected the diameter of the structure, while the axial measurement range affected the height. The

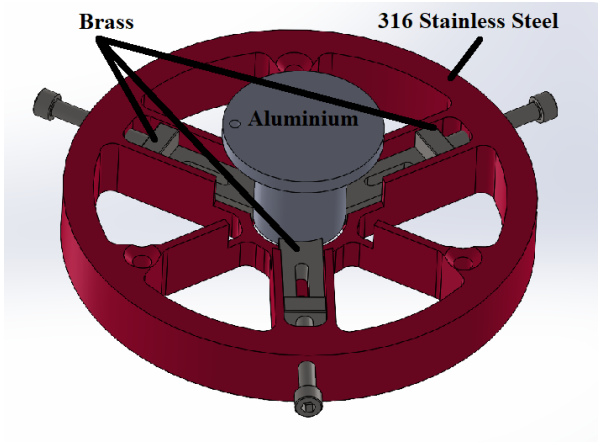


(a) Hub & chucks.

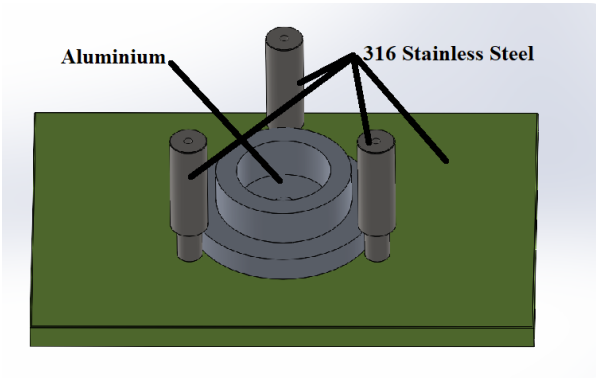


(b) Base.

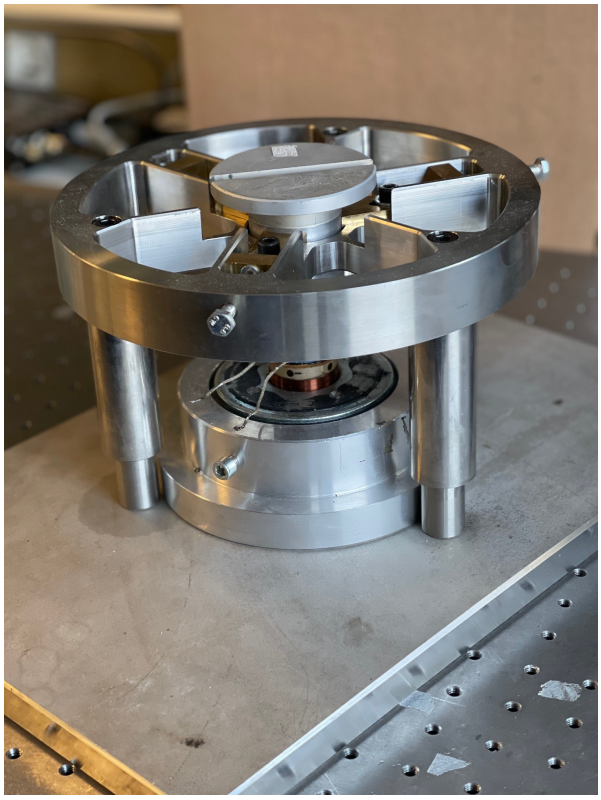

(c) Assembly.

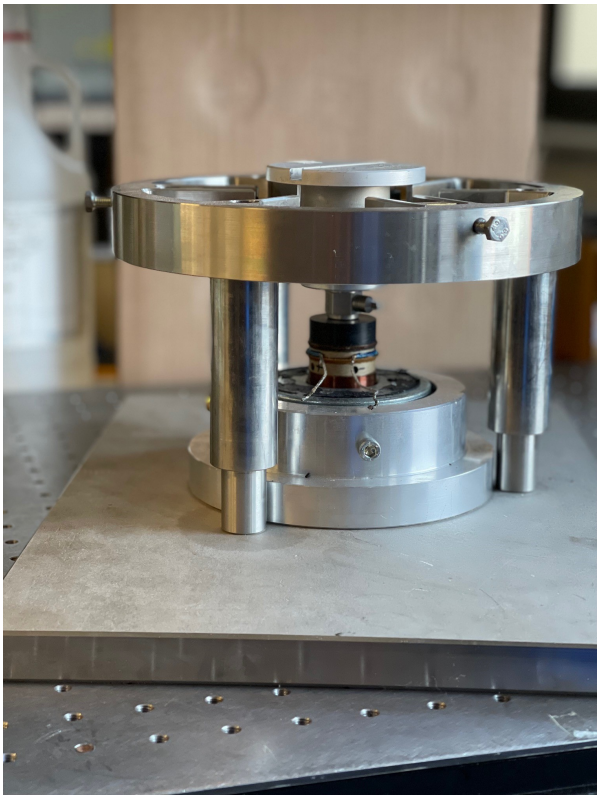

(d) View with Force Sensor.

FIGURE 2.17 – Jig Composition. (a) : 3D Computer Aided Design (CAD) model of the hub, chucks and coil holder. (b) : 3D CAD model of the base, motor cup and hub supports. (c) : Finished Jig with motor and coil. (d) : Finished Jig with motor and coil, showing the force sensor.

main 'hub' was designed to seat the chucks while also providing as much stiffness in the axial direction as possible, leading to a wheel spokes type geometry.

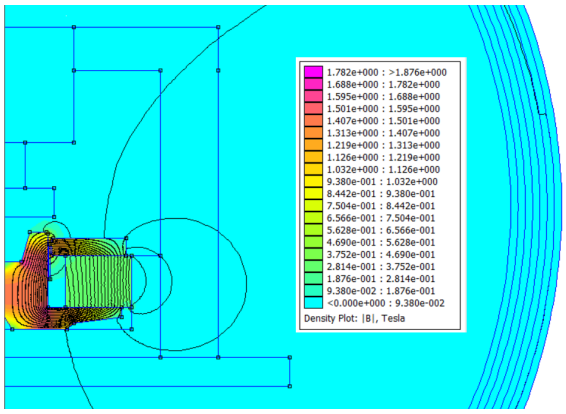


(a) Magnetostatic solution.

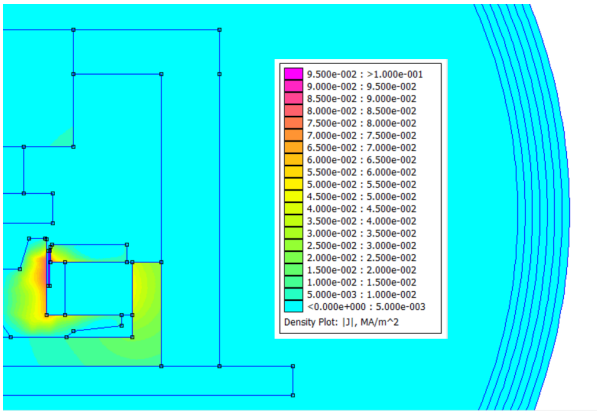


(b) Induced Currents at 10 Hz.

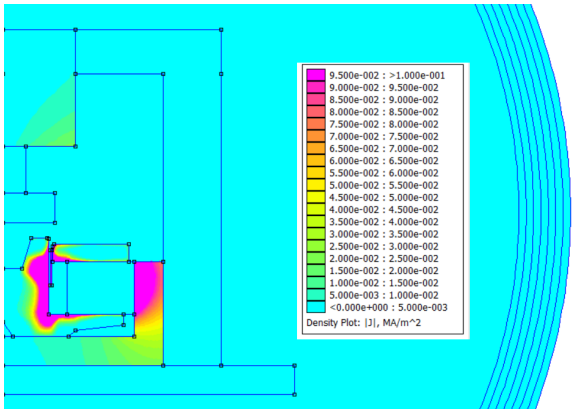


(c) Induced Currents at 100 Hz.

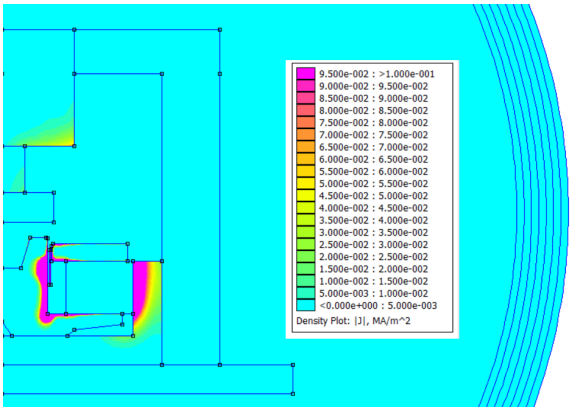


(d) Induced Currents at 1000 Hz.

FIGURE 2.18 – Jig Electromagnetic FEA study. (a) : Magnetostatic solution. The magnetic flux lines do not interact with the Jig. (b), (c), and (d) : Alternative Current (AC) simulation showing the induced current inside the jig structure for 10 Hz, 100 Hz and 1 kHz.

## 2.6 Controller

The algorithms presented in this work are discrete algorithms. They therefore require a processor to execute the mathematical operations in order to function. These operations must be performed quickly as the algorithms are to be used in real time. They also require information from the analog domain, the stimulus and also any other required signals such as those used for feedback. These analog stimuli must therefore be conditioned and discretised for use in the processor.

Audio is traditionally 16 or 24 bit data sampled at a minimum of 44.1 kHz. If we are not to loose too much information, the analog to digital converters (ADCs) used in this project must be at least 16 bit capable. Another important factor to consider is the type of ADC. There are two main choices for ADCs on the market. Successive Approximation Register (SAR) and Sigma Delta ($\Sigma\Delta$). SAR ADCs tend to have lower latency compared to $\Sigma\Delta$ ADCs as a single N bit conversion takes N cycles to compute on a SAR ADC versus $2^N$ cycles on a $\Sigma\Delta$ ADC. This has a direct influence on the amount of feedback that can be implemented with the micro controller. Lower latency means more feedback can be applied before the loop stability is compromised.

Once discretised, the signals are used in a compensation algorithm. This algorithm is composed of polynomial functions, nonlinear ordinary differential equations (ODEs) and the required numerical methods to approximate the solutions to the aforementioned ODEs. All of these methods can be performed using basic mathematical operations $+ - \times \div$, but do require relatively high numerical accuracy. Finally, for ease of use, it would be preferable to be able to use single precision floating point data types. The processor must therefore be capable of performing Floating Point (FP) calculations. The time limit for the acquisition, conversion, computations and output is defined by the sampling frequency used. At 48 kHz, all of the operations must be finished in under 20.83 µs.

The output of the compensation algorithm must then be converted into an analog signal so that it may be applied to a power amplifier. This is done through a digital to analog converter (DAC). The DAC must be capable of at least 16 bits to provide enough dynamic range for the compensation signal. It must also have a settling time that is less than the sample rate.

Finally, one very important criteria which must be taken into account is the availability of the components. At the time of writing, the global chip shortage and the CoVid pandemic have severely limited the quantity of available components. For example, the power transistors required for the output stage of the power amplifier designed during this PhD were ordered in June 2021 but were not delivered until January 2022.

### 2.6.1 Teensy 3.6

The choice of processor hardware was made based around the need for at least two 16 bit ADCs, the ability to perform very fast floating point calculations, and the availability at a low cost.
The Teensy 3.6 fulfils all of the aforementioned requirements while using the Arduino Integrated Development Environment (IDE). The programs are coded in C++, using the free TeensyDuino add on. There is a very active forum with a number of extremely valuable user contributions, some of which were used for this work.
The Teensy 3.6 is based around an ARM Cortex M4 running at 180 MHz, which may be overclocked up to 240 MHz in the IDE. The actual chip used is an NXP MK66FX1M0VMD18. It includes two 16 bit capable SAR ADCs which have access to 25 inputs between them. It also has a Floating Point Unit (FPU) which is used to perform hardware 32 bit math operations on floating point numbers. Although the included DACs are only 12 bits, the Teensy 3.6 is capable of communicating via Serial Peripheral Interface (SPI) at up to 50 MHz with any compatible hardware. As such, adding a 16 bit SPI DAC is extremely simple, and requires 6 lines of code to perform the SPI transaction. Finally the Teensy 3.6 is available from a variety of different retailers for a price of around 35 Euros.

#### ADCs

The NXP MK66FX1M0VMD18 has two SAR ADCs that may access 25 different pins on the Teensy PCB. The ADCs can use an internal 3.3 V reference or an externally provided reference voltage for the conversion. The ADCs are capable of up to 16 bit resolution, however due to various sources of noise the Effective Number Of Bits (ENOB) is usually specified at 13 bits for a single ended input. Thus if the overall noise is to be kept low, extra care must be taken when designing the signal conditioning section.

#### Signal Conditioning

To ensure accurate data with as little noise as possible, an adequate analog signal conditioning circuit is designed. The signal conditioning circuit is composed of three stages and illustrated in Figure 2.19. The first stage is where the signal is combined with the bias voltage required by the ADC. This bias voltage $U_{bias}$ is set at 1.65 V, half the ADC reference voltage and provided by a precision voltage reference, a Maxim Integrated MAX6043CAUT33+T. This chip is also used to provide a clean reference for the ADC conversion. In order to ensure that no external Direct Current (DC) voltages hamper the performance of the $1^{st}$ stage, the input signal $U_{in}$ is AC coupled via capacitor $C_{DC}$. The capacitor value is made extremely large (1 mF) which ensures a very low cut off frequency

of approximately 7 mHz. The second stage is where the signal is low pass filtered. The filtering is done by $2^{nd}$ order filter, with a cut off frequency of 11 kHz. The filter serves several purposes. First it reduces the amplitude of frequencies outside the bandwidth of the compensation algorithm. Secondly, it acts as an anti aliasing filter. Thirdly, it reduces the amount of high frequency noise present at the ADC inputs. The final stage is composed of two components, a resistor $R_c$ and a capacitor $C_c$. The capacitor is there to provide a charge reserve for when the SAR ADC capacitor is connected to the signal to be converted. The resistor is there to help with Op Amp stability.

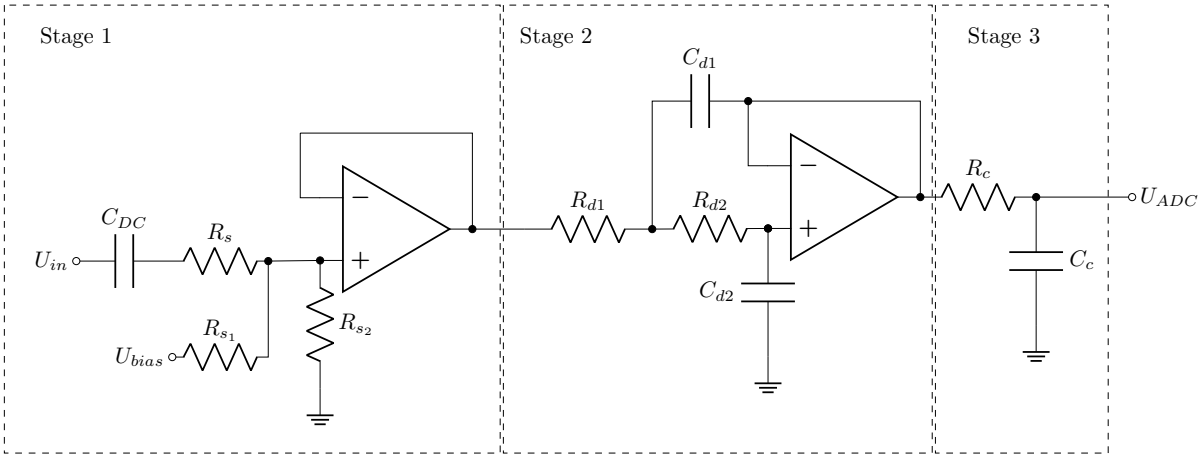


FIGURE 2.19 – Analog Input Signal Conditioning.

Due to the voltage limitations of the Teensy Printed Circuit Board (PCB), voltages above 3.5 V or below -0.2 V will damage the ADCs. There are several ways of protecting the inputs, however in the interest of keeping the circuits simple and without parasitic effects, the following solution was chosen. Rail to Rail Op Amps powered by a single 3.3 V regulated DC voltage were used in the signal conditioning stages. Thus the outputs of the Op Amps cannot be higher than the 3.3 V supply. There are two choices for the Op Amp here, the TI LME49721 or OPA2325. Both can run off a single supply up to 5.5 V and are capable of output voltages within 30 mV of the positive or negative supply.

### DAC

Once the compensation algorithm has approximated the stimulus that is to be applied to the loudspeaker, it must be converted from a digital value into an analog one. The on board DAC is only 12 bits and therefore a higher resolution solution was researched. Aside from having a resolution of 16 bit the other specifications where :

- able to operate at sampling frequencies up to 100 kHz,
- capable of bipolar output,
- low latency and settling time,
- delivery possible in Q1 of 2022.

Three DAC chips where selected :

— Maxim Integrated MAX5717,

— Analog Devices AD5542,

— Texas Instruments DAC8831.

They all satisfy the first three criteria, but the quantities available vary rapidly. However, these three DAC chips all have the same foot print and chip pin associations. This means that they can all be used on a PCB designed around one of them.

### DAC Output

As we require a bipolar signal, the DAC is connected to an external Op Amp as shown in Figure 2.20. In this case, an Analog Devices ADA4084-1 precision op amp was used as it provides a low noise, low offset and rail to rail solution. The output of the ADA4084-1 is then buffered and low pass filtered using another Sallen Key low pass filter with the same characteristics as used for the inputs.

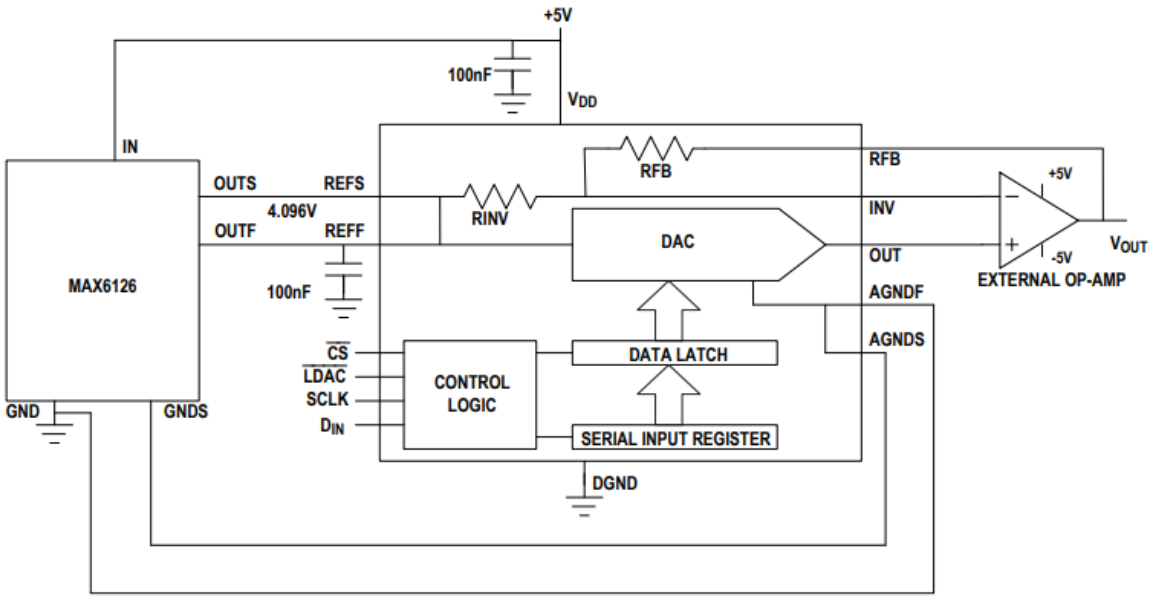


FIGURE 2.20 – Circuit for bipolar output, from [63].

## 2.6.2 Controller Performance

It is important to characterise the performance of the completed circuits in terms of noise, distortion and delay. The amount of noise and distortion influences the efficiency of the compensation, and the delay defines the amount of feedback that is applicable before the system becomes unstable. This chapter provides some basic specifications for the controller. To characterise the controller, stimuli are generated in Python and a DT9837C

DAQ is used to both apply the stimuli and measure the various quantities. The DT9837C is set to run at a sampling rate of 96 kHz, and the inputs DC coupled.
The various Teensy parameters are defined as follows :

— sampling frequency : 100 kHz,
— ADC averages : 1,
— ADC sampling speed : Medium Speed,
— ADC conversion speed : Medium Speed,
— DAC SPI Frequency : 22.5 MHz,
— Micro Controller (µC) Frequency : 180 MHz.

### Frequency Response

In order to analyse the frequency response, an exponential sweep was applied to the controller input with the following specifications :

— start Frequency : 0.001 Hz,
— end Frequency : 48000 Hz,
— amplitude : 2.5 $V_{peak}$,
— duration : 200 s.

As can be seen in Figure 2.21f, the overall frequency response is a band pass, with a first order high pass at approximately 7 mHz, and a fourth order low pass filter resulting from the cascaded input and output filters.

### Noise, Distortion

To characterise the noise and distortion of the circuit, two types of stimuli are used, sine waves and multitone. For the sine wave, three different frequencies are used to characterise the system, whereas for the multitone ten simultaneous frequencies are used. All the signals have a peak value of 2.5 V. The stimulus is generated in Python and applied to one of the controller inputs with a DT9837C DAQ. Both the controller input and output signals are acquired using the DAQ and post processed in Python. For the sine wave analysis, a Fast Fourier Transform (FFT) is performed using a rectangular window over 4 seconds of data. The results are shown in Figures 2.21a, 2.21b and 2.21c. It is possible to calculate the Signal to Noise And Distortion ratio (SINAD) and thus the ENOB of our system [97]. The SINAD is calculated as the ratio of signal power to noise and distortion power as in,

$$SINAD = \frac{P_{fund}}{P_{noise} + P_{distortion}} \tag{2.34}$$

and the *ENOB* as,

$$ENOB = \frac{SINAD - 1.76}{6.02}. \tag{2.35}$$

The fundamental power $P_{fund}$ is obtained by squaring the amplitude of the data in the frequency bin corresponding to the fundamental frequency. The noise and distortion powers ($P_{noise}$ and $P_{distortion}$) are calculated by squaring the amplitude of the data in all of the other frequency bins between 0 Hz and the Nyquist frequency, 48 kHz.
With the data shown in Figures 2.21a, 2.21b and 2.21c the average ENOB/SINAD for the Controller is :

— SINAD Controller : 75.6 dB,

— ENOB Controller : 12.27 bits.

It should be noted here that if a source with lower noise and distortion is used such as a Rhode & Schwarz Audio Analyser, the Controller ENOB and SINAD are lower at :

— SINAD Controller : 82 dB,

— ENOB Controller : 13.32 bits.

These numbers may seem rather poor at a first glance, so it was deemed important to put them into perspective. The data sheet of the chip used in the Teensy 3.6 specifies an ENOB of between 11.4 and 13.1 bits when the ADC is used in single ended mode and with **4** averages. Here we do not average the signal and we still end in the specified values.
It is also important to provide a comparison with commercial products. The DT9837C data acquisition device uses 24 bit $\Sigma\Delta$ ADCs and DACs and is specified with an ENOB of 14.7 bits when running at 96 kHz.
For the multitone analysis, the FFT is performed over 2 seconds of data using a rectangular window, with the result illustrated in Figure 2.21d. The compensation algorithm is only be useful up to at most 1 kHz, and in this frequency band of interest we have a SINAD of approximately 76 dB.

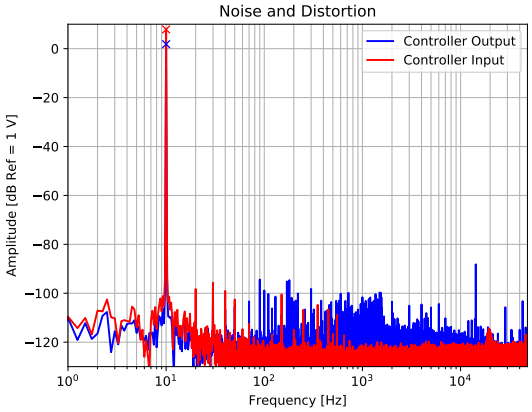


(a) Noise floor and Distortion, 10 Hz. ENOB = 12.30 Bits.

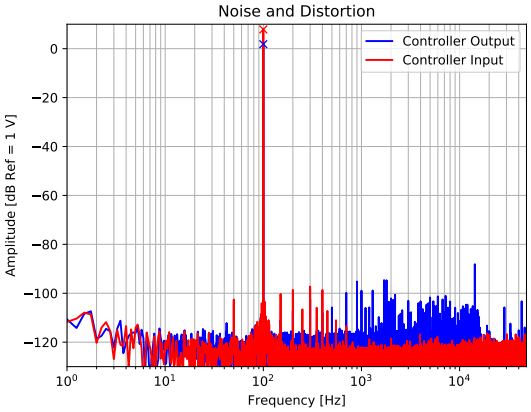


(b) Noise floor and Distortion, 100 Hz. ENOB = 12.31 Bits.

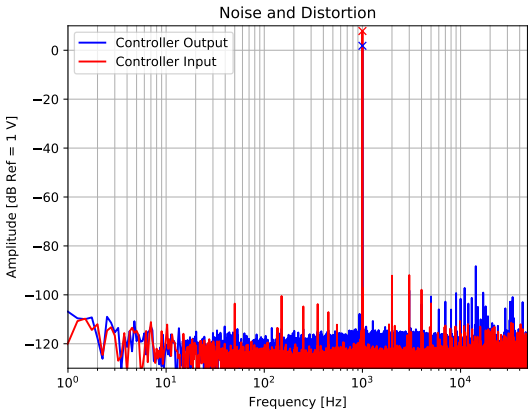


(c) Noise floor and Distortion, 1 kHz. ENOB = 12.22 Bits.

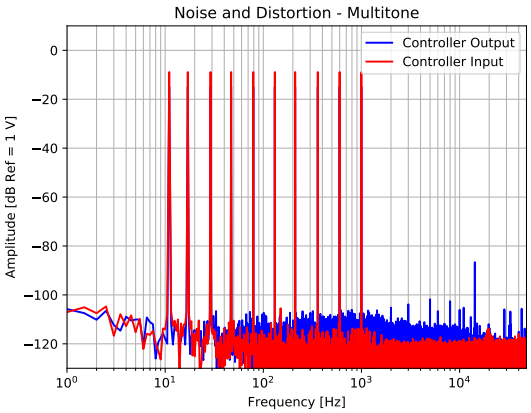


(d) Noise floor, multitone input.

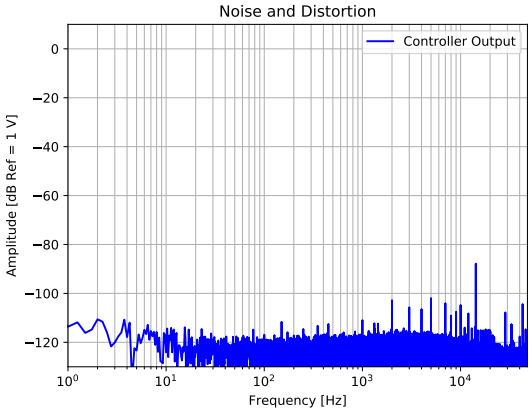


(e) Noise floor, shorted input.

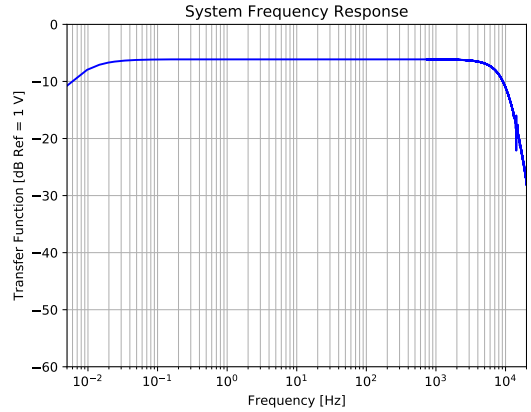


(f) Controller Frequency Response (Modulus).

FIGURE 2.21 – Controller Characteristics. (a),(b),(c) : Harmonic distortion and noise for a 10 Hz sine wave, 100 Hz sine wave, and a 1000 Hz sine wave. (d) : Noise floor and distortion for a multitone signal. (e) : Noise floor with a shorted input. (f) : Frequency response (modulus) measured using a logarithmic chirp signal.

### Group delay and Latency

As mentioned previously, the total time required for a signal to pass through the controller is important. As we have a mixture of analog and digital sections, the total time delay is a combination of group delay and latency. The group delay is caused by any filters, whereas the latency is due to analog to digital conversions, processing and the digital to analog conversion. To this end, the controller is stimulated with a 0.05 $V_{peak}$ 100 Hz sine wave. The total time delay can be approximated through the use of a cross correlation of the input and output signals, giving 72 µs. The theoretical group delay at 100 Hz resulting from a single $2^{nd}$ order low pass filter with a cut off frequency of 11 kHz is around 20 µs, and as there are two low pass filters (one on the input and one on the output), the latency of the controller is around 32 µs.
Table 2.1 summarises the performance of the controller using several well known metrics, while Figure 2.22 shows two photos of the finished product. An earlier iteration of the controller was also analysed and the work presented in [71].

| Characteristics | | | |
|---|---|---|---|
| Parameter | Value | Unit | Notes |
| Output DC Offset | 4.5 | mV | Shorted input |
| Input Full Scale Voltage | 3.2 | V | Peak Voltage |
| Output Full Scale Voltage | 4 | V | Peak Voltage |
| Bandwidth | 8.5 | kHz | -3dB |
| Input High Pass | 7 | mHZ | -3dB |
| Input Low Pass | 11 | kHz | -3dB |
| Output High Pass | - | Hz | DC Coupled |
| Output Low Pass | 11 | kHz | -3dB |
| Total delay | 72 | µs | @ 100 Hz |

Table 2.1 – Controller Specifications

## 2.7 Conclusion

The topic of loudspeaker control and linearisation often concentrates on mathematical models and various feedback techniques and sensors, it is however much more complicated than that. This section has provided a short overview of the various subsystems and algorithms that were required and developed in order to proceed with real time loudspeaker control and linearisation. In terms of software, two techniques were developed :

1. a simple algorithm was presented that enables the approximation of the roots of a nonlinear implicit quadratic equation,
2. an algorithm couples error correction and gradient descent with feed forward nonlinear modelling,

which may be used to reduce the nonlinearities of a loudspeaker. Several hardware systems were also designed in order to provide :

1. clean data for model parameter fitting,
2. adapting common voltage amplifiers for current output,
3. low latency audio algorithm processing.

All of these subsystems will be assembled into the overall real time loudspeaker control system which will be assessed in the next sections, first with some simulations and then with real world data.

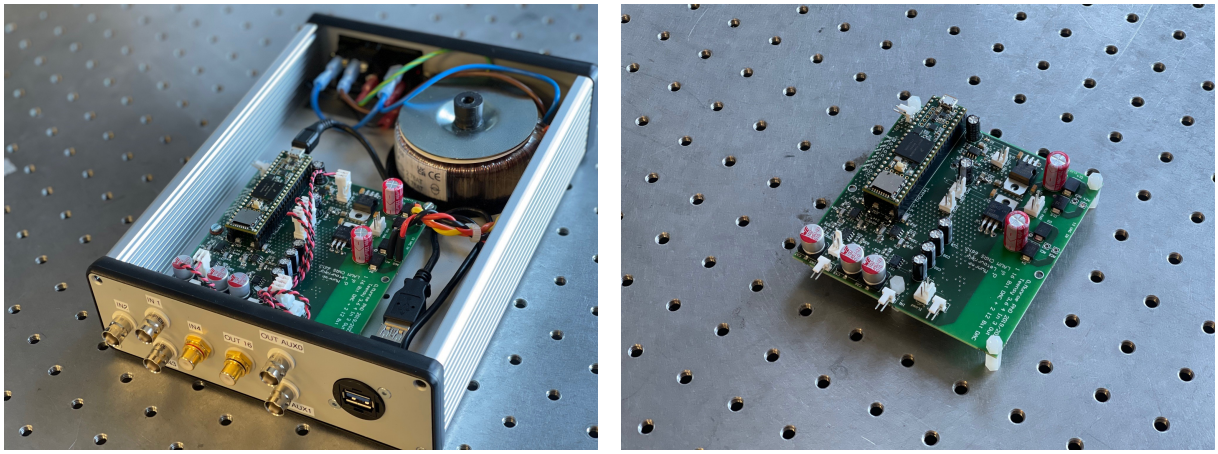

(a) Controller, V3. (b) Controller Printed Circuit Board.

FIGURE 2.22 – Finished Controller. (a) : Finished V3.0 controller. (b) : Photo of the populated controller PCB.

Chapitre 3

# Results

## 3.1 Introduction

This chapter is divided into two sections. The first section uses a digital twin of the linearisation system to investigate the effects of ADC/DAC resolution, modelling error and the effect of mechanical damping. The second section shows the results of applying the correction system to the loudspeaker system described in Chapter 2. The compensated system is compared against a non compensated current driven loudspeaker and a non compensated voltage driven loudspeaker. A further comparison is performed against an uncompensated voltage driven loudspeaker system where the drive unit has an aluminium shorting ring. Finally, the algorithm is modified to output a control signal proportional to a voltage instead of a current, and applied to the loudspeaker using a voltage source.
For this section, the stimulus used is a multitone signal with 10 non harmonic frequencies logarithmically spaced between 10 Hz and 1000 Hz. The signal lasts 4 seconds and is windowed using a Tukey window. The multitone distortion components are converted to MTND curves using a frequency window of 40 points between 10 Hz and 4000 Hz. The average compensation displayed inside the plots is derived from compensation data between 10 Hz and 4000 Hz.

## 3.2 Simulations

### 3.2.1 Digital Twin

A digital twin is a discrete model of a real system. The discrete model may be very simple or very complicated. It can be useful to see how the system may react to certain changes, without having to build or implement the changes in reality and test them. In the case of this thesis, a digital twin of the compensation system is made using state space models. The input and output conditioning is modelled by a system of differential equations where the op amps are assumed to be perfect. The Sallen Key filter as shown in Figure 3.1 is modelled using two first order differential equations,

$$\begin{cases} U_+ &= U_{out} \\ \frac{dU_{out}}{dt} &= \frac{U_A - U_{out}}{R_{d2}C_{d2}} \\ \frac{dU_A}{dt} &= \frac{U_{in} - U_A}{R_{d1}C_{d1}} - \frac{C_{d2} - C_{d1}}{C_{d1}} \frac{dU_{out}}{dt} \end{cases} \tag{3.1}$$

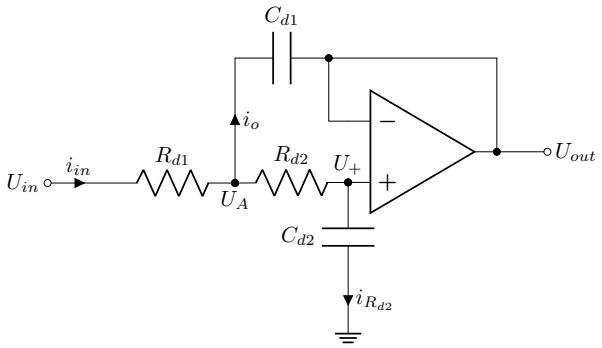


FIGURE 3.1 – Sallen Key Nodes and Currents

The N bit ADC conversion is modelled by first adding the bias voltage to the signal applied to the ADC input, $ADC_{in}$, converting it to an unsigned 16 bit integer,

$$ADC_{int} = \frac{2^N - 1}{U_{ref}}(ADC_{in} + U_{bias}), \tag{3.2}$$

with $U_{ref}$ the ADC reference voltage, then converting this back to volts as done in the Teensy code,

$$ADC_{volt} = \left(\frac{U_{ref}}{2^N - 1} ADC_{int}\right) - U_{bias}. \tag{3.3}$$

The Teensy performs all the calculations on 32 bit floating point numbers in the FPU so all of the variables used in the Teensy simulation are designated as 32 bit floating point numbers. The DAC output is simulated the same way as the ADC input, but in reverse.

In order to approximate the difference between the Teensy sampling frequency and the infinite sampling frequency of the analog sections, a sampling frequency of 960 kHz is used for the analog sections and a sampling rate of 96 kHz is used to model the operations performed by the Teensy.

### 3.2.2 Perfect Compensation

The first thing evaluated is the maximum amount of compensation that can be obtained when there is no noise of any sort in the system, no mains hum from ground loops and where the model is 100% accurate. This serves to provide an unobtainable asymptotic value. As explained in the materials and methods section, the target for the compensation is a linear loudspeaker driven by a voltage source and as such the compensated loudspeaker should not exhibit a peaking response around the resonance frequency. Figure 3.2 shows the best case compensation efficiency for a peak displacement of 5.4 mm and 0.5 mm using a true 16 bit system, while Figure 3.3 shows the same results but when comparing a 12 bit compensation system to a 16 bit uncompensated system. Overall the compensation efficiency is better than 30 dB for both cases at the high displacement amplitude where there is a large amount of distortion, however for low displacement amplitudes the 12 bit system cannot reduce the distortion as it is below the resolution of the system.

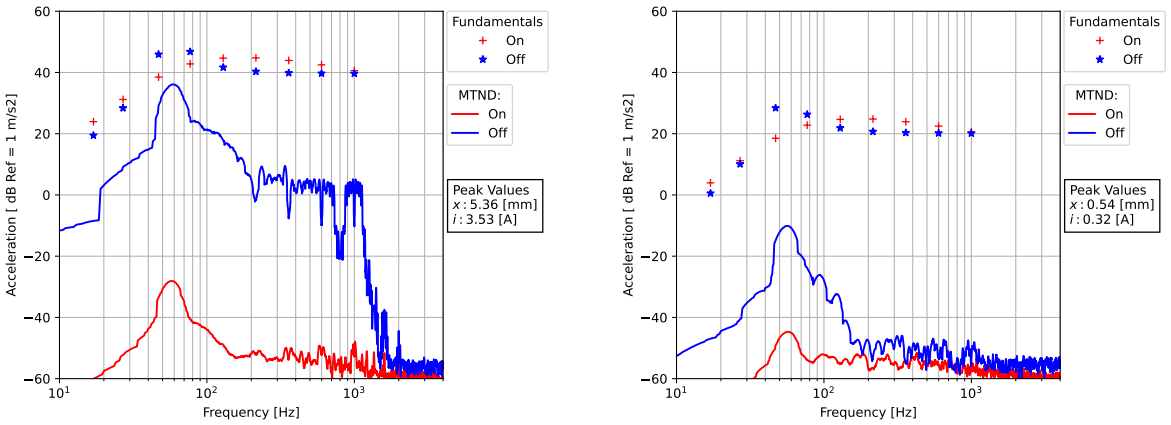


(a) Best case compensation at ±5.4 *mm*.

(b) Best case compensation at ±0.5 *mm*.

FIGURE 3.2 – Best case compensation with 16 bit ADC and DAC. Blue indicates the uncompensated system, while red indicates the compensated system. (a) : Best case compensation for a high displacement level. (b) : Best case compensation for a low displacement level.

It is clear that the true 16 bit system is superior, and therefore the simulation results that follow are performed using the assumption of a true 16 bit system.

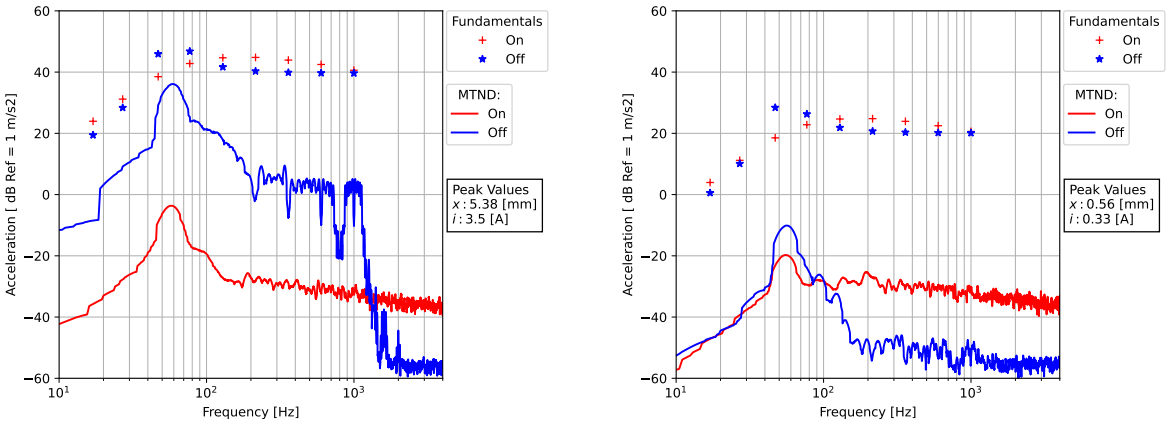


(a) Best case compensation at $\pm 5.4\ mm$.

(b) Best case compensation at $\pm 0.5\ mm$.

FIGURE 3.3 – Best case compensation with 12 bit ADC and DAC. Blue indicates the uncompensated system, while red indicates the compensated system. (a) : Best case compensation for a high displacement level. (b) : Best case compensation for a low displacement level.

### 3.2.3 Influence of model errors

The digital twin can also be used to simulate the effects of the model errors on the compensation efficiency. In this section we will simulate some basic errors for the nonlinear parameters $Bl(x)$, $K_{ms}(x)$ and $L(x)$. It is recalled that for this work, the $K_{ms}$ term regroups all the suspension elements (spider, surround and enclosure air spring). In order to only observe the influence of the feed forward model, no error correction or gradient descent is used here. The algorithm used is shown in Figure 3.4.

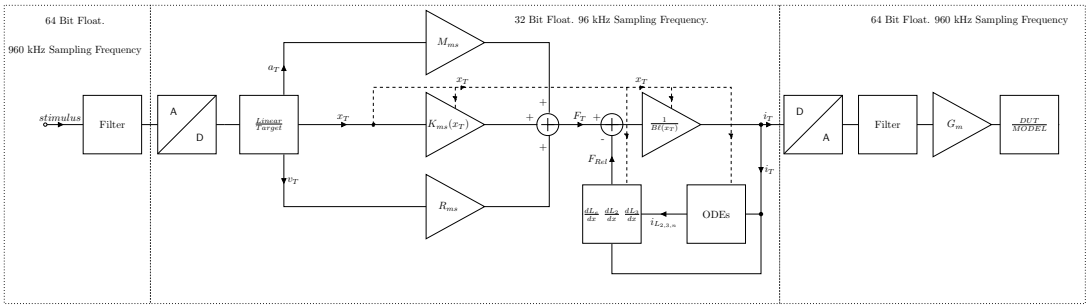


FIGURE 3.4 – Digital twin algorithm structure. Dashed lines indicate the variable is used for the nonlinear functions.

#### Model Error - $K_{ms}(x)$ Error

Here we simulate influence of the stiffness error on the compensation efficiency. The DUT and model stiffness functions can be seen in Figure 3.5a, with the relative error shown in Figure 3.5b. The results of the compensation with a 10% relative magnitude error on

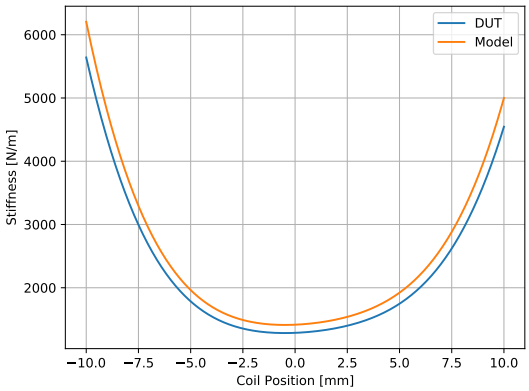


(a) Stiffness, DUT Vs Model.

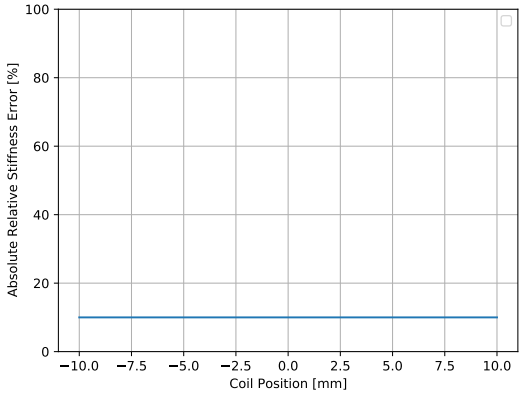


(b) Stiffness Relative Magnitude Error.

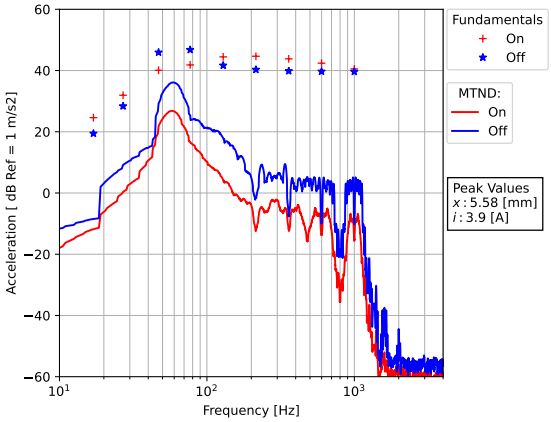


(c) Compensation with 10% Stiffness error at $\pm 5.5\ mm$.

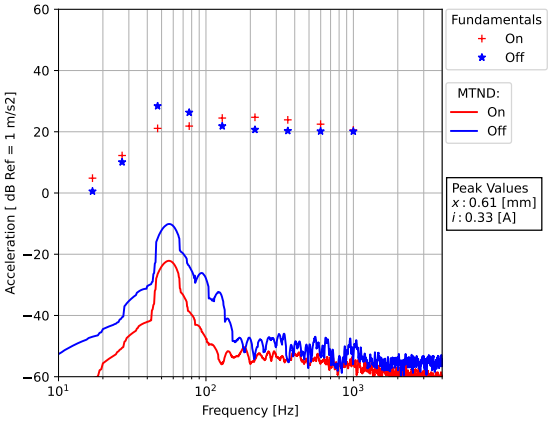


(d) Compensation with 10% Stiffness error at $\pm 0.6\ mm$.

FIGURE 3.5 – Stiffness modelling error and associated compensation efficiency. (a) : Mechanical stiffness, Model versus DUT. (b) : Relative magnitude error associated with (a). (c),(d) : Compensation for a low and high displacement levels. Blue indicates the uncompensated system, while red indicates the compensated system.

the $K_{ms}$ term can be observed in Figures 3.5c and 3.5d. The $K_{ms}$ modelling error renders the compensation scheme less efficient, with a 10% error resulting in an average of 10 dB of distortion reduction. There is a large peak in the distortion around the resonance frequency which is due to the low amount of system damping, and the fundamental response is slightly bumpy in the frequency band.

### Model Error - $B\ell(x)$ Error

Here we simulate influence of the force factor error on the compensation efficiency. The DUT and model force factor functions can be seen in figure 3.6a. Similar to the case with

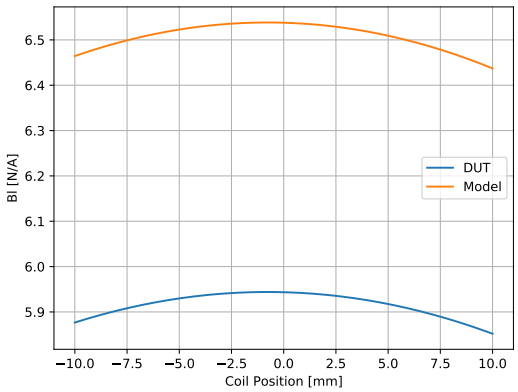


(a) Force Factor, DUT Vs Model.

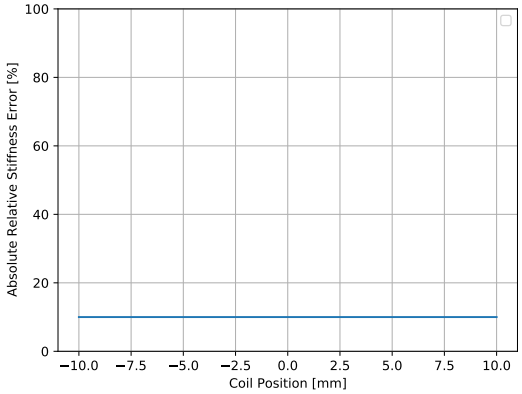


(b) Force factor Relative Magnitude Error.

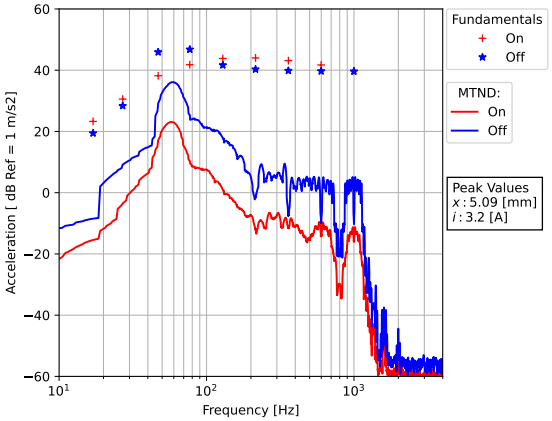


(c) Compensation with 10% $B\ell$ error at $\pm 5.0\ mm$.

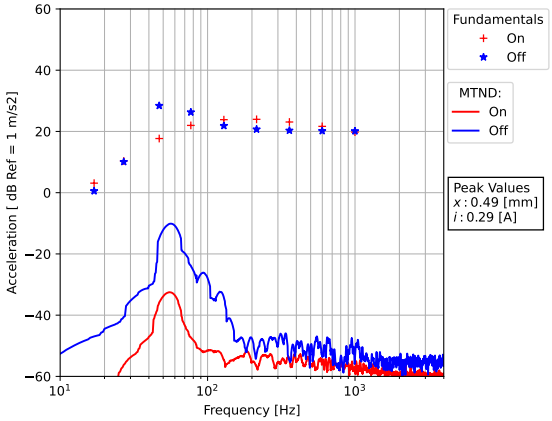


(d) Compensation with 10% $B\ell$ error at $\pm 0.5\ mm$.

FIGURE 3.6 – $B\ell(x)$ modelling error and associated compensation efficiency. (a) : $B\ell(x)$, Model versus DUT. (b) : Relative magnitude error associated with (a). (c),(d) : Compensation for a low and high displacement levels. Blue indicates the uncompensated system, while red indicates the compensated system.

the $K_{ms}$ modelling error, an error in the $B\ell$ parameter renders the compensation less efficient. There is again the large distortion peak at the resonance frequency, however the fundamental response is smoother around this frequency.

### Model Error - Inductance Error

Here we simulate influence of the inductance error on the compensation efficiency. The polynomial functions representing the inductance are multiplied by a factor of 1.1, representing a error of 10%.

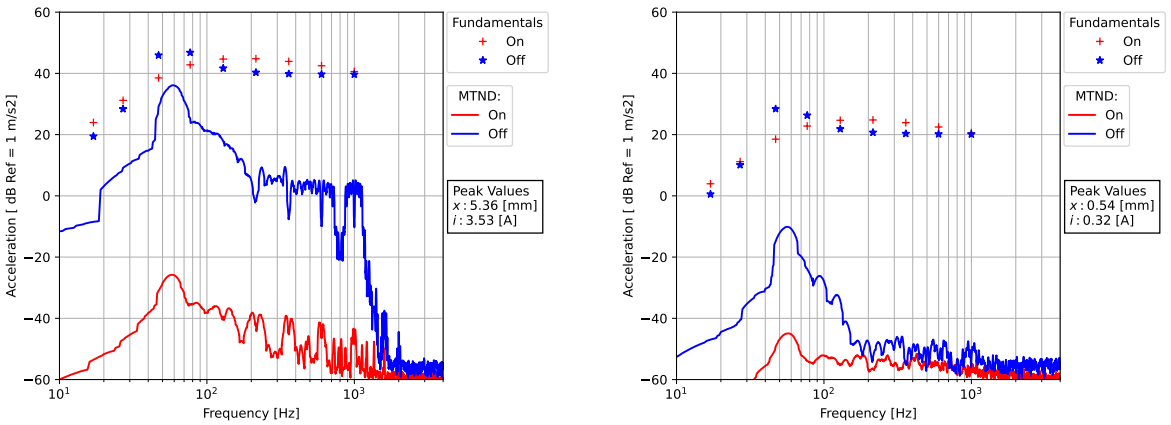


(a) Compensation with 10% $L$ error at $\pm 5.4\ mm$.

(b) Compensation with 10% $L$ error at $\pm 0.54\ mm$.

FIGURE 3.7 – Inductance modelling error and associated compensation efficiency. (a),(b) : Compensation for a low and high displacement levels. Blue indicates the uncompensated system, while red indicates the compensated system.

Here we can observe how the use of an amplifier with a high output impedance renders the compensation scheme indifferent to errors in the inductance model. This can be explained by the fact that the inductance can only influence the compensation algorithm through the reluctance force, which is relatively low in amplitude for the currents used here.

### Error, first summary

It is possible to observe the influence of the various errors by stepping the relative model error from -30% to +30%, and computing the average compensation. Figure 3.8b shows the average compensation for various amounts of error, while Figure 3.8a shows the compensation with 10% relative magnitude error on all nonlinear terms.
Overall, we can see that the compensation is most sensitive to errors in the stiffness $K_{ms}$ and force factor $B\ell$, while errors in the inductance have very little effect. In order to obtain a compensation efficiency of 20 dB, the model error must be less than 10 %.
An interesting point is that it is better to overestimate the force factor than underestimate it, which can be explained by

$$i \approx \frac{F_t - F_{rel}}{B\ell}. \tag{3.4}$$

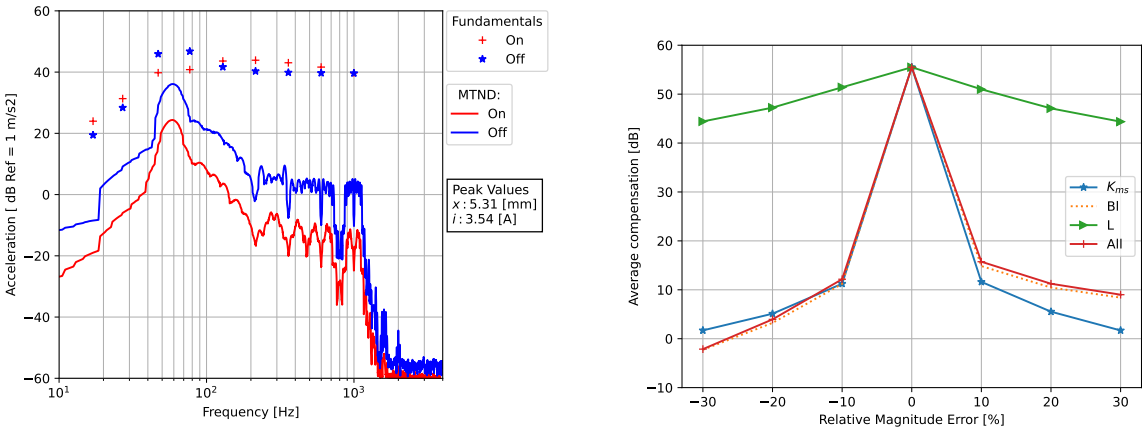


(a) Compensation with 10% error on $Bl$, $Kms$ and $L$ at $\pm 5.32$ $mm$.

(b) Compensation efficiency versus model error.

FIGURE 3.8 – Modelling error and associated compensation efficiency. (a) : Compensation for a high displacement levels, 10% error on all parameters. Blue indicates the uncompensated system, while red indicates the compensated system. (b) : Average compensation efficiency versus modelling error.

If $B\ell$ is underestimated, then the current will be higher in amplitude, resulting in larger coil displacement, power dissipation and reluctance force.

A final point that is worth making is that when using a current source to apply the correction, the lack of electromagnetic damping results in an amplification of the distortion products around the resonance. This phenomena is not seen when performing the usual battery of sine wave and Intermodulation Distortion (IMD) tests as it requires frequencies created by the nonlinear system that are situated around the resonance frequency. Usually the IMD tones are designed to use a 'bass' tone below 100 Hz and a 'voice' tone between 200 and 500 Hz, thus missing the creation of difference tones in the 40 - 80 Hz range. The amount of amplification of the distortion products seems to be directly linked to the amount of mechanical damping present in the system.

Two questions arise from this first summary. Is it possible to differentiate between an error in the $B\ell$ and an error in the $K_{ms}$, and what is the effect of an increase in the mechanical damping on the compensation efficiency with the relative magnitude errors presented here. The next two sections will attempt to clarify if not reply to these questions.

**Differentiation between an error in $B\ell$ and $K_{ms}$**

Figure 3.9 shows the harmonic distortion (HD) and IMD products for a 30% error in either the $B\ell$ or $K_{ms}$ parameters. The Harmonic Distortion (HD) terms are extracted from the total distortion data by simply looking at the harmonics (up to the $10^{th}$) of the fundamental frequencies. The IMD terms are defined as everything that is not one of the HD terms.

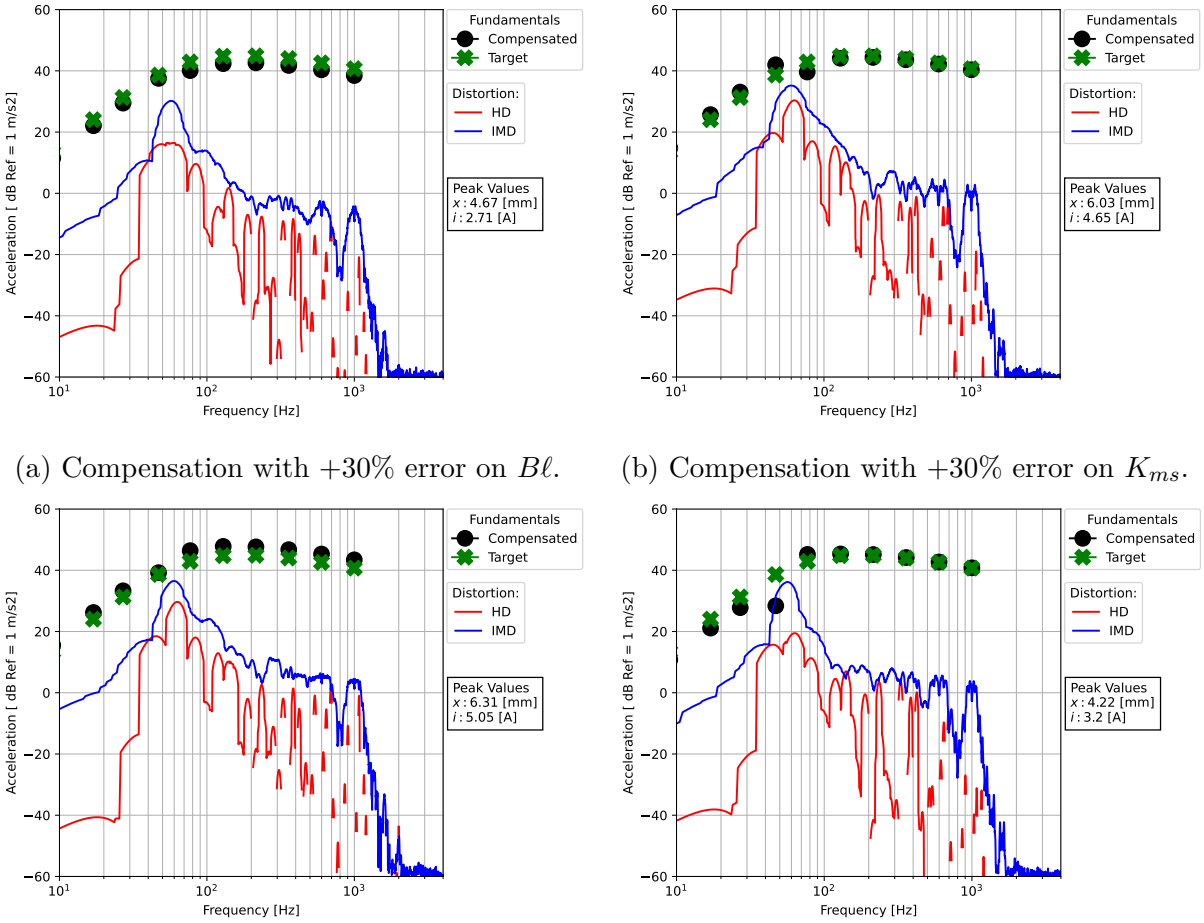


(a) Compensation with +30% error on $B\ell$.

(b) Compensation with +30% error on $K_{ms}$.

(c) Compensation with -30% error on $B\ell$.

(d) Compensation with -30% error on $K_{ms}$.

FIGURE 3.9 – Harmonic and Intermodulation terms for an error in $B\ell$ or $K_{ms}$. Green crosses indicate the target behaviour and black dots indicate the compensated system behaviour. The Blue continuous curve shows the IMD products while the Red discontinuous curve represents the HD products. (a),(c) : Compensation results with 30% Error on the $B\ell(x)$ parameter. (b),(d) : Compensation results with 30% Error on the $K_{ms}(x)$ parameter.

Overall, the difference between the two errors is not really obvious when looking at the HD or IMD data. The real clues come from the fundamentals. In the case of an error on $B\ell$, the fundamentals are effected over the entire bandwidth, whereas in the case of an error on $K_{ms}$ only frequencies around and below the resonance frequency are effected. This can be explained by the fact that $B\ell$ will effect the system over the whole bandwidth

due to it being the main transduction parameter, while the $K_{ms}$ term mainly effects the displacement and the resonance frequency.
An interesting observation of Figure 3.9 is that in the case of a multitone stimulus, most of the distortion comes from the intermodulation products and not the harmonic frequencies of the fundamentals, especially for frequencies not around the resonance frequency.

### Mechanical damping

In order to investigate the influence of the mechanical losses on the compensation efficiency and in particular the robustness of the algorithm when confronted with modelling errors, the mechanical loss $R_{ms}$ is increased from 0.5 Nm.s$^{-1}$ to 10 Nm.s$^{-1}$. This increase represents the equivalent loss increase provided by the electromagnetic damping when driving the system using a voltage source. The equivalent mechanical resistance of the $B\ell/R_e$ combination can be calculated using

$$R_{em} \approx \frac{B\ell^2}{R_e}, \tag{3.5}$$

where $R_{em}$ is the electromagnetic damping in the mechanical domain.

Figure 3.10 illustrates the compensation efficiency with different model errors for the case where the mechanical damping is increased. Overall the increase in mechanical damping renders the compensation more efficient, especially around the resonance frequency. Combining this with the results from [7], it would seem that a larger amount of damping in the system renders the compensation more robust in the face of modelling errors.

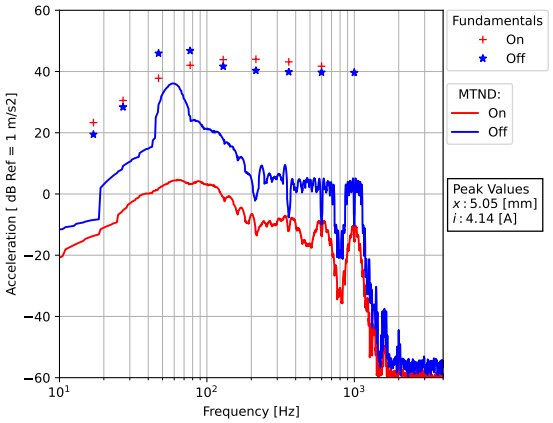


(a) Compensation with 10% error on $B\ell$.

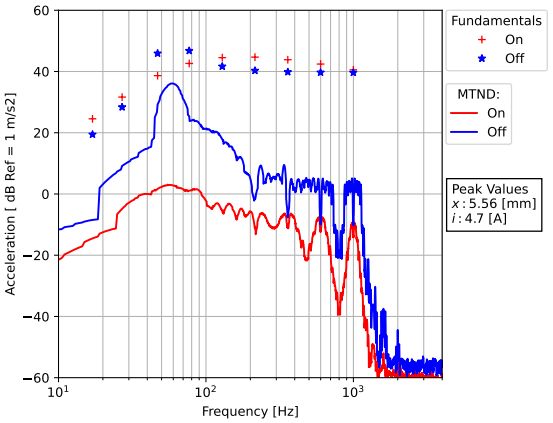


(b) Compensation with 10% error on $K_{ms}$.

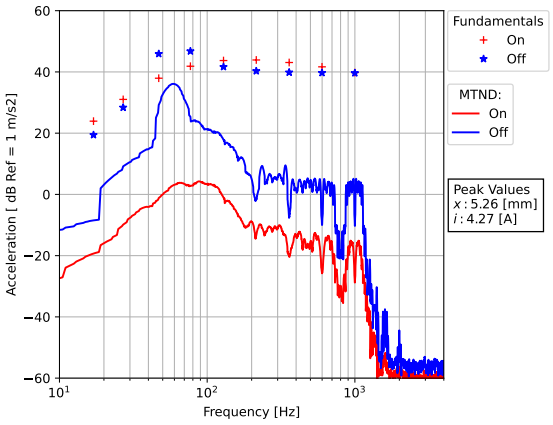


(c) Compensation with 10% error on all parameters.

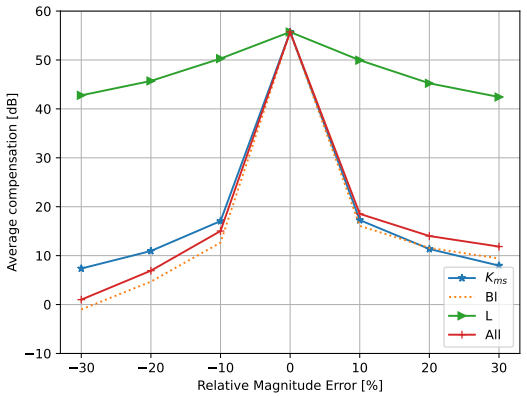


(d) Compensation with model error with $R_{ms} = 10$.

FIGURE 3.10 – Compensation efficiency with model error with $R_{ms} = 10$. Blue indicates the uncompensated system, while red indicates the compensated system. (a),(b),(c) : Compensated versus uncompensated system, 10% error on $B\ell(x)$, $K_{ms}(x)$, and $L(x)$. (d) : Resulting average compensation efficiency versus model error.

## 3.3 Measurements

For the measurements, the controller is set to run at a sampling frequency of 96 kHz while performing simultaneous ADC conversions for the stimulus and drive unit terminal voltage.

### 3.3.1 Comparison with an uncompensated current driven loudspeaker

#### Linearisation Without Error Correction and Real Time Optimisation

Figure 3.11 shows the compensation efficiency when the algorithm is used in pure feed forward mode and compared against an uncompensated system using a transconductance power amplifier. There is no error correction or gradient descent to reduce the error.
The average overall compensation is around 12.5 dB and is relatively constant with frequency. There is a large distortion peak at the resonance frequency that can be attributed to the low mechanical loss (Section 3.2.3). For the higher output levels as shown in Figures 3.11b and 3.11c, the fundamental frequencies around the resonance between 40 Hz and 100 Hz show a slight dip, which indicates an error in the modelling of the suspension as in Section 3.2.3. The fact that the amount of compensation decreases with the peak displacement level may be due to some missing phenomena in the model, something that is still present for low amplitude displacements and currents. It is possible that magnetic and/or mechanical hysteresis is one of the causes here, however this is only a hypothesis and must be verified.

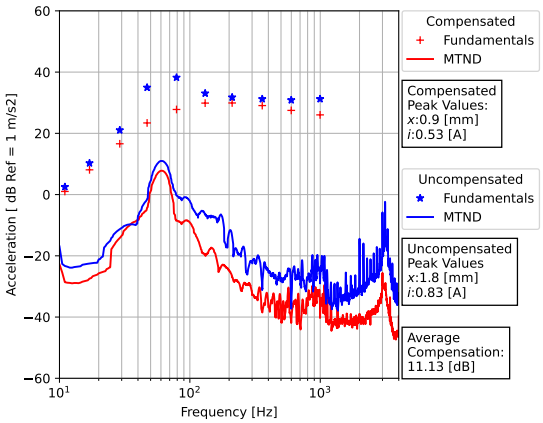


(a) With and without compensation for low peak displacement level.

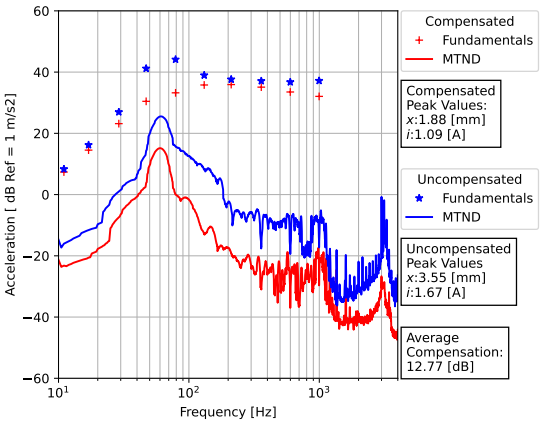


(b) With and without compensation for mid peak displacement level.

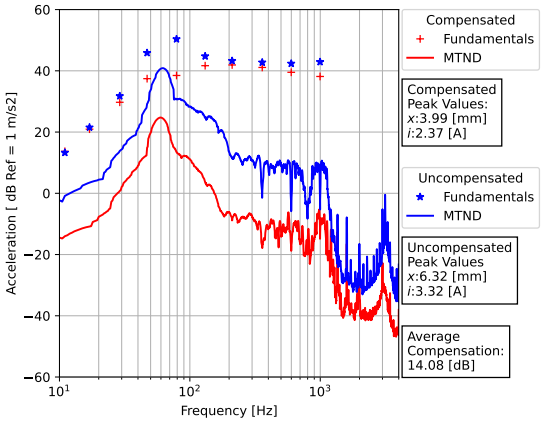


(c) With and without compensation for high peak displacement level.

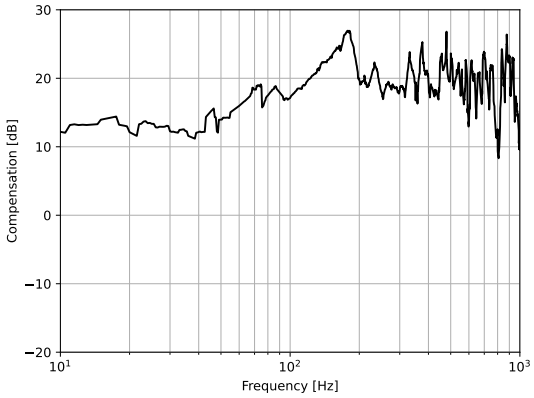


(d) Compensation versus frequency associated with Figure 3.11c, bandwidth cropped to 10 Hz - 1000 Hz.

FIGURE 3.11 – Compensation using data sheet values and nonlinear $K_{ms}$. Red indicates data with compensation, blue is without. The continuous curves show the MTND, whereas the + and $*$ show the fundamental frequencies. (a) : With/without compensation for a low level displacement. (b) : With/without compensation for a mid level displacement. (c) : With/without compensation fo a high level displacement. (d) : Amount of compensation versus frequency associated with (c), bandwidth cropped to 10 Hz - 1000 Hz.

### Linearisation With Error Correction and Real Time Optimisation

Figure 3.12, shows the compensation efficiency when the algorithm is used in hybrid mode. The error correction gain is set at 4, and the velocity error is band pass filtered using $1^{st}$ order filters with cutoff frequencies of 0.5 Hz and 250 Hz. The algorithm is allowed to converge during three measurement runs (approximately 12 seconds) before the data is saved and analysed.

The average overall compensation is around 11 dB and is again relatively constant with frequency. The reason the compensation is lower than without the error correction and optimisation is that the feedback and gradient descent add a small amount of noise back

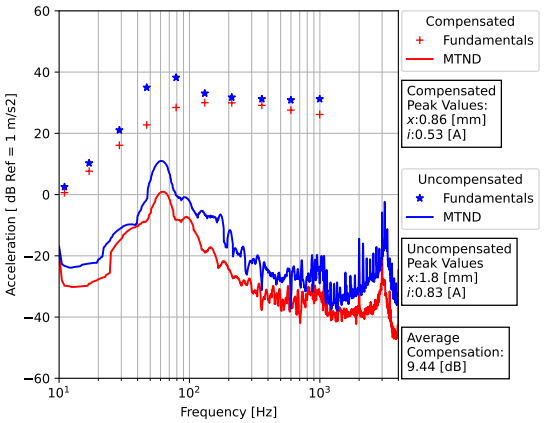


(a) With and without compensation for low peak displacement level.

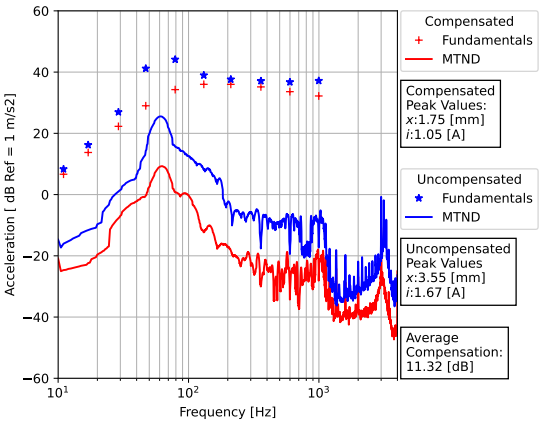


(b) With and without compensation for mid peak displacement level.

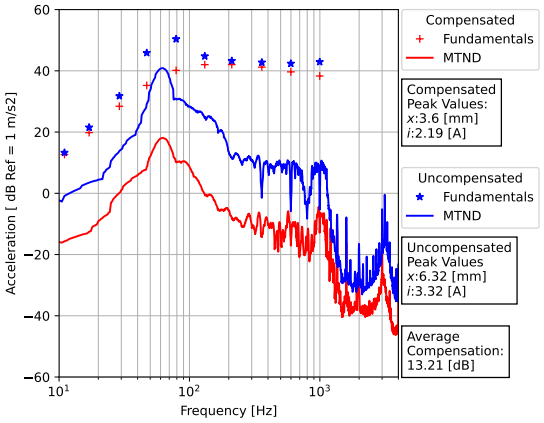


(c) With and without compensation for high peak displacement level.

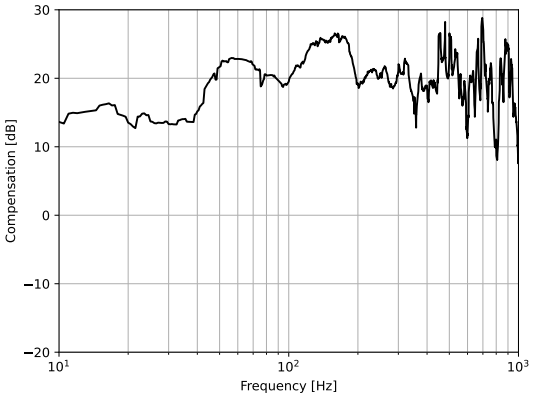


(d) Compensation versus frequency associated with Figure 3.11c, bandwidth cropped to 10 Hz - 1000 Hz.

FIGURE 3.12 – Compensation using error correction and gradient descent. Red indicates data with compensation, blue is without. The continuous curves show the MTND, whereas the + and ∗ show the fundamental frequencies. (a), (b), (c) : With/without compensation for a low, mid, and high level displacement. (d) : Amount of compensation versus frequency associated with (c), bandwidth cropped to 10 Hz - 1000 Hz.

into the system, which negatively affects the average above 1000 Hz due to the large number of frequency points. The feedback noise is from the measurement and the optimisation noise may be from the stochastic gradient descent changing the parameter values at each time step. Even if overall the average compensation is slightly worse compared to the pure feed forward model, there is less error on the fundamental response around the resonance frequency, and below 200 Hz the compensation is slightly more effective than the pure feed forward algorithm as shown in Figure 3.13.

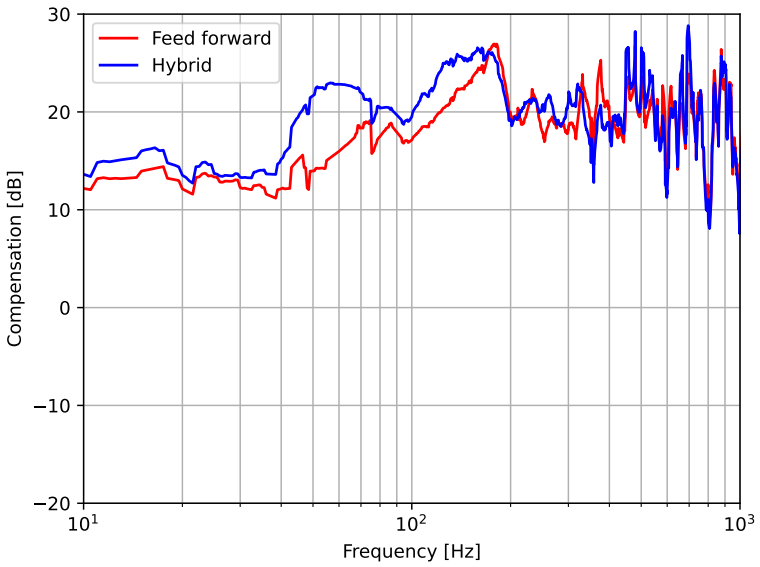


FIGURE 3.13 – Compensation versus frequency for the high level displacement level. Red curve represents pure feed forward compensation, while blue indicates the hybrid algorithm using error correction and real time optimisation.

### Conclusion

Overall, the compensation system works. The algorithm is capable of correcting both the fundamental response as well as providing an average of 12 dB of distortion reduction between 10 Hz and 4000 Hz, and up to 25 dB below 1000 Hz. This amount of compensation suggests that the model error is somewhere around 8% (Section 3.2.3).

The use of error correction and gradient descent is an interesting addition if the aim is to reduce the amount of distortion present around the resonance frequency, however it does induce extra complications and requirements when designing the associated hardware. The total system latency needs to be low or the loop stability will be compromised, and the gradient descent method needs to be kept simple. It is also possible that noise will be reinjected into the system by the feedback and therefore care must be taken when designing the analog signal conditioning and ADCs.

Of course, it is also possible that the linear and nonlinear distortion induced by the modelling error will be completely inaudible due to the presence of room modes and other sources outside of the loudspeaker.

Finally, most linearisation schemes use parameters tailored to the sample under study, something that is incredibly difficult in an industrial setting. Here we have proved it is possible to reduce the distortion of a loudspeaker system by up to 25 dB while also modifying the fundamental frequency response to match a predefined target.

### 3.3.2 Comparison with voltage driven loudspeaker

As most loudspeaker systems on the market are designed around voltage amplifiers, it is important to compare the control system against the current standard, a loudspeaker driven by a voltage source without any compensation. To this end, the stimulus is applied to the loudspeaker system using the same voltage amplifier as used for the transconductance amplifier system. Figure 3.14 illustrates this comparison at three peak displacement levels. Here the hybrid algorithm is used to linearise the loudspeaker system via the transconductance amplifier.

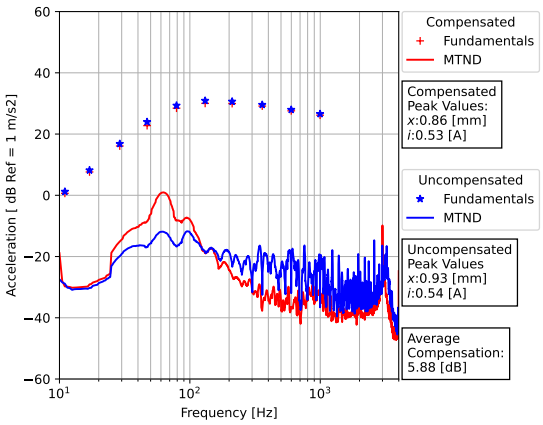


(a) With and without compensation for low peak displacement level.

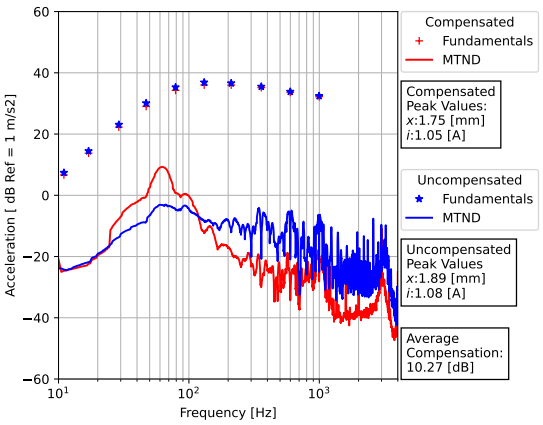


(b) With and without compensation for mid peak displacement level.

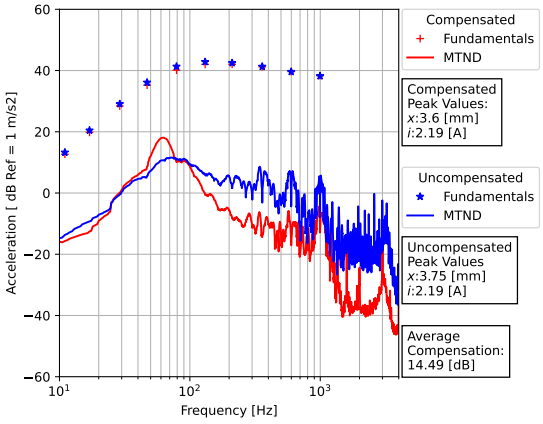


(c) With and without compensation for high peak displacement level.

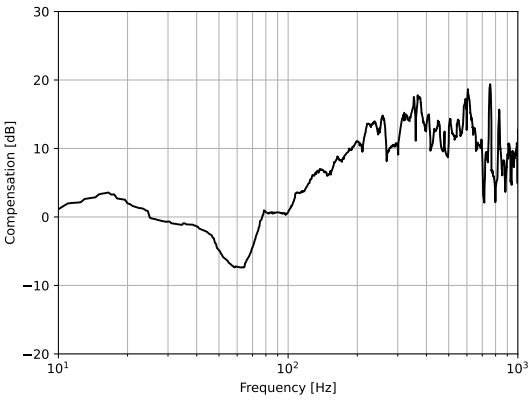


(d) Compensation versus frequency associated with Figure 3.14c, bandwidth cropped to 10 Hz - 1000 Hz.

FIGURE 3.14 – Compensation using error correction and gradient descent compared against an uncompensated voltage driven loudspeaker. Red indicates data with compensation, blue is without. The continuous curves show the MTND, whereas the + and ∗ show the fundamental frequencies. (a), (b), (c) : With/without compensation for a low, mid, and high level displacement. (d) : Amount of compensation versus frequency associated with (c), bandwidth cropped to 10 Hz - 1000 Hz.

### Comparison with voltage drive & shorting ring

Another question asked is : is it possible to attain the same levels of performance as the compensated system with simpler and cheaper means ? The Faital Pro 5FE100 has an almost identical twin product, the 5FE120. The difference is due to the presence of an aluminium shorting ring inserted into the motor. The 5FE120 is placed inside the loudspeaker enclosure and excited with a voltage source, and the results compared against the compensated system. Figure 3.15 illustrates this comparison at three peak displacement levels. Here the hybrid algorithm is used to linearise the loudspeaker system via the transconductance amplifier.

### Conclusion

Overall, the compensation algorithm still provides a useful amount of compensation above 100 Hz, with a reduction of up to 15 dB in the vocal frequency band when compared against the voltage driven drive unit and up to 10 dB when compared against a voltage driven drive unit with a shorting ring. The compensated system also shows a substantial reduction in distortion above 1000 Hz compared to the voltage driven systems, which is thought to be due to a combination of the high output impedance of the transconductance amplifier and the compensation algorithm. The distortion peak at resonance may be an issue for measurements, however the audibility of the distortion at this frequency may be very low due to frequency masking and the sensitivity of the ear to low frequency tones. In some cases, the extra distortion generated at the resonance frequency may give the impression of more bass, similar to the techniques which use the harmonics to create a 'ghost fundamental' [6, 87].
However it is important to remember that even if the compensation algorithm performs better, it requires a large amount of extra time, money, and silicon which adds additional challenges due to the global chip shortage. Of course if the silicon is already budgeted for in the product bill of materials then the addition of the algorithm into a product may become more cost effective.

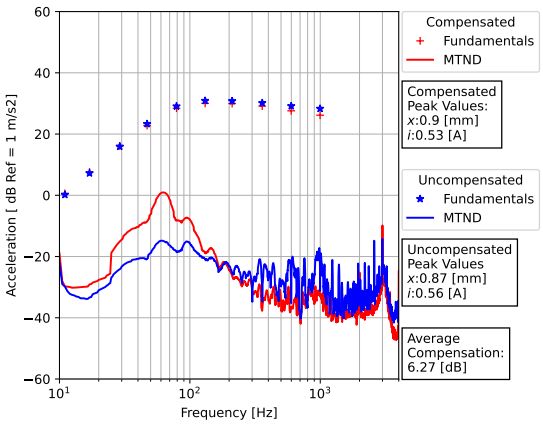


(a) With and without compensation for low peak displacement level.

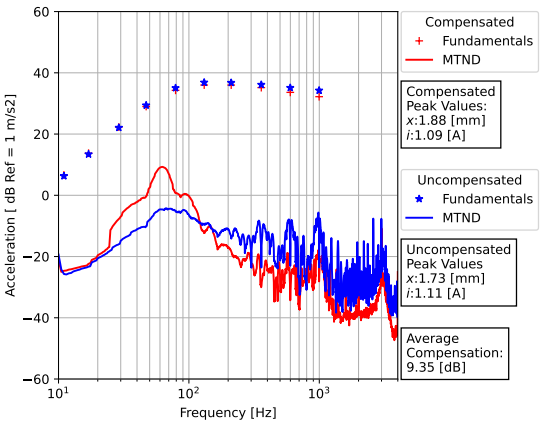


(b) With and without compensation for mid peak displacement level.

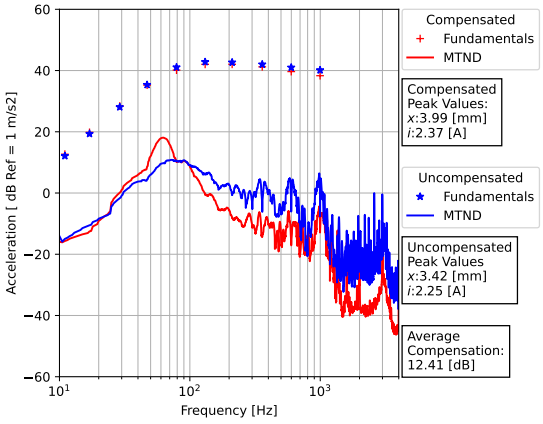


(c) With and without compensation for high peak displacement level.

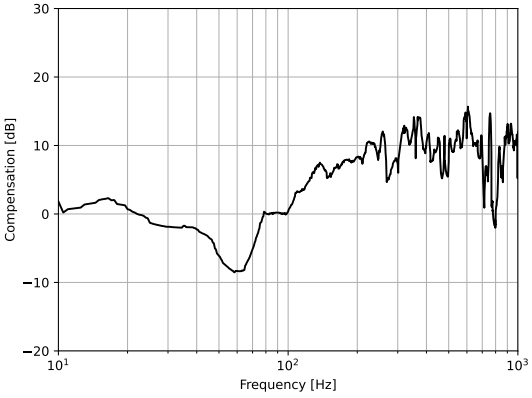


(d) Compensation versus frequency associated with Figure 3.15c, bandwidth cropped to 10 Hz - 1000 Hz.

FIGURE 3.15 – Compensation using error correction and gradient descent compared against an uncompensated voltage driven loudspeaker with a shorting ring. Red indicates data with compensation, blue is without. The continuous curves show the MTND, whereas the + and ∗ show the fundamental frequencies. (a), (b), (c) : With/without compensation for a low, mid, and high level displacement. (d) : Amount of compensation versus frequency associated with (c), bandwidth cropped to 10 Hz - 1000 Hz.

### 3.3.3 Compensation using voltage drive

This final section aims to show the results of using a voltage source to apply the compensation. The algorithm is modified to output a signal proportional to the compensation voltage rather than the compensation current by adding the line

$$u_{comp} = R_e i_{comp} + L_e(x_T)\frac{di_{lin}}{dt} + R_2(x_T)(i_{comp} - i_{L_2}) + R_3(x_T)(i_{comp} - i_{L_3}) + B\ell(x_T)v_T, \quad (3.6)$$

and the measured coil current is used rather than the coil voltage to generate the velocity error for the error correction and optimisation. The model parameters and the algorithm are identical apart from the aforementioned modifications. Figure 3.16 shows the results when using the hybrid method with a voltage source to apply the correction.

There are several interesting points that can be observed here. The first is that above 1000 Hz, the distortion levels are identical. This confirms the idea that the substantial decrease in distortion above 1000 Hz when using a transconductance amplifier to apply the correction signal is due to the higher output impedance. A deeper analysis may establish a link with electromagnetic hysteresis, and the fact it is not taken into account. The second point is that the correction is not as effective above 200 Hz when applied using a voltage source. This may be due to the extra modelling errors that occur when converting the compensation current to a compensation voltage in Equation (3.6).

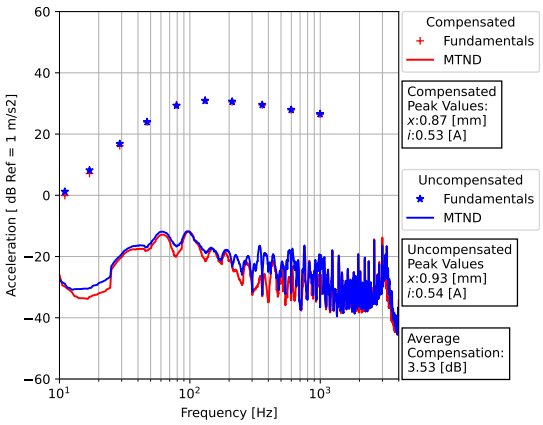


(a) With and without compensation for alow peak displacement level.

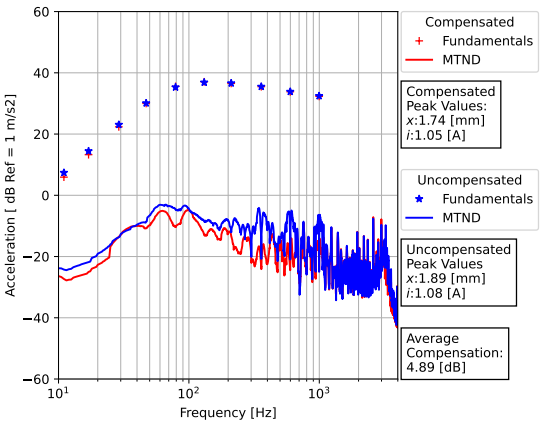


(b) With and without compensation for a medium peak displacement level.

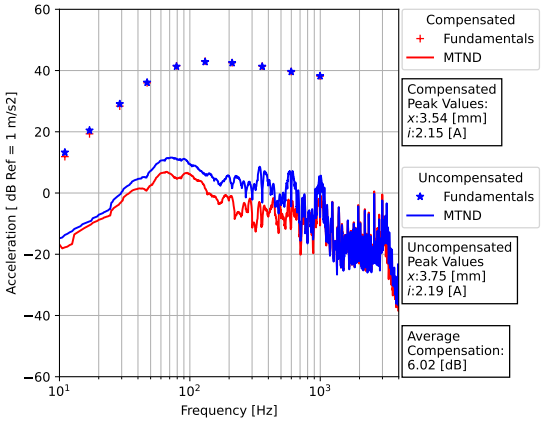


(c) With and without compensation for a high peak displacement level.

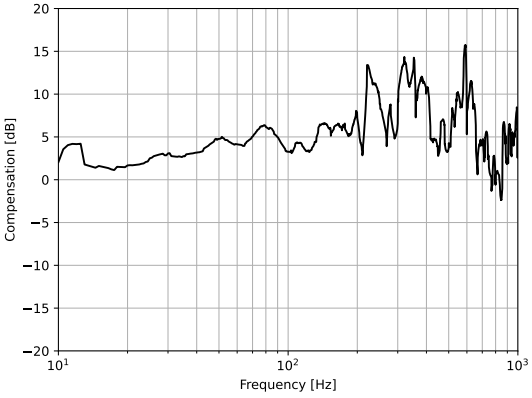


(d) Compensation versus frequency associated with Figure 3.16c, bandwidth cropped to 10 Hz - 1000 Hz.

FIGURE 3.16 – Voltage driven compensation using error correction and gradient descent compared against an uncompensated voltage driven loudspeaker. Red indicates data with compensation, blue is without. The continuous curves show the MTND, whereas the + and $*$ show the fundamental frequencies. (a), (b), (c) : With/without compensation for a low, mid, and high level displacement. (d) : Amount of compensation versus frequency associated with (c), bandwidth cropped to 10 Hz - 1000 Hz.

Chapitre 4

# Conclusion

## 4.1 Conclusion

This thesis concentrates on the issue of real time control of a loudspeaker system with the aim of providing both hardware and software solutions to the problem. The proposed solution combines both feed forward and feedback techniques, resulting in a hybrid control algorithm that also includes a real time optimisation of the loudspeaker suspension model based on the drive unit terminal voltage.

The feed forward model is a physics based nonlinear model represented by a system of nonlinear differential equations, whose parameters are provided using both simulations and data sheet information. An algorithm was developed during this thesis that allows the approximation of the roots of a implicit nonlinear quadratic equation, (that of the reluctance force), and published in [72]. In order to adapt the algorithm to production tolerances and time variations of the suspension, the nonlinear suspension model parameters are updated in real time using a simple gradient descent method.

A form of error correction feedback is combined with the gradient descent method in order to reduce the influence of modelling errors. The drive unit coil velocity is approximated from the drive unit terminal voltage and used as the feedback variable and also used to generate the cost function of the gradient descent method.

The algorithm is run on a controller designed during this thesis. The controller consists of a Teensy 3.6 micro controller that was used to run the algorithm in real time, along with a 16 bit SPI DAC for outputting the compensation signal. The Teensy 3.6 ADCs are of the SAR type leading to a low total system time delay of 72 µs. Care was taken when laying out the components in order to reduce the amount of noise present at the ADC inputs.

Various hardware tools were developed in order to provide clean measurement data and useful insight into certain nonlinear phenomena of the loudspeaker. One of the most important being a jig that allows the simultaneous measurement of the voice coil current,

voltage and applied force while fixed at a certain position inside the magnetic gap of the motor. The choice of materials and geometry allows these measurements to be performed without any mechanical resonances between 0 Hz and 1000 Hz.

The linearisation system was proved to provide up to 25 dB of distortion reduction between 10 Hz and 1000 Hz, while also correcting the fundamental response. A useful point for industrial applications is that the parameters for the nonlinear model were all derived from simulations or data sheets.

While the use of an amplifier with a high output impedance simplifies the model, it resulted in a compensation scheme that was more sensitive to model errors, specifically around the resonance frequency. However it was also shown that applying the correction signal using an amplifier with a high output impedance resulted in a more efficient correction above the resonance frequency and especially above 1000 Hz. When compared against a non compensated voltage driven loudspeaker system with a drive unit including a aluminium shorting ring, the current driven compensation scheme was found to still provide up to 10 dB of compensation between 200 Hz and 1000 Hz. Of course, an aluminium ring is simple to manufacture and relatively cheap compared to the added complexity of a low latency real time controller and current drive power amplifier. The additional challenges incurred by the global chip shortage are also to be taken into account.

The work done during this thesis provides several things that will be useful for future works :

- low latency controller for nonlinear system control or audio processing,
- an algorithm for the compensation of the reluctance force that also works with hysteretic models,
- an algorithm structure combining feed forward, error correction and gradient descent,
- a jig allowing the measurement of the voice coil behaviour when fixed at a certain position inside the magnetic gap,
- proof that it is possible to linearise a loudspeaker system using model parameters derived from simulations and data sheets.

## 4.2 Future Work

There are several paths that may be taken from this point. They will be listed here along with some ideas.

### Nonlinear Model

The accuracy of the nonlinear model is one aspect that needs improving. There is a plethora of scientific contributions detailing more accurate models for almost every component of the loudspeaker. Unfortunately, they are relatively complex and/or only concentrate on the modelling of the fundamental.
A more accurate model of the suspension is required, with the caveat that it must also be mathematically simple to execute and with parameters that are easy to fit. It is possible that a hysteretic type model may provide a more accurate prediction of the suspension behaviour.

### Sensors

A linear, low cost velocity sensor would improve the compensation performance considerably. If it could also be combined with a displacement sensor then the long term performance of the compensation scheme would be taken care of.

### Damping

The use of a current source amplifier to provide the compensation may still work if a way is found to add a set amount of linear mechanical loss to the system. It is possible that this may be performed using eddy currents and electromagnetic damping.

### Drive unit design

This thesis has concentrated on trying to compensate a drive unit that was specifically designed for voltage drive. It may be possible to improve the compensation results by using a drive unit designed to be driven by a current source and used with the compensation algorithm. For instance, lowering the suspension stiffness and using the air spring of the enclosure to provide the restoring force may reduce the influence of modelling errors as the air spring is linear, easy to predict and model, and does not vary with time. Reducing the value of the DC resistance of coil would lessen the thermal effects as the power dissipation would be lower, and the coil current is already controlled by the amplifier.

Annexe A

# Appendix - Eddy Currents & Mutual Inductance

## A.1 Eddy Currents & Mutual Inductance

### A.1.1 Eddy currents

Currents will be induced into any conductor subjected to a time varying magnetic field, thus the current flowing through the voice coil will induce current into any conductor in the vicinity. The material commonly used in the motor structure of a loudspeaker drive unit is a low carbon steel typically between 0.06% an 0.1 % carbon. Although its electrical conductivity is low, the close proximity to the source of the time varying magnetic field means that electrical currents will be induced. The material will have a direct influence on the emf of the coil.

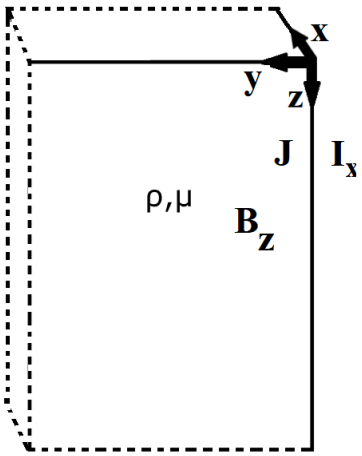


Figure A.1 – Ideal block of material

For a surface current $\overrightarrow{\mathbf{I}_x}$ in a material of electrical resistivity $\rho$ and magnetic permeability $\mu$, a magnetic field $\overrightarrow{\mathbf{B}_z}$ will be induced. By applying Maxwell's equations to this ideal case, we can observe how the eddy currents affect the system.

The Maxwell-Ampere law states that

$$\nabla \times \overrightarrow{\mathbf{B}} = \mu \overrightarrow{\mathbf{J}} + \mu\epsilon \frac{d\overrightarrow{\mathbf{E}}}{dt}, \tag{A.1}$$

combining with Ohm's law

$$\nabla \times \overrightarrow{\mathbf{B}} = \mu \overrightarrow{\mathbf{J}} + \mu\epsilon\rho \frac{d\overrightarrow{\mathbf{J}}}{dt}, \tag{A.2}$$

the time derivative term may be neglected if $\rho$, $\mu$ and $\epsilon$ are small

$$\nabla \times \overrightarrow{\mathbf{B}} \approx \mu \overrightarrow{\mathbf{J}}. \tag{A.3}$$

Combining Faraday's law and Ohm's law we get

$$\rho\nabla \times \overrightarrow{\mathbf{J}} = -\frac{\partial\overrightarrow{\mathbf{B}}}{\partial t}. \tag{A.4}$$

If we now look at the vectors for the current **I**, current density **J** and the magnetic field **B** defined as

$$\begin{aligned} \overrightarrow{\mathbf{I}} &= I_x \overrightarrow{x} + I_y \overrightarrow{y} + I_z \overrightarrow{z} \\ \overrightarrow{\mathbf{J}} &= J_x \overrightarrow{x} + J_y \overrightarrow{y} + J_z \overrightarrow{z} \\ \overrightarrow{\mathbf{B}} &= B_x \overrightarrow{x} + B_y \overrightarrow{y} + B_z \overrightarrow{z} \end{aligned} \tag{A.5}$$

Due to the construction of the example, we can simplify to

$$\begin{aligned} \overrightarrow{\mathbf{I}} &= I_x \overrightarrow{x} \\ \overrightarrow{\mathbf{J}} &= J_x \overrightarrow{x} \\ \overrightarrow{\mathbf{B}} &= B_z \overrightarrow{z}. \end{aligned} \tag{A.6}$$

Thus, Equations (A.3) and (A.4) may be written

$$\frac{\partial B_z}{\partial y}\overrightarrow{x} - \frac{\partial B_z}{\partial x}\overrightarrow{y} \approx \mu J_x \overrightarrow{x}, \tag{A.7}$$

and

$$\rho\left[-\frac{\partial J_x}{\partial z}\overrightarrow{y} + \frac{\partial J_x}{\partial y}\overrightarrow{z}\right] = -\frac{\partial B_z}{\partial t}\overrightarrow{z}. \tag{A.8}$$

Again due to the nature of the example, we may simplify

$$-\frac{\partial B_z}{\partial y}\overrightarrow{x} \approx \mu J_x \overrightarrow{x}, \tag{A.9}$$

and

$$\rho \frac{\partial J_x}{\partial y} \overrightarrow{z} = -\frac{\partial B_z}{\partial t} \overrightarrow{z}. \tag{A.10}$$

Finally

$$\begin{aligned} -\frac{\partial B_z}{\partial y} &\approx \mu J_x \\ \rho \frac{\partial J_x}{\partial y} &= -\frac{\partial B_z}{\partial t}, \end{aligned} \tag{A.11}$$

leading to

$$\frac{\partial^2 B_z}{\partial y^2} = \frac{\mu}{\rho} \frac{\partial B_z}{\partial t} \tag{A.12}$$

or

$$\frac{\partial^2 J_x}{\partial y^2} = \frac{\mu}{\rho} \frac{\partial J_x}{\partial t}. \tag{A.13}$$

From Equation (A.11), we can see that the spatial gradient of the the current density **J** along the $y$ axis is proportional to the time variation of the magnetic field **B**. This implies that for high frequency variations in **B** there will be a large gradient in current density **J** in the $y$ direction, but for low frequency variations in **B**, the current density **J** will be almost uniform in the $y$ direction. We may also observe that the signs of the current density **J** and the B field are opposed, thus confirming that the induced currents oppose the field that created them. We will now look at how the spatial gradient of the current density changes with frequency.

Equations (A.12) and (A.13) are both of the form of a diffusion equation which is well known and solutions exist. If we now suppose that our surface current is sinusoidal

$$I(t) = I_0 sin(\omega t), \tag{A.14}$$

then as we are under the assumption that the medium is linear and time invariant, the current density must also be sinusoidal but due to the diffusion equation, it must also have a phase that depends on y leading to a solution of the form

$$e^{j(\omega t - ky)}, \tag{A.15}$$

which combined with Equation (A.13) leads to the condition

$$j^2 k^2 = \frac{\mu}{\rho} j\omega, \tag{A.16}$$

leading to two solutions for the wave number k

$$\begin{cases} k_1 = +\left(\frac{\mu\omega}{\rho}\right)^{0.5} \frac{1-j}{\sqrt{2}} \\ k_2 = -\left(\frac{\mu\omega}{\rho}\right)^{0.5} \frac{1-j}{\sqrt{2}}. \end{cases} \tag{A.17}$$

Only $k_1$ is valid as the wave can only be attenuated by the medium, thus we may write the solution for the current density $J_x(t)$

$$J_x(t) = J_0 e^{-\frac{y}{\delta}} e^{j(\omega t - \frac{y}{\delta})}, \tag{A.18}$$

where $\delta$ is the skin depth of the medium

$$\delta = \sqrt{\frac{2\rho}{\mu\omega}}. \tag{A.19}$$

As both $B_z(t)$ and $J_x(t)$ are solutions to the diffusion equation, we may also write

$$B_z(t) = B_0 e^{-\frac{y}{\delta}} e^{j(\omega t - \frac{y}{\delta})}, \tag{A.20}$$

From Equation (A.18) we may observe how the current density changes with depth. $J_x(t)$ is maximal at the surface, with an amplitude that decays exponentially with propagation depth. As well as an amplitude change, there is also a phase change with depth. The phase starts of at 0 radians at the surface and then at a depth of $\pi\delta$ becomes $\pi$, implying that the current circulating at a depth of $y = \pi\delta$ is in phase opposition to the current circulating at the surface. If we now integrate the current density $J_x(t)$ over all of $y$, we end up with a quantity called the bulk current, in Amperes per $\overrightarrow{\mathbf{z}}$ unit width

$$I_{bulk}(t) = \int_0^\infty J_x(t) dy \tag{A.21}$$

which leads to

$$I_{bulk}(t) = \left[ -\frac{J_0 e^{-\frac{y}{\delta}} e^{j(\omega t - \frac{y}{\delta})}}{\frac{1}{\delta} + \frac{j}{\delta}} \right]_0^\infty, \tag{A.22}$$

thus

$$I_{bulk}(t) = \left[ \frac{J_0 \delta e^{j(\omega t)}}{1+j} \right], \tag{A.23}$$

finally

$$I_{bulk}(t) = \frac{J_0 \delta e^{j(\omega t - \frac{\pi}{4})}}{\sqrt{2}}. \tag{A.24}$$

Using the same logic, we may also derive the expression for the bulk magnetic field $B_{bulk}$ in Teslas per $\overrightarrow{\mathbf{x}}$ unit length

$$B_{bulk}(t) = \frac{B_0 \delta e^{j(\omega t - \frac{\pi}{4})}}{\sqrt{2}}. \tag{A.25}$$

The bulk current is equivalent to the total current flowing inside the medium, but with a uniform current density. From this point of view, one can imagine the bulk current as the current flowing uniformly through a rectangular portion of the block of material. The bulk field $B_{bulk}$ is the equivalent magnetic field created by this bulk current. This current path will have its own resistance and inductance. From the Maxwell-Faraday equation

$$\oint E \cdot dl = -\int \frac{\partial B}{\partial t} \cdot dA, \tag{A.26}$$

becomes in our case

$$\oint E dx = -\int_0^\infty \int_0^{\hat{x}} \frac{\partial B}{\partial t} dy dx, \tag{A.27}$$

where $\hat{x}$ is the unit length in the $\overrightarrow{x}$ direction. Using equation (A.11)

$$\oint E dx = \rho \int_0^\infty \int_0^{\hat{x}} \frac{\partial J_x}{\partial y} dy dx, \tag{A.28}$$

thus

$$\oint E dx = -(1+j)\frac{\rho}{\delta} \int_0^\infty \int_0^{\hat{x}} J_0 e^{-\frac{y}{\delta}} e^{j(\omega t - \frac{y}{\delta})} dy dx, \tag{A.29}$$

or

$$\oint E dx = -(1+j)\frac{\rho}{\delta}\hat{x} \int_0^\infty J_0 e^{-\frac{y}{\delta}} e^{j(\omega t - \frac{y}{\delta})} dy, \tag{A.30}$$

of which the integral has already been calculated for the bulk current in Equation (A.24), giving

$$\oint E dx = -(1+j)\frac{\rho}{\delta}\hat{x}\frac{J_0 \delta e^{j(\omega t - \frac{\pi}{4})}}{\sqrt{2}}. \tag{A.31}$$

or

$$E\hat{x} = -\frac{\rho}{\delta}\hat{x}\frac{J_0 \delta e^{j(\omega t - \frac{\pi}{4})}}{\sqrt{2}} + e^{-\frac{\pi}{2}}\frac{\rho}{\delta}\hat{x}\frac{J_0 \delta e^{j(\omega t - \frac{\pi}{4})}}{\sqrt{2}} \tag{A.32}$$

There are two terms here, one term is in phase with the bulk current implying losses, while one term is $\frac{\pi}{2}$ out of phase with the bulk current implying an inductive component

$$\begin{cases} E_r\hat{x} = -\frac{\rho}{\delta}\hat{x}\frac{J_0 \delta e^{j(\omega t - \frac{\pi}{4})}}{\sqrt{2}} \\ E_{ind}\hat{x} = \frac{\rho}{\delta}\hat{x}\frac{J_0 \delta e^{j(\omega t - \frac{3\pi}{4})}}{\sqrt{2}}. \end{cases} \tag{A.33}$$

By using the assumption that $E_{ind} = L\frac{dI}{dt}$, we may write that

$$\begin{cases} R_{eddy} = \frac{\rho}{\delta} \\ L_{eddy} = \frac{\rho}{\delta\omega}, \end{cases} \tag{A.34}$$

or

$$\begin{cases} R_{eddy} = \sqrt{\frac{\mu\omega\rho}{2}} \\ L_{eddy} = \sqrt{\frac{\mu\rho}{2\omega}}. \end{cases} \tag{A.35}$$

We can see that both the resistance and inductance depend on the square root of frequency, electrical resistivity and permeability. Another point is that the resistance increases with the square root of frequency, while the inductance decreases with the square root of frequency. This is logic for as frequency increases, the area in which the current circulates is reduced due to the skin depth. This leads to an increase in electrical resistivity, and a decrease in inductance as the resulting magnetic fields are circulating inside a smaller and smaller amount of the medium.
It is the bulk current which experiences these two effects and as the bulk current can be approximated as a single conductive loop of uniform current density, we effectively have two concentric coils. The first coil is the voice coil and the second coil is the equivalent current path of the bulk current.

### A.1.2 Mutual Inductances

If we imagine our two coils as in Figure A.2, concentric, parallel and separated by the distance r. We know that the emf across coil 1 can be expressed as

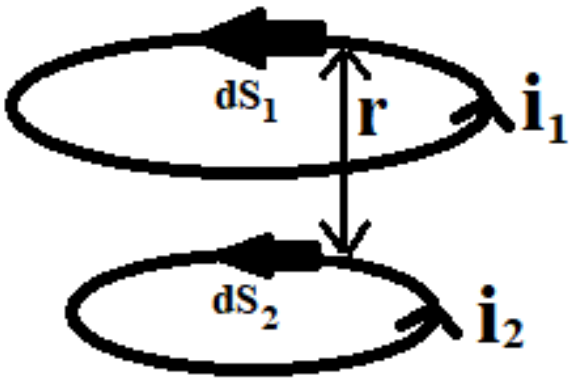


FIGURE A.2 – Mutual inductance of two coils

$$\epsilon_1 = -\frac{d}{dt}\int \vec{\mathbf{B}} \cdot \vec{\mathbf{dS}}, \tag{A.36}$$

where $S$ is the surface bound by the coil. This expression may also be expressed as a line integral of the vector potential A around coil 1

$$\epsilon_1 = -\frac{d}{dt}\oint_1 \overrightarrow{\mathbf{A}} \cdot \overrightarrow{\mathbf{dS_1}}. \tag{A.37}$$

Of course, what interests us is the coupling between the two coils, thus we assume that the vector potential in coil 1 is due to currents in coil 2

$$\overrightarrow{\mathbf{A}} = \frac{1}{4\pi\epsilon_0 c^2}\oint_2 \frac{i_2 \overrightarrow{\mathbf{dS_2}}}{r}, \tag{A.38}$$

where $c$ is the speed of light, $i_2$ is the current circulating in coil 2 and $r$ is the distance between the two coils. Therefore, the emf in coil 1 will be

$$\epsilon_1 = -\frac{1}{4\pi\epsilon_0 c^2}\frac{d}{dt}\oint_1\oint_2 \frac{i_2 \overrightarrow{\mathbf{dS_2}}}{r} \cdot \overrightarrow{\mathbf{dS_1}}. \tag{A.39}$$

The current $i_2$ does not depend on the integration variables, therefore it may be removed leaving us with

$$\epsilon_1 = -\left[\frac{1}{4\pi\epsilon_0 c^2}\oint_1\oint_2 \frac{\overrightarrow{\mathbf{dS_2}} \cdot \overrightarrow{\mathbf{dS_1}}}{r}\right]\frac{di_2}{dt}, \tag{A.40}$$

as we assume that both coils are concentric and parallel

$$\epsilon_1 = -\left[\frac{1}{4\pi\epsilon_0 c^2 r}\oint_1\oint_2 dS_2 dS_1\right]\frac{di_2}{dt}, \tag{A.41}$$

or

$$\begin{cases} \epsilon_1 = -\Pi\frac{di_2}{dt} \\ \Pi = \left[\frac{1}{4\pi\epsilon_0 c^2 r}\oint_1\oint_2 dS_2 dS_1\right] \end{cases} \tag{A.42}$$

The term $\Pi$ is what is commonly know as the mutual inductance. We can see that it decreases as the coils are moved further apart ($r$), and that due to the dot product in Equation (A.39), tends towards zero as the coils become perpendicular. As $dS_1$ and $dS_2$ are line integrals over the length of their respective coils, the mutual inductance will increase with the length of the wire, or the amount of turns in the coils.

The consequence is that our voice coil will have several sources of emf. Assuming that the coil is immobile inside the motor, we will have the emf due to self inductance as well as the emf due to mutual inductance

$$\epsilon = L_{self}\frac{di_1}{dt} - \Pi\frac{di_2}{dt}, \tag{A.43}$$

where $L_{self}$ is the self inductance of the voice coil, $\Pi$ represents the mutual inductance due to the coupling with the surrounding steel and $i_2$ is the bulk current circulating inside the

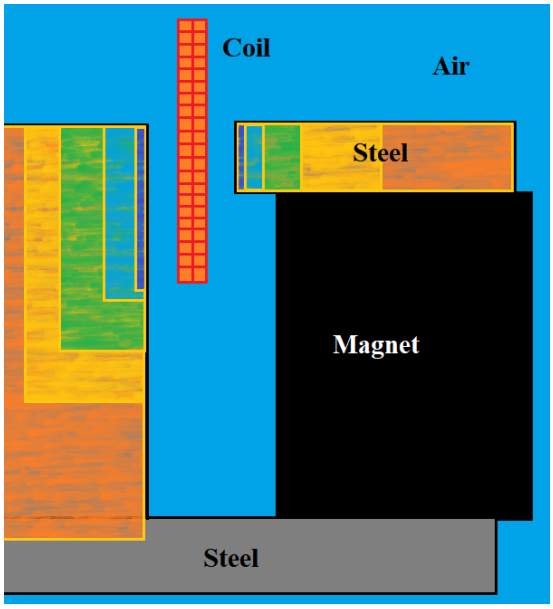


FIGURE A.3 – Illustration of inductive coupling and skin effect

surrounding steel. As the bulk current is effectively a coil with a single turn and a frequency dependent resistance and inductance, the emf due to the mutual coupling between the coils will also exhibit a frequency dependent resistance and inductance. Figure A.3 is an attempt to illustrate the phenomena. The self inductance of the voice coil will be due to the properties of the solid blue medium, air, and the amount of turns that enclose the 'air core'. The mutual inductance will be due to the coupling with the steel. The pastel type colours show the skin depth and thus the path of the bulk current as frequency increases, orange being low frequency and dark blue being high frequency.

# Appendix - Fractional Derivatives

## B.1 Fractional Derivatives

Fractional Calculus has been around for the last 300 years. It first appeared in 1695 in a letter from Gottfried Wilhelm Leibniz to Guillaume de l'Hôpitale. Interest in fractional calculus has increased dramatically of the last few years due to the fact that physical and biological phenomena often have memory. This is where integer order derivatives and integrals fail, as they are local.

There are several ways of calculating the fractional derivative or integral of a function $f(t)$. For this work, we will only be concentrating on the Grünwald Letnikov formulation as it can be represented by a weighted sum like an FIR filter. The fractional derivative of order $\alpha$ of a discretised function $f(nT_s)$ could be approximated by [39, 44]

$$\frac{d^\alpha f(t)}{dt^\alpha} \approx \frac{1}{T_s^\alpha} \sum_{i=0}^{n} (-1)^i \binom{\alpha}{i} f((n-i)T_s), \tag{B.1}$$

where $T_s$ is the sampling period and $n$ is the current sample number. The FIR filter structure may become more apparent if we rewrite the equation as a weighted sum of past samples

$$\begin{aligned} \frac{d^\alpha f(t)}{dt^\alpha} &\approx \frac{1}{T_s^\alpha} \sum_{i=0}^{n} w_i^\alpha f((n-i)T_s) \\ w_i^\alpha &= (-1)^i \binom{\alpha}{i}, \end{aligned} \tag{B.2}$$

where $w_i^\alpha$ represents the weights of the FIR filter which may be calculated in two ways. This first is the classical recurrence formulation

$$\begin{aligned} w_0^\alpha &= 1 \\ w_i^\alpha &= \left[1 - \frac{\alpha+1}{i}\right] w_{i-1}^\alpha. \end{aligned} \tag{B.3}$$

The second methods makes use of a FFT to compute a finite number of weights by considering the weights $w_i^\alpha$ as the coefficients of the power series expansion [39]

$$(1-z)^\alpha = \sum_{i=0}^{\infty}(-1)^i\binom{\alpha}{i}z^i = \sum_{i=0}^{\infty} w_i^\alpha z^i. \tag{B.4}$$

Substituting $z = e^{-j\theta}$

$$(1-e^{-j\theta})^\alpha = \sum_{i=0}^{\infty} w_i^\alpha e^{-ij\theta}, \tag{B.5}$$

then the weights are expressed in the form of a Fourier transform

$$\begin{aligned} w_i^\alpha &= \frac{1}{2\pi i}\int_0^{2\pi} f_\alpha(\theta)e^{ij\theta}d\theta \\ f_\alpha(\theta) &= (1-e^{-j\theta})^\alpha. \end{aligned} \tag{B.6}$$

Practically, this may be calculated using the following pseudo code

```
nPoints = 1024
theta = linspace(0, 2 pi, nPoints)
z = exp(-1i theta)
alpha = 0.5
f = (1 - z)^alpha
F = real(ifft(f))
nMemory = 512
w = F(1:nMemory)
```

where $nPoints$ represents the number of integration points (more is better), and $nMemory$ represents the length of the FIR filter. Using this method always results in a finite number of memory points and is very quick. Another advantage relative to the recurrence method is that the weights for higher order approximations to the fractional derivative may be easily calculated. The $(1-z)^\alpha$ is a first order approximation to the derivative, such that for an $\alpha$ of 1, the weights form the Euler definition of a derivative. Second and third order approximations [39] may be calculated using

$$\begin{aligned} f_2 &= \left(\frac{3}{2} - 2z + \frac{1}{2}z^2\right)^\alpha \\ f_3 &= \left(\frac{11}{6} - 3z + \frac{3}{2}z^2 - \frac{z^3}{3}\right)^\alpha. \end{aligned} \tag{B.7}$$

Annexe C

# Appendix - Numerical Integrator stability

## C.1 Stability

One of the main principles behind the solver is that the gradient of the function between two time steps is small. If the gradient is larger than a certain amount, then the solution will not converge and will become unstable. In practical terms, this may be observed easily by simply increasing the time step until the solution diverges.
In mathematical terms, the stability of a solver may be assessed using the test equation

$$\frac{dy}{dt} = \lambda y(t). \tag{C.1}$$

When discretised and applied to the Euler forward solver

$$y_{n+1} = y_n + T_s \lambda y_n, \tag{C.2}$$

leading to

$$y_{n+1} = y_n(1 + T_s \lambda). \tag{C.3}$$

We now define the stability function of the Euler forward method as

$$\begin{aligned} \Phi(z) &= (1 + z) \\ z &= T_s \lambda, \end{aligned} \tag{C.4}$$

and the stability criterion as $|\Phi(z)| < 1$, leading to a stability region of

$$z \in C,\ |1 + z| < 1. \tag{C.5}$$

One way $z$ can verify this condition is

$$-2 < z < 0. \tag{C.6}$$

In the case of the RL circuit example, $\lambda$ is simply

$$\lambda = -\frac{R}{L}. \tag{C.7}$$

Thus, when using the Euler methods to provide an approximation of the solution to the RL circuit equations, the time step must be small enough to verify

$$T_s < 2\frac{L}{R}. \tag{C.8}$$

If we now look at a higher order solver, such as the second order Adams Bashforth method

$$i[n+1] = i[n] + \frac{dt}{2}(3y(n, i_n) - y(n-1, i_{n-1})), \tag{C.9}$$

where the stability function is

$$\Phi(w, z) = w^2 - \frac{(2+3z)}{2}w + \frac{z}{2}, \tag{C.10}$$

which has roots

$$\begin{aligned} w_1 &= \frac{1}{2}\left[1 + \frac{3}{2}z + \sqrt{1 + z + \frac{9}{4}z^2}\right] \\ w_2 &= \frac{1}{2}\left[1 + \frac{3}{2}z - \sqrt{1 + z + \frac{9}{4}z^2}\right], \end{aligned} \tag{C.11}$$

leading to a stability region of

$$z \in C, \left| \frac{1}{2}\left[1 + \frac{3}{2}z \pm \sqrt{1 + z + \frac{9}{4}z^2}\right] \right| < 1. \tag{C.12}$$

One way z can verify this condition is

$$-1 < z < 0. \tag{C.13}$$

Thus the $2^{nd}$ order method has a smaller stability region than the $1^{st}$ order method. Generally, higher order methods are more accurate, but less stable.
When a system of equations is used, such as those of a single degree of freedom oscillator with a forcing term $f(t)$

$$f(t) = M\ddot{x}(t) + R\dot{x}(t) + Kx(t), \tag{C.14}$$

we must find the eigenvalues of the equation matrix A. The first step is to transform the equations into first order differential equations

$$\begin{aligned} \frac{dx}{dt} &= v \\ \frac{dx}{dt} &= \frac{f(t) - Rv - Kx}{M}. \end{aligned} \tag{C.15}$$

This can be written in matrix form,

$$\begin{bmatrix} \frac{dx}{dt} \\ \frac{dv}{dt} \end{bmatrix} = A \begin{bmatrix} x \\ v \end{bmatrix} + \frac{1}{M} \begin{bmatrix} 0 \\ f(t) \end{bmatrix}, \tag{C.16}$$

where

$$A = \begin{bmatrix} 0 & 1 \\ -\frac{K}{M} & -\frac{R}{M}. \end{bmatrix} \tag{C.17}$$

We now need to find the eigenvalues of A, or the values of $\lambda$ that verify

$$|A - I\lambda| = 0, \tag{C.18}$$

where $I$ is the identity matrix. An analytical development is rather time consuming, but there is another more intuitive way of looking at the stability. If we look at the A matrix in Equation (C.17), we can see that the gradient $\frac{dv}{dt}$ depends on fractions $\frac{-K}{M}$ and $\frac{R}{M}$. Therefore, the gradient of $v$ with respect to time increases as $M$ is decreased and $K$ and $R$ are increased. Physically this implies that mechanical systems with low mass and high stiffness require the use of a smaller time step to remain stable. The same logic may be applied to the example of the inductor, electrical systems with low inductance will require a smaller time step to converge.

Annexe D

# Appendix - Amplifier Prototype

## D.1 Introduction

The work described in this thesis revolves around the compensation of certain nonlinear phenomena of the electrodynamic loudspeaker. The compensation algorithm is of the discrete kind, and thus when the compensation signal has been converted into the digital domain, it needs to be applied as accurately as possible to the loudspeaker via a power amplifier. Power amplifiers exist in four main topologies, whose basic characteristics are summarised in Table D.1.

| | Ideal Amplifier Type | | | |
|---|---|---|---|---|
| | Voltage | Current | Transconductance | Transimpedance |
| Input Impedance | $\infty$ | 0 | $\infty$ | 0 |
| Output Impedance | 0 | $\infty$ | $\infty$ | 0 |
| Input | Volts | Amperes | Volts | Amperes |
| Output | Volts | Amperes | Amperes | Volts |
| Gain | V/V | A/A | A/V | V/A |

Table D.1 – Basic Amplifier Characteristics

The output of the compensation scheme is in the form of a voltage, thus only two options are available to use, a voltage amplifier or a transconductance amplifier. Another requirement is that the compensation applied to the loudspeaker is in the form of a current, using so called 'current drive'. Therefore the amplifier type needed to perform the correction is a transconductance amplifier.
Most of the power amplifiers available on the market today are of the voltage type, with a small percentage of the other types reserved for instrumentation, research or esoteric uses. It is therefore slightly challenging to obtain a transconductance amplifier that adheres to a specific set of requirements.
In the aim of providing a foundation for future works, this chapter details the design and construction of a transconductance amplifier system that may be adapted to specific tasks and made for a relatively small financial cost.

## D.2 Topologies

There are many different ways of designing an amplifier that produces an output current that is proportional to an input voltage. The simplest is where the load is inside the feedback loop, and the feedback is taken from a current sensing resistor [18, 32] as shown in figure D.1. There is however some issues with this circuit. Firstly the frequency dependent and nonlinear load of a loudspeaker will have a tendency to modulate the transconductance. Secondly, the output impedance of the amplifier will be frequency dependent due to the amplifiers dominant pole [67]. Thirdly, the load is not ground referenced.

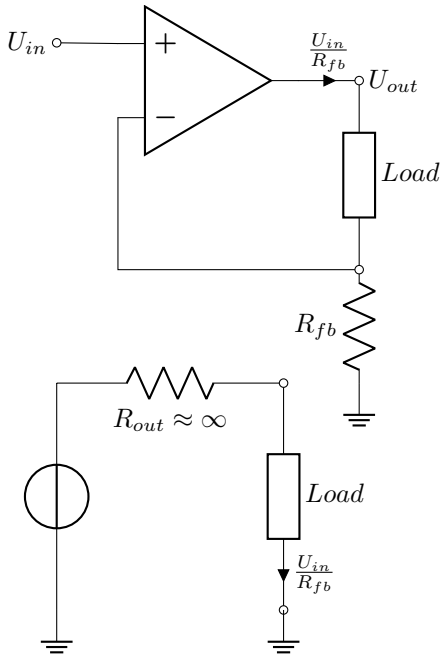


FIGURE D.1 – Transconductance amplifier.

A circuit shown in Figure D.2 is proposed in [67]. The overall current gain $G_i$ is defined by the resistors $R_x$ and $R_f$ as

$$G_i = -\frac{R_x}{R_f}. \tag{D.1}$$

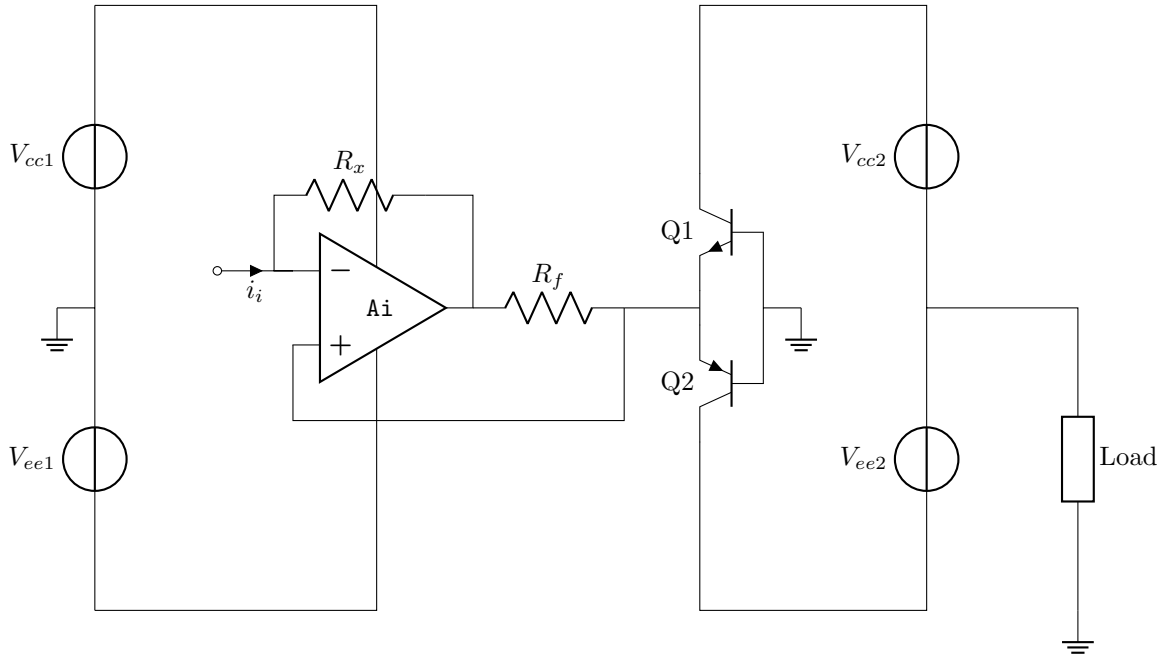


FIGURE D.2 – Basic Topology from [67].

$V_{cc1}$ and $V_{ee1}$ are both ground referenced power supplies, which means they may be used in other channels. The current flowing through the load is the current flowing through $R_f$ minus any base current flowing to ground in $Q_1$ and $Q_2$. The load is ground referenced and also outside of any feedback loop. Finally, as the amplifier $A_i$ is referenced to the input of the common base stage, any distortions appearing here are effectively decoupled. One of the main disadvantages compared to the circuit in Figure D.1 is the need for an extra power supply in $V_{cc2}$ and $V_{ee2}$.

The circuit detailed in [67] shows a level of performance that would be sufficient for the work done in this thesis. The main issue is the complexity of the circuit. There is a vast number of components, some of which may no longer be available due to being obsolete or no longer in stock due to the global chip shortage. Thus in the interest of proposing a simple solution that may be built using modern and available components, some modifications were made, as shown in Figure D.3.

The circuit proposed for this thesis is based around the "Module" part of Figure D.3. An operational amplifier A2 is used to keep the voltage at $v_{RF-}$ equal to the reference voltage of the voltage amplifier. The current circulating in $R_f$ and thus in the Load can be defined as

$$i_{Load} = \frac{v_{RF+} - v_{RF-}}{R_f}. \tag{D.2}$$

The main advantage of the proposed circuit compared to that of [67] is the drastically reduced component count. The module can be used to transform any commercially available voltage amplifier into a transconductance system, with low complexity and cost. Of course as the module acts as a sort of current follower, the linearity of the system will

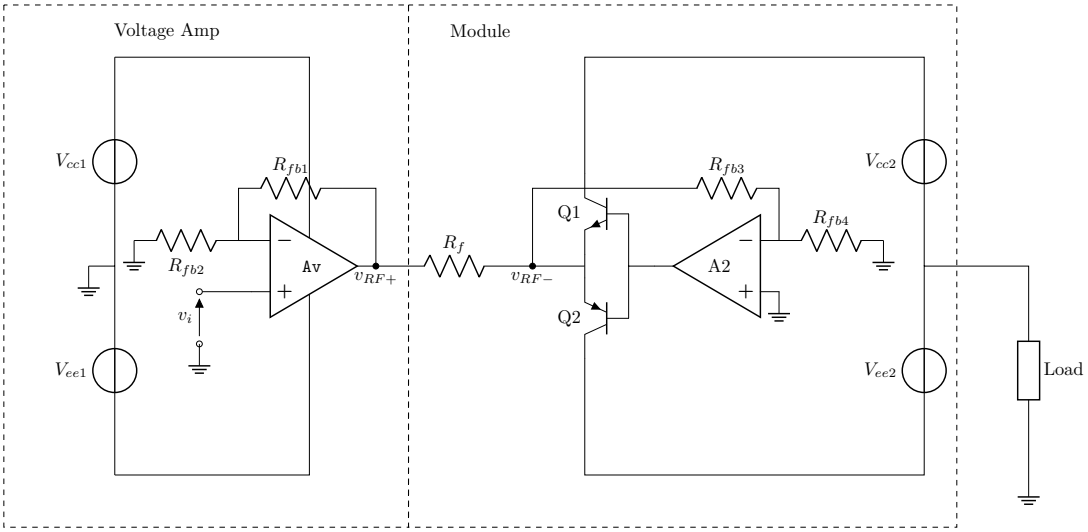


FIGURE D.3 – Proposed Topology.

depend on the linearity of the voltage amplifier.

## D.3 Prototype

A prototype amplifier (Figure D.4) was built around the topology in Figure D.3, and characterised as detailed in the next section. The actual circuit and component values are given in Section D.4, Figure D.6. Two BNC outputs provide load current and voltage monitoring.


(a) Prototype. (b) Amp front panel.

FIGURE D.4 – Amplifier Prototype.

### D.3.1 Amplifier Performance

It is important to characterise the performance of the completed circuits in terms of noise, distortion and frequency response, provide a comparison against a commercial amplifier (the BEAK BAA1000), and also analyse the influence of the Op Amp on the system performance.
To characterise the system, stimuli are generated in Python and a DT9837C data acquisition system is used to both apply the stimuli and measure the various quantities. The DT9837C is set to run at a sampling rate of 96 kHz, and the inputs DC coupled. The voltage amplifier used to stimulate the module is an Audiophonics LPA-S400ET which uses the Purifi 1ET400A amplifier modules [1]. The voltage gain of the amplifier is set to 10 V/V using the internal jumpers.

#### Frequency Response

In order to analyse the frequency response, an exponential sweep is applied to the controller inputs with the following specifications :

- Start Frequency : 0.01 Hz,
- end Frequency : 48000 Hz,
- amplitude : 0.5 $V_{peak}$,
- duration : 20 s.

As can be seen in Figure D.5f, the overall frequency response is a first order low pass filter, with a -3 dB frequency of 34 kHz. The total system transconductance is 3.4 A/V.

#### Noise, Distortion

To characterise the noise and distortion of the circuit, two types of stimuli are used, sine wave and multitone. For the sine wave, three different frequencies are used to characterise the system, whereas for the multitone ten simultaneous frequencies were used. The stimulus is generated in Python and applied to the voltage amplifier input with a DT9837C data acquisition system (DAQ). Both the amplifier output voltage and module output current signals are acquired using the DAQ and post processed in Python. For the sine wave analysis, a FFT is performed using a rectangular window over 4 seconds of data. The results are shown in Figures D.5a to D.5c. What is immediately clear is the system performance depends on the voltage amplifier. Any distortion and noise generated by the voltage amplifier will find its self in the current flowing through the load. If low noise and distortion is required, then care must be taken in selecting an appropriate voltage amplifier. For the multitone analysis, the FFT is performed over 2 seconds of data using a rectangular window, with the result illustrated in Figures D.5d and D.5e, the SINAD

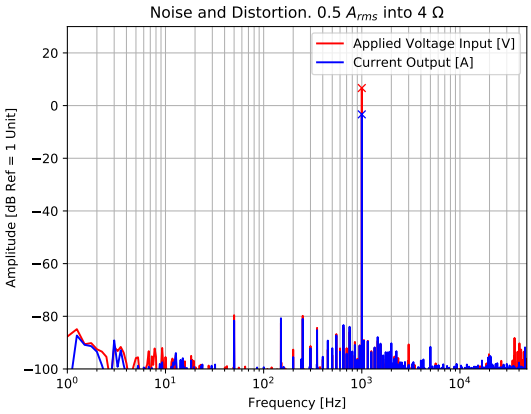


(a) Noise floor and Distortion, 1 W into 4 Ω.

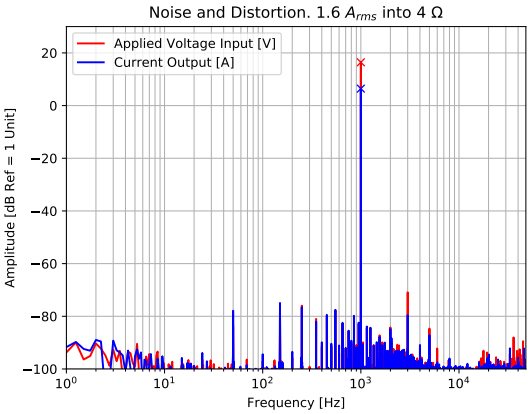


(b) Noise floor and Distortion, 10 W into 4 Ω.

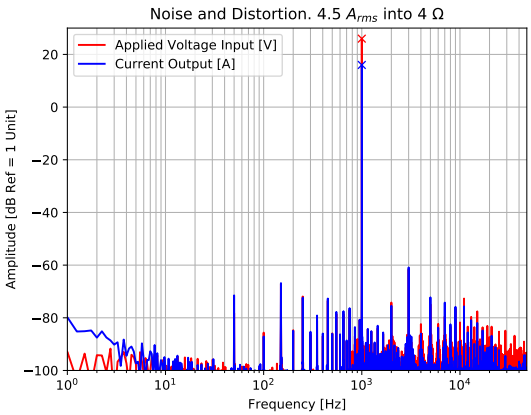


(c) Noise floor and Distortion, 80 W into 4 Ω.

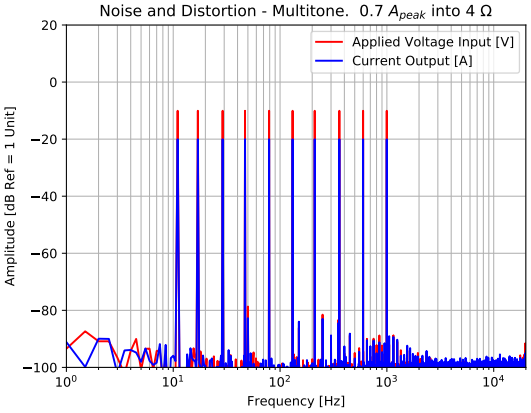


(d) Noise floor and Distortion with multitone, 0.7 $A_{peak}$ into 4 Ω.

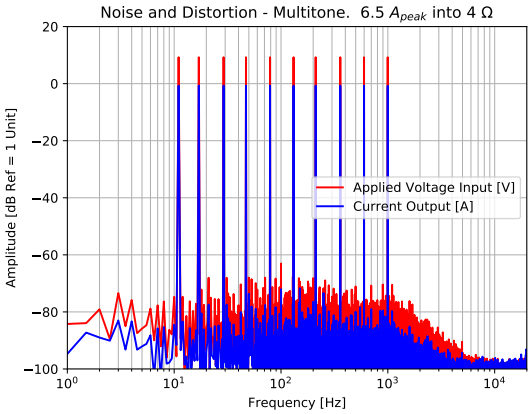


(e) Noise floor and Distortion with multitone, 6.5 $A_{peak}$ into 4 Ω.

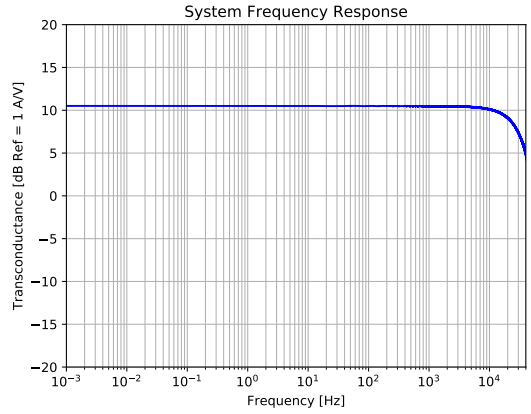


(f) Amplifier Frequency Response.

FIGURE D.5 – Amplifier Characteristics, 4 Ω resistive load. Red indicates the voltage applied to the input of the module by the voltage amplifier, and blue indicates the current output of the module. (a),(b),(c) : Noise floor and harmonic distortion for a 1 kHz sine wave input for 1 W, 10 W and 80 W. (d), (e) : Noise floor and distortion for a multitone signal at 0.7 $A_{peak}$ and 6.5 $A_{peak}$. (f) : Frequency response.

is approximately 59 dB for the 0.7 $A_{peak}$ signal and 61 dB for the 6.5 $A_{peak}$ signal. The transconductance amplifier system is thus the limiting factor in the linearity of the control system as the SINAD for the controller using the same signal and bandwidth is 76 dB. Table D.2 provides a summary of the amplifier system characteristics.

| Module Characteristics | | | |
|---|---|---|---|
| Parameter | Value | Unit | Notes |
| Output DC Offset | 0.85 | mA | Shorted input |
| Transconductance | 0.34 | A/V | @ 1 kHz |
| Input Impedance | 3.4 | Ω | @ 1 kHz |
| Output Impedance | 2.2 | kΩ | - |
| Bandwidth | 34 | kHz | -3dB |
| Input High Pass | - | Hz | DC Coupled |
| Input Low Pass | 34 | kHz | -3dB |

Table D.2 – Transconductance Power Amplifier Specifications

## D.4 Amplifier Module Circuit & Values

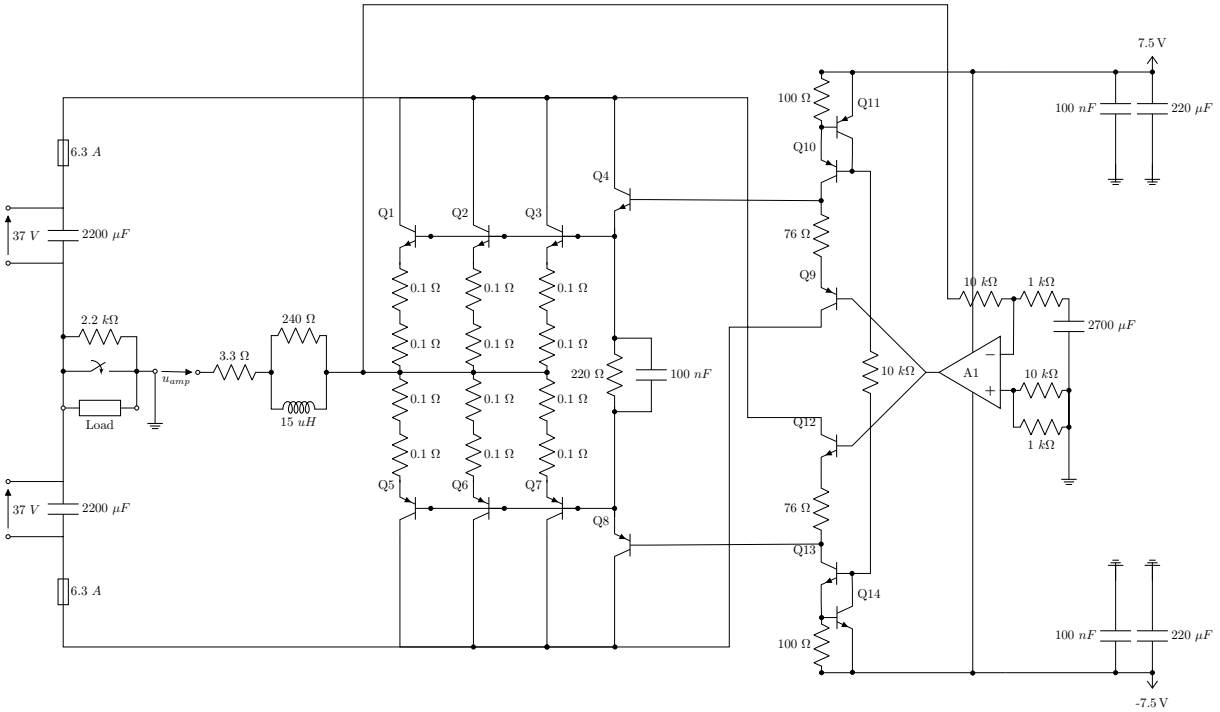


FIGURE D.6 – Amplifier Module Circuit with Values

— Q1-Q3 : MJL3281. Mounted on the heat sink
— Q5-Q7 : MJL1302. Mounted on the heat sink
— Q4 : MJE15034. Mounted on the heat sink
— Q8 : MJE15035. Mounted on the heat sink
— Q10, Q11 : BC560.
— Q13, Q14 : BC550.
— Q9 : KSA1381. Mounted on the heat sink
— Q12 : KSC3503. Mounted on the heat sink
— A1 : NE5534. (With 47 $pF$ compensation capacitor)

## D.5 Other data

In this section, two comparisons are performed. Figure D.7 illustrates the differences in performance when using two different Op Amps for A1, NE5534 versus the TL081. Figure D.8 compares the transconductance amplifier system designed during this thesis with a commercial amplifier, the BEAK BAA1000.

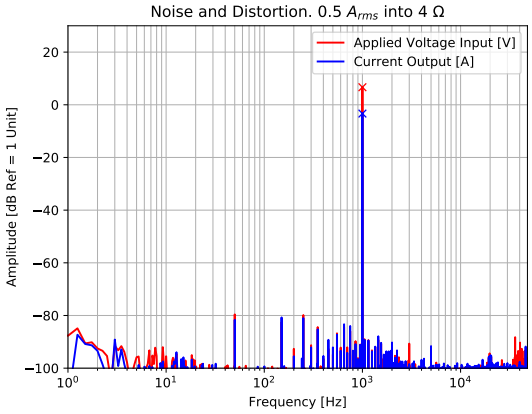


(a) Noise floor and Distortion, NE5534, 1 W into 4 Ω.

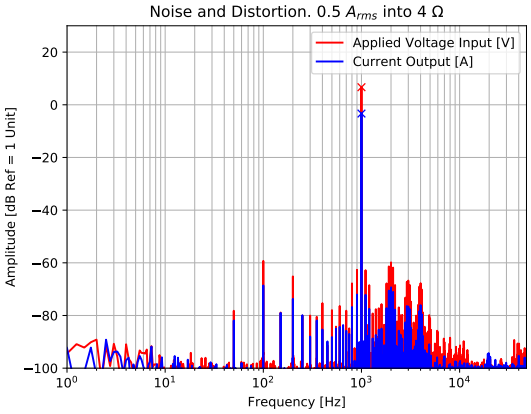


(b) Noise floor and Distortion, TL081, 1 W into 4 Ω.

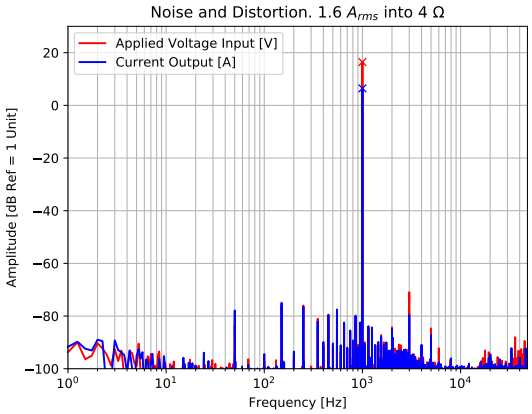


(c) Noise floor and Distortion, NE5534, 10 W into 4 Ω.

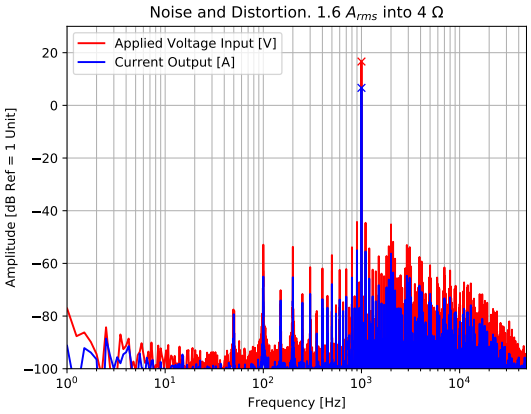


(d) Noise floor and Distortion, TL081, 10 W into 4 Ω.

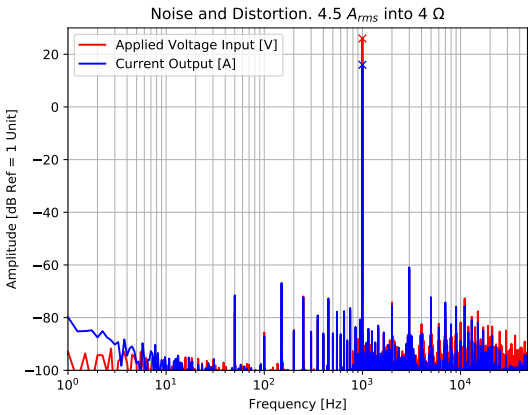


(e) Noise floor and Distortion, NE5534, 80 W into 4 Ω.

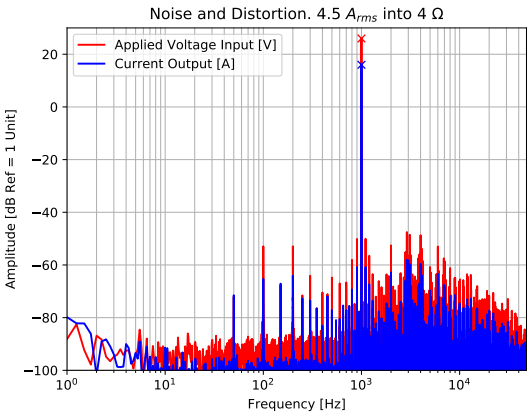


(f) Noise floor and Distortion, TL081, 80 W into 4 Ω.

FIGURE D.7 – Op Amp influence, 4 Ω resistive load. Red indicates the voltage applied to the input of the module by the voltage amplifier, and blue indicates the current output of the module. (a),(c),(e) : Noise floor and harmonic distortion for a 1 kHz sine wave input for 1 W, 10 W and 80 W. NE5534 Op Amp (b),(d),(f) : Same as (a),(c),(e) but with TL081 Op Amp.

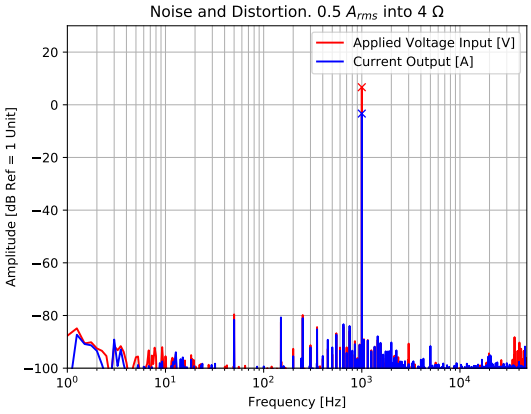


(a) Noise floor and Distortion, PhD Module 1 W into 4 Ω.

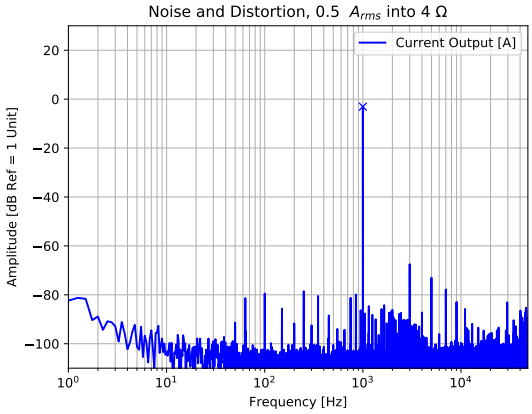


(b) Noise floor and Distortion, BAA1000, 1 W into 4 Ω.

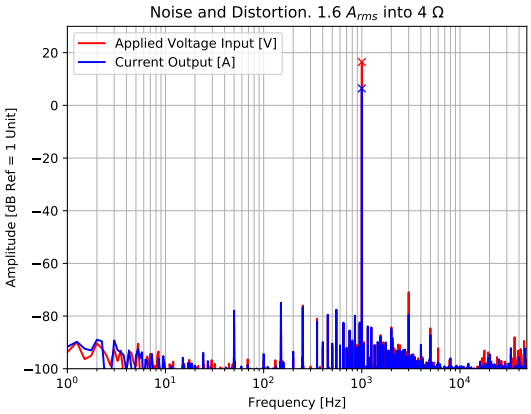


(c) Noise floor and Distortion, Phd Module, 10 W into 4 Ω.

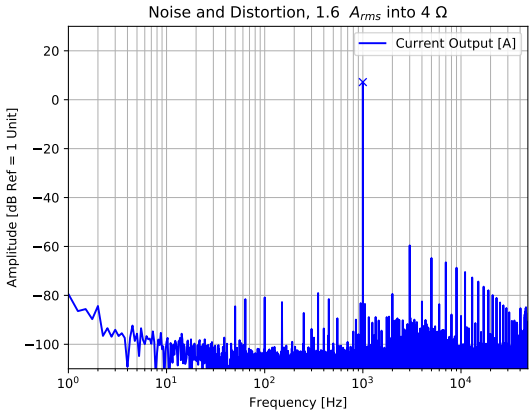


(d) Noise floor and Distortion, BAA1000, 10 W into 4 Ω.

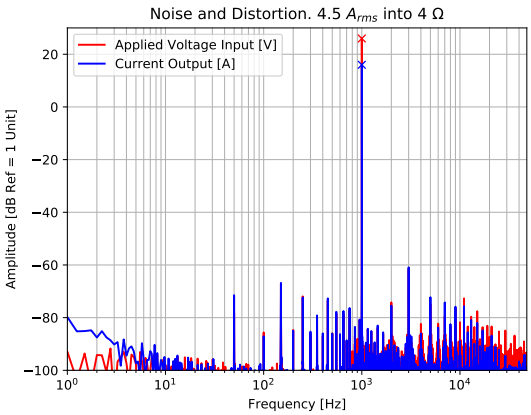


(e) Noise floor and Distortion, Phd Module, 80 W into 4 Ω.

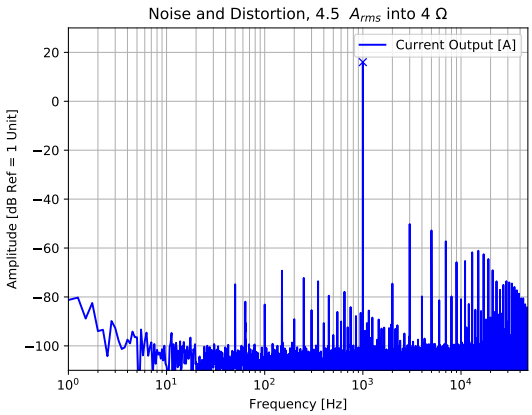


(f) Noise floor and Distortion, BAA1000, 80 W into 4 Ω.

FIGURE D.8 – Amplifier Characteristics, 4 Ω resistive load. Red indicates the voltage applied to the input of the module by the voltage amplifier, and blue indicates the current output of the module. (a),(c),(e) : Noise floor and harmonic distortion for a 1 kHz sine wave input for 1 W, 10 W and 80 W. Module (b),(d),(f) : Same as (a),(c),(e) but for a BEAK BAA1000 commercial amplifier.

Annexe E

# Appendix - Voltage/Current Sensing

## E.1 Component & Topology choice

The goal of this mini project was to develop a system capable of providing low noise current and voltage measurements with a further requirement to avoid any issues due to ground loops. An efficient way of reducing the amount of noise when measuring a voltage or current is to use Kelvin connections, also known as a four point measurement, in conjunction with differential inputs. Ground loops and noise can be reduced by using batteries instead of traditional power supplies.
The final design uses an instrumentation Op Amp, the Texas Instruments INA128, powered by a symmetrical supply provided by two 9 V batteries. The quiescent current of a single INA128 is 700 $\mu A$ which gives a total continuous measurement time of approximately 22 days using 380 mAh 9 V batteries.
For the current sensing, a 0.1 $\Omega$ resistor is used in a low side configuration. In order to reduce the overall footprint of the measurement system, a 3 W 2512 SMD resistor is used. An example of the finished circuit is shown in Figure E.1. Special care was taken when laying out the resistor and the connections to the Op Amp as in [75].

## E.2 Layout

For the use of differential inputs to be most effective, the current paths from the measurement point to the input must be a symmetrical as possible as any differences will be amplified. Figure E.2 shows a zoom of the section of interest. Red indicates the top copper layer while green indicates the bottom copper layer. Pads 1 and 2 are the measurement points for the voltage across the shunt resistor. It should be clear that the path from either point 1 or 2 is the same, with precision resistors used for the inputs.
In order to screen the current paths from outside electromagnetic perturbations, a copper plane is used for the reference and used as a shield for the low voltage input tracks.

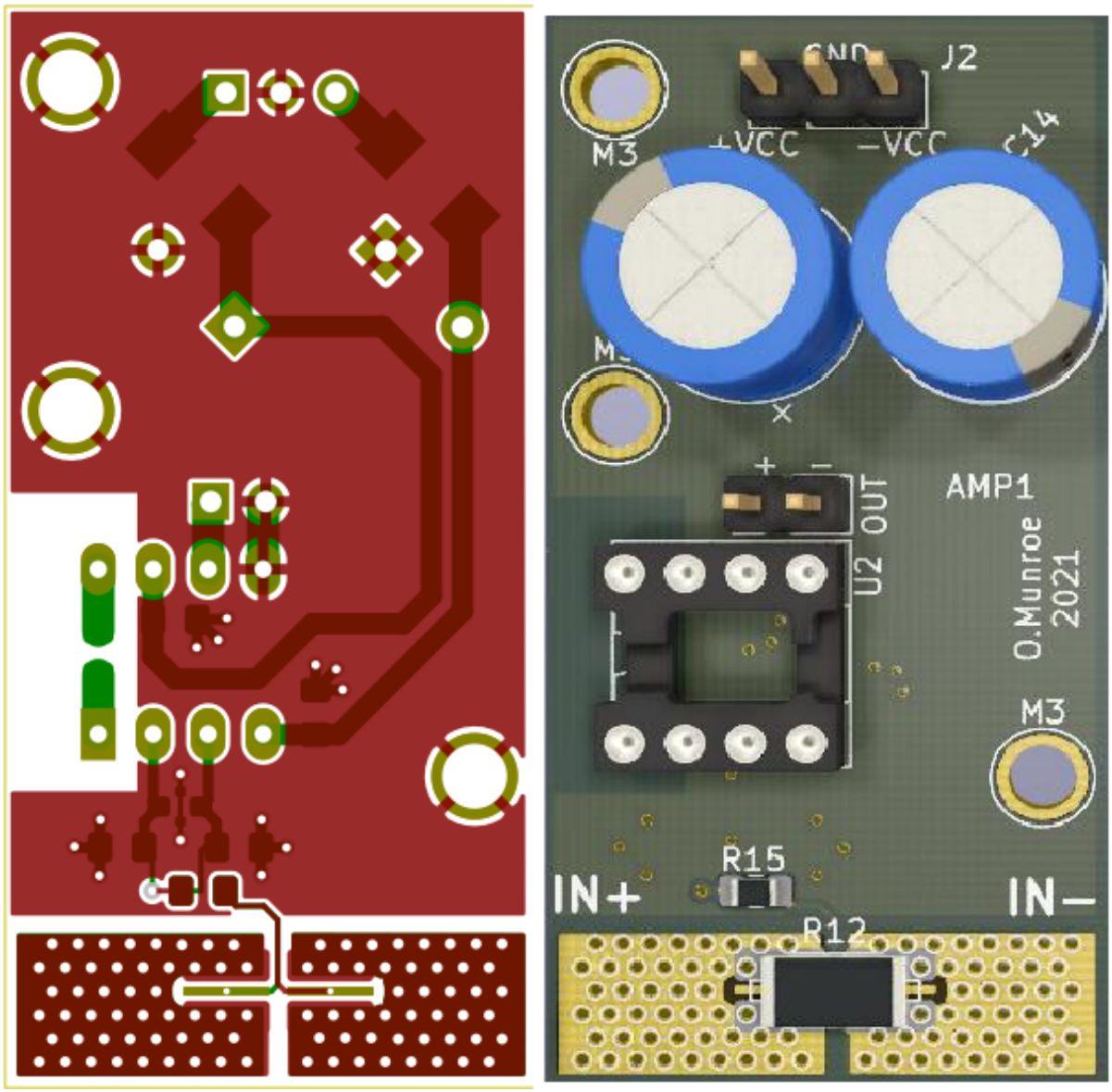


Figure E.1 – Differential Input Current Sensing

Finally in order to improve the thermal performance, plated holes are used around the SMD resistor to aid in heat dissipation through increasing the dissipating surface area. Due to their low surface area, SMD resistors tend to dissipate heat through their copper pads and the solder connection [101].

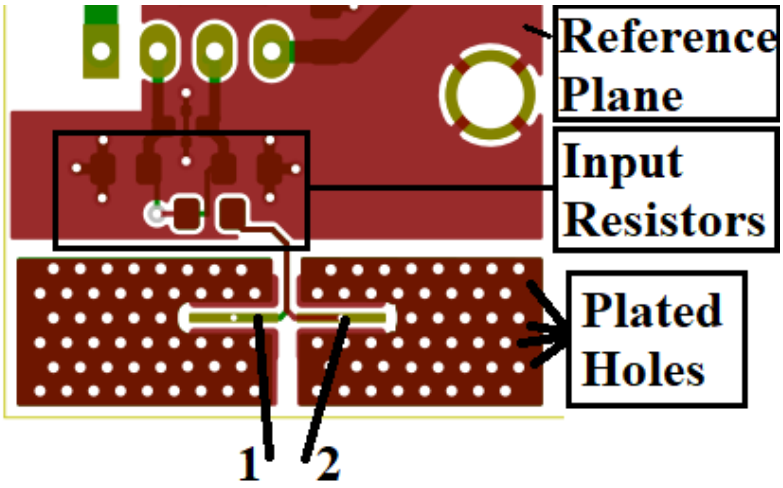


FIGURE E.2 – Differential Input symmetry.

## E.3 Developed system

The final system can be seen in Figure E.3. Four differential modules are used to provide two sensitivity options for both the voltage and current output. The voltage sensing is done at the connection point (seen here as the banana plugs) using the thin white and black wire while the load current is carried by the thicker red and black wires. Two 9 V batteries power the circuits without any reference to the electrical earth, leading to a floating differential voltage and current measurement system. If no current monitoring is needed, the voltage sensing wires can be clipped onto the points of interest and the voltage measured differentially.


FIGURE E.3 – Voltage/Current sensing system

# BIBLIOGRAPHIE


[1] *1ET400A DATA SHEET*, 1.0, Purifi, oct. 2019.

[2] Finn AGERKVIST et Bo Rhode PEDERSEN, « Time Variance Of The Suspension Nonlinearity », in : *Journal of the Audio Engineering Society* (oct. 2008).

[3] Finn AGERKVIST, Knud THORBORG et Carsten TINGGARD, « A Study Of The Creep Effect In Loudspeaker Suspension », in : *Journal of the Audio Engineering Society* (oct. 2008).

[4] Isao ANAZAWA, « Impact Of The Coupling Factor On Lossy Voice Coil Impedance », in : *Journal of the Audio Engineering Society* (mars 2019).

[5] ARESLIAM, URL : `https://commons.wikimedia.org/wiki/File:Mullins_Effect.png`, (accessed : 04.2022).

[6] Manish ARORA, Seongcheol JANG et Hangil MOON, « Low Complexity Virtual Bass Enhancement Algorithm For Portable Multimedia Device », in : *Journal of the Audio Engineering Society* (sept. 2006).

[7] Juha BACKMAN, « Dynamic Driver Linearization Using Current Feedback », in : *Journal of the Audio Engineering Society* (mai 2018).

[8] Marco BARATELLI et Oliver MUNROE, « Predicting Loudspeaker Current Distortion With FEA », in : *Journal of the Audio Engineering Society* (mai 2020).

[9] Benjamin B. BAUER, « Acoustic Damping For Loudspeakers », in : *Transactions of the IRE Professional Group on Audio* AU-1.*3* (1953), p. 23-34, DOI : `10.1109/TSP.1953.28133`.

[10] M. A. H. BEERLING, Cornelis H. SLUMP et Otto E. HERMANN, « Reduction On Nonlinear Distortion In Loudspeakers With Digital Motional Feedback », in : *Journal of the Audio Engineering Society* (fév. 1994).

[11] David BIRT, « A Motion Transducer For Low-Frequency Loudspeakers », in : *Journal of the Audio Engineering Society* (oct. 1991).

[12] Ruben BJERREGAARD et al., « Accelerometer Based Motional Feedback Integrated In A 2 3/4" Loudspeaker », in : *Journal of the Audio Engineering Society* (mai 2016).

[13] Fernando Bolaños, « Modal Analysis And Nonlinear Normal Modes (NNM) On Moving Assemblies Of Loudspeakers », in : *Journal of the Audio Engineering Society* (oct. 2005).

[14] Pascal Brunet et Glenn S. Kubota, « Nonlinear Control Of Loudspeaker Based On Output Flatness And Trajectory Planning », in : *Journal of the Audio Engineering Society* (oct. 2019).

[15] J.C. Butcher, *Numerical Methods for Ordinary Differential Equations*, Wiley, 2003, isbn : 978-0-471-96758-3.

[16] Doug Button et al., « Characterization Of Nonlinear Port Parameters In Loudspeaker Modeling », in : *Journal of the Audio Engineering Society* (oct. 2018).

[17] William Cardenas et Wolfgang Klippel, « Loudspeaker Rocking Modes (Part 1 : Modeling) », in : *Journal of the Audio Engineering Society* (oct. 2015).

[18] Johan A. Catrysse, « On The Design Of Some Feedback Circuits For Loudspeakers », in : *Journal of the Audio Engineering Society* (mars 1983).

[19] Krzysztof Chwastek, « Modelling Of Dynamic Hysteresis Loops Using The Jiles–Atherton Approach », in : *Mathematical and Computer Modelling of Dynamical Systems* 15 (fév. 2009), p. 95-105, doi : 10.1080/13873950802432016.

[20] F. Griffiths David et J. Higham Desmond, *Numerical Methods for Ordinary Differential Equations*, Springer, London, 2010, isbn : 978-0-85729-147-9, doi : https://doi.org/10.1007/978-0-85729-148-6.

[21] Yvan Denis, Nahiene Hamila et Fabrice Morestin, « Hysteresis Behavior Modelling Of Woven Fabric Under Large Strain », in : *AIP Conference Proceedings* 2113.*1* (2019), p. 020003, doi : 10.1063/1.5112508, eprint : https://aip.scitation.org/doi/pdf/10.1063/1.5112508, url : https://aip.scitation.org/doi/abs/10.1063/1.5112508.

[22] Julie Diani, Bruno Fayolle et Pierre Gilormini, « A review on the Mullins effect », in : *European Polymer Journal* 45.*3* (2009), p. 601-612, issn : 0014-3057, doi : https://doi.org/10.1016/j.eurpolymj.2008.11.017, url : https://www.sciencedirect.com/science/article/pii/S0014305708006332.

[23] Mark Dodd, Wolfgang Klippel et Jack Oclee-brown, « Voice Coil Impedance As A Function Of Frequency And Displacement », in : *Journal of the Audio Engineering Society* (oct. 2004).

[24] Antoine Falaize et Thomas Hélie, « Passive modelling of the electrodynamic loudspeaker : from the Thiele–Small model to nonlinear port-Hamiltonian systems », in : *Acta Acustica* 4.*1* (fév. 2020), p. 1, doi : 10.1051/aacus/2019001, url : https://hal.archives-ouvertes.fr/hal-02496422.

[25] Antoine Falaize et al., « Compensation of loudspeaker's nonlinearities based on flatness and port-Hamiltonian approach », in : *22ème Congrès Français de Mécanique*, Association Française de Mécanique, Lyon, France, août 2015, URL : https://hal.archives-ouvertes.fr/hal-01245632.

[26] R.P. Feynman, R.B. Leighton et M. Sands, *The Feynman Lectures on Physics, Vol. II : The New Millennium Edition : Mainly Electromagnetism and Matter*, The Feynman Lectures on Physics, Basic Books, 2011, ISBN : 9780465024940, URL : https://books.google.fr/books?id=hlRhwGK40fgC.

[27] Ronald M. Foster, « A Reactance Theorem », in : *Bell System Technical Journal* 3.*2* (1924), p. 259-267, DOI : https://doi.org/10.1002/j.1538-7305.1924.tb01358.x, eprint : https://onlinelibrary.wiley.com/doi/pdf/10.1002/j.1538-7305.1924.tb01358.x, URL : https://onlinelibrary.wiley.com/doi/abs/10.1002/j.1538-7305.1924.tb01358.x.

[28] Mohammed E. Fouda, Ahmed Radwan et Anis Allagui, « Power and Energy Analysis of Fractional-order Electrical Energy Storage Devices », in : *Energy* 111 (sept. 2016), p. 785-792, DOI : 10.1016/j.energy.2016.05.104.

[29] Frank X.Y. Gao et W. Martin Snelgrove, « Adaptive Linearization Of A Loudspeaker », in : *Journal of the Audio Engineering Society* (oct. 1992).

[30] Gary P. Geaves et David J. Henwood, « Finite Element Modelling Of A Loudspeaker. Part 1 : Theory and Validation. », in : *Journal of the Audio Engineering Society* (oct. 2005).

[31] Wolfgang Geiger, « Servo Control Of Loudspeaker Cone Motion Using An Optical Linear Displacement Sensor », in : *Journal of the Audio Engineering Society* 53.*6* (juin 2005), p. 518-524.

[32] Richard A. Greiner et Travis M. Sims jr., « Loudspeaker Distortion Reduction », in : *Journal of the Audio Engineering Society* 32.*12* (déc. 1984), p. 956-963.

[33] D.J. Griffiths, *Introduction to Electrodynamics*, v. 2, Cambridge University Press, 2017, ISBN : 9781108420419, URL : https://books.google.fr/books?id=ndAoDwAAQBAJ.

[34] R. Haber et L. Keviczky, *Nonlinear system identification. 2. Nonlinear system structure identification*, Mathematical Modelling Series, Kluwer Academic Publishers, 1999, ISBN : 9780792358572, URL : https://books.google.fr/books?id=0JpJKBdCRW4C.

[35] David S. Hall, « Design Considerations For An Accelerometer-Based Dynamic Loudspeaker Motional Feedback System », in : *Journal of the Audio Engineering Society* (oct. 1989).

[36] D.C. Hamill, « Lumped equivalent circuits of magnetic components : the gyrator-capacitor approach », in : *IEEE Transactions on Power Electronics* 8.*2* (1993), p. 97-103, doi : 10.1109/63.223957.

[37] Edward R. Hanson, « A Motional Feedback Loudspeaker System », in : *Journal of the Audio Engineering Society* (sept. 1973).

[38] H. D. Harwood, « Loudspeaker Distortion With Low-Frequency Signals », in : *Journal of the Audio Engineering Society* 20.*9* (nov. 1972), p. 718-728.

[39] Podlubny Igor, *Fractional Differential Equations*, Academic Press, 1999, isbn : 0-12S5H810-2.

[40] Jfmelero, url : https://commons.wikimedia.org/w/index.php?curid=6120095, (accessed : 04.2022).

[41] D. C. Jiles et D. L. Atherton, « Theory Of Ferromagnetic Hysteresis (Invited) », in : *J. of Applied Physics* 55.*6* (1984), p. 2115-2120, doi : 10.1063/1.333582, eprint : https://doi.org/10.1063/1.333582, url : https://doi.org/10.1063/1.333582.

[42] D. B. (Don) Keele jr. et Ryan J. Mihelich, « Suspension Bounce As A Distortion Mechanism In Loudspeakers With A Progressive Stiffness », in : *Journal of the Audio Engineering Society* (avr. 2002).

[43] Alexander King et Finn Agerkvist, « Fractional Derivative Loudspeaker Models For Nonlinear Suspensions And Voice Coils », in : *Journal of the Audio Engineering Society* 66.*7/8* (juin 2018), p. 525-536, doi : https://doi.org/10.17743/jaes.2018.0030.

[44] Alexander King et Finn T. Agerkvist, « State-Space Modeling of Loudspeakers Using Fractional Derivatives », in : *Audio Engineering Society Convention 139*, oct. 2015, url : http://www.aes.org/e-lib/browse.cfm?elib=17970.

[45] Alexander W. King et Finn T. Agerkvist, « Position Dependence Of Fractional Derivative Models For Loudspeaker Voice Coils With Lossy Inductance », in : *Journal of the Audio Engineering Society* (mai 2017).

[46] Wolfgang Klippel, « Direct Feedback Linearization Of Nonlinear Loudspeaker Systems », in : *Journal of the Audio Engineering Society* 46.*6* (juin 1998), p. 499-507.

[47] Wolfgang Klippel, « Loudspeaker Nonlinearities – Causes, Parameters, Symptoms », in : *Journal of the Audio Engineering Society* (oct. 2005).

[48] Wolfgang Klippel, « Mechanical Fatigue And Load-Induced Aging Of Loudspeaker Suspension », in : *Journal of the Audio Engineering Society* (oct. 2011).

[49] Wolfgang Klippel, « Nonlinear Adaptive Controller For Loudspeakers With Current Sensor », in : *Journal of the Audio Engineering Society* (mai 1999).

[50] Wolfgang Klippel, « Nonlinear Modeling Of The Heat Transfer In Loudspeakers », in : *Journal of the Audio Engineering Society* (mars 2003).

[51] Wolfgang Klippel, « The Mirror Filter-A New Basis For Reducing Nonlinear Distortion And Equalizing Response In Woofer Systems », in : *Journal of the Audio Engineering Society* 40.*9* (sept. 1992), p. 675-691.

[52] Timothy Lahey, « Modelling Hysteresis in the Bending of Fabrics », thèse de doct., jan. 2015.

[53] Steven A. Lane et Robert L. Clark, « Improving Loudspeaker Performance For Active Noise Control Applications », in : *Journal of the Audio Engineering Society* 46.*6* (juin 1998), p. 508-519.

[54] James Lazar et Pascal M. Brunet, « Reluctance Force Compensation for the Nonlinear Control of a Loudspeaker », in : *Audio Engineering Society Convention 149*, oct. 2020.

[55] W. M Leach jr., « Loudspeaker Voice-Coil Inductance Losses : Circuit Models, Parameter Estimation, And Effect On Frequency Response », in : *Journal of the Audio Engineering Society* 50.*6* (juin 2002), p. 442-450.

[56] Claude Lemaréchal, *Cauchy and the Gradient Method*, 2012.

[57] Zhenkun Li et al., « Modelling Energy Dissipation And Hysteresis Of Woven Fabrics With Large Deformation Under Single Loading-Unloading Cycle », in : *Composite Structures* 279 (2022), p. 114781, ISSN : 0263-8223, DOI : https://doi.org/10.1016/j.compstruct.2021.114781, URL : https://www.sciencedirect.com/science/article/pii/S0263822321012290.

[58] Stephen Low et Malcolm J. Hawksford, « A Neural Network Approach To The Adaptive Correction Of Loudspeaker Nonlinearities », in : *Journal of the Audio Engineering Society* (oct. 1993).

[59] Luiz Luz de Almeida et al., « Limiting Loop Proximity Hysteresis Model », in : *Magnetics, IEEE Transactions on* 39 (fév. 2003), p. 523-528, DOI : 10.1109/TMAG.2002.806344.

[60] Balbine Maillou et al., « Modelling nonlinear viscoelastic behaviours of loudspeaker suspensions-like structures », in : *J. of Sound and Vibration* 416 (2018), p. 213-223, ISSN : 0022-460X, DOI : https://doi.org/10.1016/j.jsv.2017.11.046, URL : https://www.sciencedirect.com/science/article/pii/S0022460X1730826X.

[61] Riccardo MARIANI et al., « Toward an adjustable nonlinear low frequency acoustic absorber », in : *Journal of Sound and Vibration* 330.*22* (2011), p. 5245-5258, DOI : 10.1016/j.jsv.2011.03.034, URL : https://hal.archives-ouvertes.fr/hal-00628729.

[62] William V. MARS, URL : https://en.wikipedia.org/wiki/File:Payne_Effect_in_filled_rubber.png, (accessed : 04.2022).

[63] *MAX5717/MAX5719 16 and 20-Bit Voltage DACs*, 19-8567, Rev. 2, MAXIM Integrated, juill. 2019.

[64] Victor Y. MAZIN, « Modeling Of Magnetic Hysteresis And Its Influence On Harmonic Distortion In Electrodynamic Loudspeakers », in : *Journal of the Audio Engineering Society* (mai 1999).

[65] D. C. MEEKER, *Finite Element Method Magnetics, Version 4.2 (28Feb2018 Build)*, URL : https://www.femm.info.

[66] Benoit MERIT, « Contribution à L'Identification Des Non-Linéarités Des Moteurs De Haut-Parleurs Electrodynamiques : Sur La Réalisation De Moteurs Tout Aimant », 2010LEMA1012, thèse de doct., 2010, 1 vol. (VII-[2]-146 p.) URL : http://www.theses.fr/2010LEMA1012/document.

[67] Paul G. MILLS et Malcolm J. HAWKSFORD, « Distortion Reduction In Moving-Coil Loudspeaker Systems Using Current-Drive Technology », in : *Journal of the Audio Engineering Society* 37.*3* (mars 1989), p. 129-148.

[68] Paul G. MILLS et Malcolm J. HAWKSFORD, « Transconductance Power Amplifier Systems For Current-Driven Loudspeakers », in : *Journal of the Audio Engineering Society* 37.*10* (oct. 1989), p. 809-822.

[69] Jean-Pierre MORKERKEN et al., « Vented-Box Geometry And Low Frequency Reproduction : The Aerodynamical Approach », in : *Journal of the Audio Engineering Society* (avr. 2002).

[70] L. MULLINS, « Softening of Rubber by Deformation », in : *Rubber Chemistry and Technology* 42.*1* (mars 1969), p. 339-362, ISSN : 0035-9475, DOI : 10.5254/1.3539210, eprint : https://meridian.allenpress.com/rct/article-pdf/42/1/339/1936732/1_3539210.pdf, URL : https://doi.org/10.5254/1.3539210.

[71] Oliver MUNROE, Stephane LETOURNEUR et Antonin NOVAK, « Design Of An Electronic Circuit For Loudspeaker Real-Time Digital Signal Processing », in : *16eme Congrès Français d'Acoustique*, Marseille, France, mars 2022, URL : https://hal.archives-ouvertes.fr/hal-03685026.

[72] Oliver Munroe, Antonin Novak et Laurent Simon, « Reluctance Force Modeling And Compensation », in : *Journal of the Audio Engineering Society* 70.*3* (mars 2022), p. 177-184, doi : https://doi.org/10.17743/jaes.2021.0054.

[73] Kevin P. Murphy, *Probabilistic Machine Learning : An introduction*, MIT Press, 2022, url : probml.ai.

[74] Antonin Novak, « Modeling Viscoelastic Properties Of Loudspeaker Suspensions Using Fractional Derivatives », in : *Journal of the Audio Engineering Society* 64.*1/2* (jan. 2016), p. 35-44, doi : https://doi.org/10.17743/jaes.2015.0091.

[75] Marcus O'Sullivan, *Optimize High-Current Sensing Accuracy by Improving Pad Layout of Low-Value Shunt Resistors*, url : https://www.analog.com/en/analog-dialogue/articles/optimize-high-current-sensing-accuracy.html, (accessed : 20.04.2021).

[76] Harry F. Olson, « Analysis Of The Effects Of Nonlinear Elements Upon The Performance Of A Back-Enclosed, Direct Radiator Loudspeaker Mechanism », in : *Journal of the Audio Engineering Society* 10.*2* (avr. 1962), p. 156-162.

[77] A. R. Payne, « The Dynamic Properties Of Carbon Black-Loaded Natural Rubber Vulcanizates. Part I », in : *J. of Applied Polymer Science* 6.*19* (1962), p. 57-63, doi : https://doi.org/10.1002/app.1962.070061906, eprint : https://onlinelibrary.wiley.com/doi/pdf/10.1002/app.1962.070061906, url : https://onlinelibrary.wiley.com/doi/abs/10.1002/app.1962.070061906.

[78] Bo Rohde Pedersen et Finn T. Agerkvist, « Time Varying Behavior Of The Loudspeaker Suspension », in : *Journal of the Audio Engineering Society* (oct. 2007).

[79] Bo Rohde Pedersen et Rer Rubak, « Linearization Of Nonlinear Loudspeakers », in : *Journal of the Audio Engineering Society* (oct. 2006).

[80] Yves Pene, Yoachim Horyn et Christophe Combet, « Non-Linear Acoustic Losses Prediction In Vented Loudspeaker Using Computational Fluid Dynamic Simulation », in : *Journal of the Audio Engineering Society* (mai 2020).

[81] Gaël Pillonnet et al., « Distortion Improvement In The Current Coil Of A Loudspeaker », in : *Journal of the Audio Engineering Society* (mai 2013).

[82] F. Preisach, « Über die Magnetische Nachwirkung », in : *Zeitschrift für Physik* 94.*5* (1935), p. 277-302, doi : 10.1007/BF01349418, eprint : https://doi.org/10.1063/1.333582, url : https://doi.org/10.1007/BF01349418.

[83] Chester W. Rice et Edward W. Kellogg, « Notes On The Development Of A New Type Of Hornless Loudspeaker », in : *Journal of the Audio Engineering Society* 30.*7/8* (août 1982), p. 512-521.

[84] Lars Risbo et al., « Force Factor Modulation In Electro Dynamic Loudspeakers », in : *Journal of the Audio Engineering Society* (sept. 2016).

[85] Dominick Rosato, Donald Rosato et Marlene Rosato, *Plastics Design Handbook*, jan. 2001, DOI : 10.1007/978-1-4615-1399-5.

[86] Hans Schurer, Cornelis H. Slump et Otto E. Herrmann, « Exact Input-Output Linearization Of An Electrodynamical Loudspeaker », in : *Journal of the Audio Engineering Society* (nov. 1996).

[87] Meir Shashoua et Daniel Glotter, « Method and System For Enhancing Quality Of Sound Signal », US5930373A, 1997.

[88] Takeo Shindo, Osamu Yashima et Hideo Suzuki, « Effect Of Voice-Coil And Surround On Vibration And Sound Pressure Response of Loudspeaker Cones », in : *Journal of the Audio Engineering Society* 28.*7/8* (août 1980), p. 490-499.

[89] Karl Erik Stahl, « Synthesis Of Loudspeaker Mechanical Parameters By Electrical Means : A New Method For Controlling Low-Frequency Loudspeaker Behaviour », in : *Journal of the Audio Engineering Society* (nov. 1978).

[90] Adel Tayeb et al., « On The Nonlinear Viscoelastic Behavior Of Rubber-Like Materials : Constitutive Description And Identification », in : *International Journal of Mechanical Science* 130 (2017), p. 437-447, ISSN : 0020-7403, DOI : https://doi.org/10.1016/j.ijmecsci.2017.06.032, URL : https://www.sciencedirect.com/science/article/pii/S0020740317304460.

[91] Steve Temme et Pascal Brunet, « A New Method For Measuring Distortion Using A Multitone Stimulus And Noncoherence », in : *Journal of the Audio Engineering Society* 56.*3* (mars 2008), p. 176-188.

[92] Knud Thorborg et Claus Futtrup, « Electrodynamic Transducer Model Incorporating Semi-Inductance And Means For Shorting AC Magnetization », in : *Journal of the Audio Engineering Society* 59.*9* (sept. 2011), p. 612-627.

[93] Knud Thorborg et al., « Frequency Dependence Of Damping And Compliance In Loudspeaker Suspensions », in : *Journal of the Audio Engineering Society* 58.*6* (juin 2010), p. 472-486.

[94] Xing Tian et al., « Compensation Of Nonlinear Distortion In Loudspeakers Considering Nonlinear Viscoelasticity Of The Suspension », in : *Journal of the Audio Engineering Society* 69.*3* (mars 2021), p. 204-210, DOI : https://doi.org/10.17743/jaes.2020.0072.

[95] Xing Tian et al., « Identification Of Nonlinear Fractional Derivative Loudspeaker Model », in : *Journal of the Audio Engineering Society* 68.*5* (mai 2020), p. 355-363, DOI : https://doi.org/10.17743/jaes.2020.0010.

[96] Tanya Tolpekina, W. Pyckhout-Hintzen et Bo Persson, « Linear and Nonlinear Viscoelastic Modulus of Rubber », in : *Lubricants* 7 (mars 2019), p. 22, doi : 10.3390/lubricants7030022.

[97] *Understand SINAD, ENOB, SNR, THD, THD + N, and SFDR so You Don't Get Lost in the Noise Floor*, MT-03, Rev. A, Analog Devices, oct. 2008.

[98] John Vanderkooy, « A Model Of Loudspeaker Driver Impedance Incorporating Eddy Currents In The Pole Structure », in : *Journal of the Audio Engineering Society* 37.*3* (mars 1989), p. 119-128.

[99] Alexander Voishvillo et al., « Graphing, interpretation, and comparison of results of loudspeaker nonlinear distortion measurements », in : *journal of the audio engineering society* 52.*4* (avr. 2004), p. 332-357.

[100] M. R. Ward, *Electrical Engineering Science*, Maidenhead : McGraw-Hill, 1971, isbn : ISBN 9780070942554.

[101] Bryan Yarborough, *Thermal Management for Surface-Mount Devices*, rapp. tech. 30380, VISHAY DALE, mars 2018, url : https://www.vishay.com/docs/30380/terminalderating.pdf.

[102] Xiang Zhang, « Analysis and design of an adaptive-supply class H audio power amplifier for mobile devices », thèse de doct., 2017, doi : 10.32657/10356/72875.

DOCTORAT BRETAGNE LOIRE SCIENCES POUR L'INGENIEUR

Le Mans Université

**Titre :** Contrôle du haut parleur en temps réel

**Mot clés :** Haut parleur, Rétroaction, Distorsion, Modèle Prédictif, Amplificateur, Contrôleur

**Résumé :** L'objectif de cette thèse est de fournir des solutions matérielles et logicielles simplifiées au problème de la linéarisation des haut-parleurs en temps réel. La plupart des méthodes existantes nécessitent l'utilisation de capteurs externes, utilisent des modèles non linéaires complexes, ou tentent d'optimiser tous les paramètres non linéaires du modèle prédictif. D'un point de vue industriel, la simplicité est attrayante, donc la thématique principale de ce travail est de proposer un cadre de linéarisation qui soit aussi simple que possible tout en étant compétitif avec les autres méthodes.

Afin de rendre l'algorithme aussi simple que possible, la plupart des paramètres non linéaires sont fournis a priori par l'utilisation de simulations et de fiches techniques. Seule la fonction non linéaire utilisée pour représenter la suspension du haut-parleur est optimisée en temps réel pour adapter les paramètres à l'échantillon. L'algorithme est exécuté sur un contrôleur à faible latence, et le signal de commande est appliqué au système de haut-parleurs via un système d'amplificateur de puissance à transconductance. Le contrôleur et le système d'amplificateur de puissance ont été conçus, construits et validés par l'auteur au cours de cette thèse.

Le système de contrôle est simulé et les effets de la résolution ADC, de l'erreur de modèle et de l'amortissement mécanique sur la compensation sont analysés. Les résultats des mesures montrent que le système de contrôle est capable de réduire les distorsions harmoniques et d'intermodulation dans l'accélération du cône jusqu'à 25 dB entre 10 Hz et 1000 Hz. Le système de contrôle permet également de contrôler la réponse en fréquence linéaire du système de haut-parleurs, en éliminant le pic présent à la fréquence de résonance du haut-parleur ou en fournissant une modification plus large de la réponse en fréquence.

**Title:** Real Time Loudspeaker Control

**Keywords:** Loudspeaker, Linearisation, Feedback, Feed Forward, Correction, Distortion

**Abstract:** The aim of this thesis is to provide simplified hardware and software solutions to the problem of real time loudspeaker linearisation. Most of the existing methods require the use of external sensors, use complex nonlinear models, or attempt to optimise all the nonlinear parameters of the feed forward model. From an industrial standpoint simplicity is attractive, so the main thematic of this work is to propose a linearisation framework that is as simple as possible while still being competitive with other methods.

In order to make the algorithm as simple as possible, most of the nonlinear parameters are provided *a priori* through the use of simulations and data sheets. Only the nonlinear function used to represent the loudspeaker suspension is optimised in real time to adapt the parameters to the sample drive unit. The algorithm is run on a low latency controller, and the control signal applied to the loudspeaker system via a transconductance power amplifier system. Both the controller and the power amplifier system were designed, built and validated by the author during this thesis.

The control system is simulated and the effects of ADC resolution, model error, and mechanical damping on the compensation are analysed. Measurement results show that the control system is capable of reducing both harmonic and intermodulation distortions in the cone acceleration by up to 25 dB between 10 Hz and 1000 Hz. The control system also enables the control of the linear frequency response of the loudspeaker system, removing the peaking present at the loudspeaker resonance frequency or providing a more broad band modification of the frequency response.